Development of novel calibration methods and performance forecaster of cutting-edge superconducting detector MKIDs for CMB experiments

Doctoral Thesis

博士論文

Development of novel calibration methods and performance forecaster of cutting-edge superconducting detector MKIDs for CMB experiments

(CMB 実験応用を目的とした最先端の超伝導検出器 MKIDs の新しい較正手法と性能推定ツールの開発)

Astronomical Institute, Graduate School of Science, Tohoku University

東北大学大学院 理学研究科 天文学専攻

Hiroki Kutsuma

沓間 弘樹

March, 2021

令和２年

Abstract

Development of novel calibration methods and performance forecaster of cutting-edge superconducting detector MKIDs for CMB experiments

by Hiroki Kutsuma

The Big Bang theory has recognized widely as the standard model describing the evolution of the universe. However, the theory is inherent by the fundamental problems, e.g., the horizontal problem and the flatness problem. In 1980s, Alan Guth and Katsuhiko Sato proposed the inflationary cosmology. Assuming the universe had an exponentially expanding period at the very early universe, they showed that these problems are naturally solved. According to the standard inflation theory, the tensor fluctuation was generated due to the quantum fluctuation of the space-time during the inflation period and it drifts in our universes as the primordial gravitational wave. The cross mode and plus mode primordial gravitational waves imprint the B-mode and E-mode polarizations in the CMB, respectively. Since the scalar mode fluctuation generates only the E-mode polarization, the detection of the B-mode CMB polarization provides smoking gun evidence of the inflation theory.

Many observation efforts have been done aiming for the first detection of the primordial B-mode CMB polarization. The power spectrum of the CMB B-mode polarization has two bumps. One is called recombination bump appeared at around small angular scale of 2 degree ($l \sim 100$), and the other is called reionization bump appeared at around large angular scale of 20 degree ($l < 10$). Many conventional ground-based CMB experiments target to detect the recombination bump. However, the expected amplitude of the primordial B-mode CMB polarization is less than the B-mode polarization caused by the disturbance on the E-mode CMB polarization due to the gravitational lensing effect of the large scale structure. On the other hand, the detection of the reionization bump from the ground-based observation is limited by $1/f$ atmospheric fluctuation. The atmospheric fluctuation becomes significant below 0.1 Hz. It is hard to detect reionization bump by conventional ground-based observations since it is impossible to cover a few tenth degree of sky within a few second. To access the reionization bump by the ground-based CMB polarization experiments, invention for observational strategy to mitigate the atmospheric fluctuation is required.

The sum of neutrino masses is one of the important parameters in describing the evolution of the early universe. It is experimentally proposed that the neutrinos have mass. Since the non-zero neutrino mass can not be explained by the standard model of the particle physics, the neutrinos are the only particles beyond the standard model currently known. We can evaluate the sum of the neutrino masses from the observation of the B-modes polarization due to the gravitational lensing effect of the large scale structure. However, to limit the sum of neutrino masses from the B-mode polarization due to the gravitational lensing effect of the large scale structure we need to know the precise optical depth at the reionization epoch τ, since the influence of the gravitational lensing effect of the large scale structure and Thomson scattering by the free electrons in the reionization are strongly degenerate. To evaluate the optical depth at the reionization epoch, the CMB E-mode polarization below $l \sim 10$ is useful since the scalar perturbation below $l \sim 10$ entered inside of the Hubble horizon after the reionization epoch. There is a systematic difference in the estimated τ between WMAP and Planck satellites results. The independent measurement of the optical depth at the reionization epoch by the CMB polarization experiment which is able to perform the secure measurement of the large angular scale signal is an important.

In order to observe the faint signal like the CMB polarization, various types of large format detector arrays toward astronomical observations, including CMB polarization observations are proposed. Recently, majority of CMB polarization experiments use a superconducting detector as a focal plane detector, because it is sensitive

enough to reach the noise level of the photon noise of the atmosphere for the ground-based observations. At present, many millimeter and submillimter telescope including CMB observation use a large format Transition Edge Sensor (TES) array as a focal plane detector. The TES is a superconducting detector. In next decade, over mega pixel focal plane detector is going to be required in order to increase the precision of the observations. However, the development of the mega pixel TES camera is hard with the current readout multiplexer system. The Microwave Kinetic Inductance Detector (MKID) is the cutting-edge superconducting detector which enable to break the mega pixel wall. The advantage of the MKID is that it has a potential to read over thousands pixels per single readout line. Moreover, the time response of the MKID (< 100 μs) is significantly faster than the TES.

Although the MKID is the detector technology which is supposed to explore the mega pixel era, it has several fundamental problems which have to be overcome. The one is that there is significant systematic uncertainty involved in the calibration of the detector performance since there is no novel method for the responsivity calibration. The MKID for millimeter and submillimter astronomical observations is operated at $250 - 300$ mK. Every day or a few day, the MKID is once warmed up above the transition temperature and cooled down below the transition temperature again. Since the performance of the MKID changes every cooling cycle, we have to perform calibration of the performance of the MKID, especially its responsivity, every cooling cycle. Conventionally, the calibration of the responsivity of the MKID has been performed by measuring the change of the response when the temperature of the detector mount plate is heated up by controlling the heater attached to the mount plate. This method is inevitable from following systematic error. It always accompanies uncertainties whether the plate temperature measured by the thermometer coincides with the detector temperature. This method is also time consuming. It takes several hours for every calibration. Therefore, a few 10% of the observational time is consumed by the responsivity calibration. The other problem is that the $1/f$ type noise always appears and it limits the performance in low sampling frequency. This noise is supposed to be attributed to the two level system (TLS) formed in the interface of the supercoducting material and substrate. To realize the photon noise limit high sensitivity MKID down to low sampling frequency, we have to mitigate the TLS noise in someway. The third problem is that there is no method to measure the superconducting transition temperature, T_c, of the hybrid type MKID which is widely used for the recent astronomical observations. The superconducting transition temperature of the MKID is one of the crucially important parameters to fix the design of MKID and evaluate performance.

The GroundBIRD is a ground-based CMB polarization experiment to probe the inflationary cosmology. For enabling to attack the reionization bump of the primordial B-mode CMB polarization and to observe the precise optical depth to reionization from the ground by mitigating the $1/f$ atmospheric fluctuation, the GroundBIRD performs a rapid rotation scan around the zenith direction with inclining the telescope 30 degree from zenith at rotation speed of 20 rotations per minute, which corresponds to 3 seconds for one rotation. Because of the earth rotation 44% of the full sky area is covered in a day. Since the time response of MKID is significantly faster than TES and satisfies the requirements from the rapid rotation scan strategy, MKID is installed on the focal plane of the GroundBIRD. We show in this thesis that the performance of the prototype MKID is far from the GroundBIRD observation requirements based on the results of our performance verification experiments as shown in Chapter.3. The $1/f$ type TLS noise dominates over the generation and recombination noise below 100Hz. Further research and development is required to

optimize performance of the MKID to the GroundBIRD observation. However, the one cycle from the design to evaluation is about three months. We have to iterate this cycle several times to feed back the results to new design. Dramatic reduction of the consumption for this research and development cycle is desired.

We propose new method for the responsivity calibration in Chapter 4. The method uses the change of the number of the excess quasiparticles while changing the microwave readout power. By changing microwave readout power from high power to low power abruptly, the number of the excess quasiparticles transit to a new steady state with time constant. This time constant is called quasiparticle lifetime and the time has an relation between the number of quasiparticles in the MKID. We evaluate the number of quasiparticles from the quasiparticle lifetime using theoretical formula. As a result, the responsivity is extracted. We apply this method for the real measurement using the MKID maintained at 285 mK. We confirm the consistency between the results obtained using this method and conventional calibration methods. Since our method is free from the above mentioned systematic accompanying in the conventional method, the our method provides much more secure results compared with the conventional method. Furthermore, the time duration consumed for the calibration dramatically shortened, down to 10 minutes, by our proposed method.

We propose a new method to measure the T_c of MKID by abrupt change of the applied readout microwave power. The number of quasiparticles in the MKID decrease with the quasiparticle lifetime during abrupt change of the applied readout microwave power. Therefore, we can measure the relation between the quasiparticle lifetime and the detector phase response by abrupt change of the readout microwave power. As a results, we can estimate the intrinsic quasiparticle lifetime. The intrinsic quasiparticle lifetime is theoretically modeled by T_c, the physical temperature of the device, and other known parameters. We can extract T_c by comparing the measured lifetime with theoretical model. Using an MKID made of aluminium, we demonstrate this method at a 0.3 K operation. The results are consistent with those obtained by T_c measured by monitoring the transmittance of the readout microwave power for various device temperature. The proposed method opens a possibility to measure T_c of the hybrid type MKID directly. Since there was no method to measure T_c, the speculated value of T_c has been adopted. The speculated values vary largely from author to author in the range from 1.1 K to 1.5 K. This introduces tenfold difference in the estimated noise level of the MKID under dark condition. Our method fixes this large uncertainty and dramatically improves precision of designing the MKID. Since the photon noise of the atmosphere dominates over the intrinsic noise of the MKID for the GroundBIRD application, the uncertainty of the noise level introduced by the uncertainty of T_c in the range of 1.1 K to 1.5 K is about 20%.

We develop the forecaster which evaluate the performance of MKID quantitatively by setting environmental variables and design parameters as shown in Chapter 6. By inputting the design parameters of the prototype MKID into the forecaster, we confirmed that the TLS noise dominates over the BLIP noise below 100 Hz and that the main problem of the prototype MKID is its design. We show that this bad performance is attributed to the design. Since the total width of the coplanar waveguide (CPW) line made from Nb of the prototype MKID is too narrow, the contribution of the TLS noise became prominent. A new design of MKID with widening the total width of CPW line made from Nb is proposed. We evaluate the expected performance of the new design MKID using the forecaster in Chapter 7. We showed that the TLS noise is significantly reduced from that of the prototype MKID and is suppressed below the BLIP noise down to the GroundBIRD rotation frequency

(0.3 Hz).

Acknowledgements

I would like to thank Makoto Hattori for my undergraduate to doctor's course. He invited me the CMB experiment. Thanks for discussing my progress every week.

I would like to thank Chiko Otani. He invited me the GroundBIRD experiment and prepared my position in RIKEN.

I am deeply grateful to Osamu Tajima. He invited me the GroundBIRD experiment. Without his support, I wouldn't have been able to produce so many research results. He listened to my bad explanation, and connected them to physics. I learned a lot of things as well as research from him.

I would like to thank Satoru Mima, Shugo Oguri, Taketo Nagasaki, Junya Suzuki, and Shunsuke Honda. They are young researcher of the GroundBIRD experiment. They gave me various advice on my research. Discussions with them allowed me to have various perspectives on not only radio astronomy but also particle physics experiments and superconducting detector physics. My stay with them in Tenerife will be a memory of my lifetime.

I would like to thank Junta Komine and Takuji Ikemitsu. They were Kyoto University student. I stayed with them in Tenerife for two months. These two months are good memories. I deeply grateful to Yoshinori Sueno. He is Kyoto University student. He supported my research for the method to measure superconducting transition temperature of the MKID.

I would like to thank Akira Endo and Kenichi Karatsu. They are TUDelft and SRON researchers. They support to develop MKID for the GroundBIRD experiment. In my short stay in TUDelft, their advice on my research gave me confidence.

I would also like to thank all the people in Astronomical Institute, Tohoku University, the KEK CMB group, and RIKEN Center for Advanced Photonics Terahertz Sensing and Imaging Research Team. I could spend great time on Sendai for five years, on Tsukuba for two years, and on Wako for two years.

I would like to thank to my family for their supports during my student life.

Contents

Chapter 1

Introduction

In this Chapter, we briefly introduce the inflation theory to address why the CMB *B*-mode polarization observation is important. We also describe the optical depth to reionization that play an important role in the measurement of the sum of neutrino masses. The current status of development of the superconducting detector for astronomical observations are also briefly reviewed to address why the development of new type of superconducting detectors are required. At the end of the introduction, motivations of the development of the MKID performed by this thesis based on the requirements of GroundBIRD are described.

1.1 Observational confirmation of the inflation model

The Big Bang theory has recognized widely as the standard model describing the evolution of the universe. The theory has provided convincing explanation for the Hubble expansion law of the galaxies, the uniformity of the Helium 4 abundance in the Galactic and extra galactic interstellar medium and the cosmic microwave background radiation (CMB) with almost perfect blackbody spectrum at the temperature of 2.725K. However, the theory is inherent by the fundamental problems, e.g., the horizon problem and the flatness problem. The era of CMB photon was first released from the cosmic plasma is at around 370 k years from the beginning of the universe. The era is called the last scattering surface. The apparent angular size of the particle horizon at the last scattering surface is ~ 2 deg [1]. The structures of the CMB temperature fluctuation beyond this scale have been found [2, 3, 4]. Why the coherent structures beyond the horizon size of the early universe is called the horizon problem. The curvature of the current universe is close to zero, in other word the geometry of the current universe is close to flat [5, 6]. As described in Appendix A, this insists that the curvature of the universe at the begging of the universe must be tuned to a value close to zero with an accuracy of more than 62 orders. This fine tuning problem is called the flatness problem.

In 1980s, Alan Guth and Katsuhiko Sato proposed the inflationary cosmology [7, 8]. Assuming the universe had an exponentially expanding period at the very early universe, they showed that these problems are naturally solved (see Appendix A). The main reason why the inflationary theory has been supported as the model which describes the evolution of the early universe is not the fact that the inflation is able to solve the above mentioned rather academical problems but its prediction power. Many of them have been observationally confirmed, such as the almost flat geometry of the current universe, the existence of the almost scale invariant scalar mode perturbation with almost Gaussian distribution etc. According to the standard inflation theory (see Appendix A), the tensor fluctuation was generated due to the quantum fluctuation of the space-time during the inflation period and it drifts in our

universe as the primordial gravitational wave background. Although the direct detection of the primordial gravitational wave is yet hard, indirect confirmation of the existence of the primordial gravitational wave and measurement of its amplitude are possible by performing the polarization observation of the cosmic microwave background (CMB). The primordial gravitational wave imprints the polarization signals in the CMB by the electron scattering at the last scattering surface and the reionization epoch [9]. The cross and plus modes of the primordial gravitational wave imprint the B-mode and E-mode polarization in the CMB, respectively. The brief introduction of the physical mechanism of generation of B-mode polarization due to the cross mode gravitational wave through the electron scattering is given in Appendix A. Since the scalar mode fluctuation generates only the E-mode polarization, the detection of the B-mode CMB polarization provides smoking gun evidence of the inflation theory. Hereafter, we refer the signal as the primordial B-mode CMB polarization. The detection of the primordial B-mode CMB polarization tells us the epoch of the inflation period since the amplitude of the power spectrum of the primordial gravitational wave is proportional to the fourth power of the temperature of the universe at the beginning of the inflation epoch, and provides the first observational confirmation of the quantum gravity (see Appendix A). In convention, the amplitude of the primordial tensor mode is expressed by the ratio of the power spectrum of the tensor perturbation to the scalar perturbation, r, since the amplitude of the scalar perturbation is well constrained from the observation of the CMB temperature fluctuation. It is called tensor-to-scalar ratio.

Many observational efforts have been done aiming for the first detection of the primordial B-mode CMB polarization. The power spectrum of the CMB B-mode polarization are shown in Figure. 1.1. The power spectrum of the primordial B-mode CMB polarization has two bumps. One is called recombination bump appeared at around small angular scale of 2 degree ($l \sim 100$), and the other is called reionization bump appeared at around large angular scale of 20 degree ($l < 10$). Many conventional ground-based CMB experiments target to detect the recombination bump. However, the expected amplitude of the primordial B-mode CMB polarization is less than the B-mode polarization caused by the disturbance on the E-mode CMB polarization due to the gravitational lensing effect of the large scale structure. Although a lot of efforts have been done for extracting the primordial B-mode CMB polarization from the detected signals [10], the claim for the detection of the recombination bump only is not convincing to accept the detection of the primordial B-mode CMB polarization since it is not clean evidence. On the other hand, the detection of the reionization bump from the ground-based observation is limited by $1/f$ atmospheric fluctuation. The atmospheric fluctuation becomes significant below 0.1 Hz. It is hard to detect reionization bump by conventional ground-based observations since it is impossible to cover a few tenth degree of sky within a few second. To access the reionization bump by the ground-based CMB polarization experiments, invention for observational strategy to mitigate the atmospheric fluctuation is required.

1.2 Optical depth to reionization

The optical depth to reionization τ is the important parameter to characterize the reionization. When the redshift z is below about 20, the first generation stars are formed, and the neutral hydrogen is reionized by the strong UV light emitted by the stars. The CMB photon is re-scattered by the decoupled electron in the reionization epoch. The optical depth to reionization is a quantity which provides a measure of

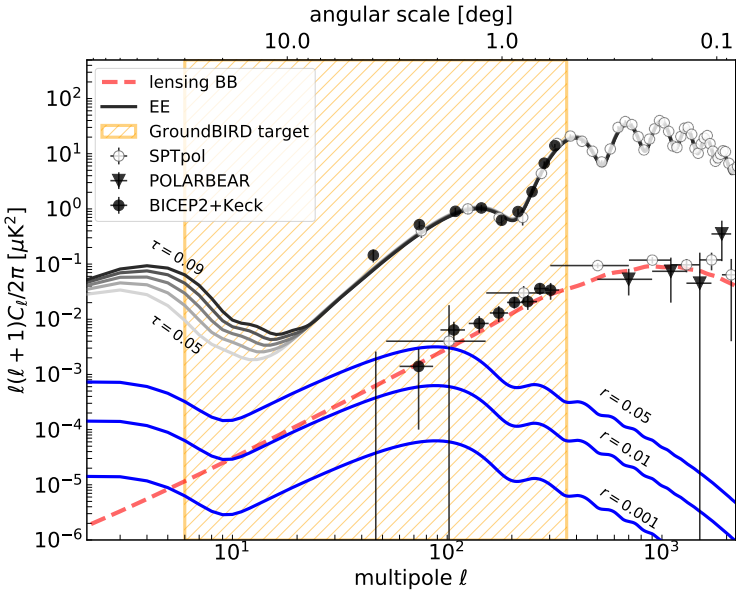

FIGURE 1.1: The power spectrum of E-mode polarization in various optical depth to reionization τ and that of B-mode polarization in various tensor-to-scolar ratio r as a function of multipole [11]. The orange region shows the GroundBIRD observation region. The some points with error bar is the observation results of the previous studies [12, 13, 14, 15]. The power spectrum of B-mode polarization at high multipole region is dominated by the gravitational lensing effect [11].

the line-of-site free-electron opacity to CMB radiation. The optical depth to reionization is given by

$$\tau = c\sigma_T \int_{t_r}^{t_0} \mathrm{d}t \bar{n}_e \tag{1.1}$$

where c is the speed of light, σ_T is the cross section of Thomson scattering, $\bar{n}_e$ is the average number density of the free electron, t_0 is the current time, and t_r is the time when the reionization is assumed to occur instantaneously.

The sum of neutrino masses is one of the important parameters in describing the evolution of the early universe. It is experimentally proved that the neutrinos have mass [16]. Since the non-zero neutrino mass can not be explained by the standard model of the particles physics, the neutrinos are the only particles beyond the standard model currently known. The CMB photons are affected by the gravitational potential due to the large scale structure of the universe during their arrival to us from the recombination epoch. The effect is called gravitational lensing. Since the neutrino has a large velocity dispersion during the formation of the large scale structure, the evolutionary rate of the large scale structure by the baryon and dark matter is delayed by the neutrino. In other words, the evolutionary rate of the formation of the large scale structure depends on the sum of neutrino masses. Therefore, we can evaluate the sum of the neutrino masses from the observation of the B-mode polarization due to the gravitational lensing effect of the large scale structure. However, to limit the sum of neutrino masses from the B-mode polarization due to the gravitational lensing effect of the large scale structure we need to know the precise optical depth to reionization, since the influence of the gravitational lensing effect of the large scale structure and Thomson scattering by the free electrons in the reionization

epoch are strongly degenerate [17]. Since the fluctuation at high multipole region enter the Hubble horizon earlier than that at low multipole region, the power spectrum at high multipole region show the past fluctuation of the universe. The information of the fluctuation in the higher multipole region than the reionization bump is disturbed by the decoupled electron in the reionization epoch. In order to recover the information of the fluctuations entered the Hubble scale before reionization epoch, it is necessary to make precise observations of the optical depth to reionization, which is a quantity that indicates how much it is disturbed by the reionization epoch.

The E-mode polarization at $l < 10$ tells us the information of the reionization epoch, since the scalar perturbation at $l < 10$ entered inside of the Hubble horizon after the reionization epoch, therefore it avoids the re-scattered effects after the reionization epoch. The E-mode polarization at $l < 10$ has a bump shown in Figure 1.1. The WMAP and Planck satellite observed the bump and obtained optical depth to reionization. The WMAP proposed $\tau = 0.089 \pm 0.014$ [3] and the Planck proposed $\tau = 0.054 \pm 0.007$ [4]. The results are different. Since the WMAP satellite does not have high frequency detector, it may not be able to distinguish between CMB and dust polarization. Since Planck satellite was not designed to measure large angular scale and it takes about a year to observe the full sky, large systematic errors, e.g. detector drift due to the comic ray muon hit, are contaminated in the data. Therefore, the precise measurement of the optical depth at the reionization epoch by independent CMB polarization experiment is an important topic.

1.3 Developing the large format detector arrays toward astronomical observations

In order to observe the faint signal like the CMB polarization, various types of large format detector arrays toward astronomical observations including CMB polarization experiments are proposed. Recently many CMB polarization experiments use a superconducting detector as a focal plane detector, because it is sensitive enough to reach the noise level of the photon noise of the atmosphere for the ground-based observations and of the CMB for the observation from the space. The sensitivity of such detectors are called photon noise limit.

1.3.1 Mega pixel era

The history of the application of the direct detector for millimeter and submillimeter astronomical observation started from 1988 as shown in Figure 1.2. Caltech submillimeter observatory (CSO) applied direct detector composed by semiconductor thermister as a focal plane detector for radio astronomical observation at the first time. Until 2010, the semiconductor detector played the central role for the many astronomical observations as a focal plane detectors. Some observations used over 100 semiconductor detectors as a focal plane detector [18, 19, 20]. From 2000 to 2005, some telescopes, e.g., CAPMAP [21] and QUITE [22] used HEMT (High Electron Mobility Transistor) as a direct detector. From 2007, many telescopes start to use Transition Edge Sensor (TES) [23] as a focal plane detector. The TES is a direct detector composed of superconductor which utilizes the sensitive change of the resistance of the superconductor at around the superconducting transition temperature caused by the absorption of the radiation energy as its detection principle. APEX-SZ [24] is the project which is installed TES to APEX-12 m telescope, for the first time. By applying superconducting quantum interference device (SQUID) as for readout circuit,

multiplexing of the multi pixel TES detectors has started. At present, many millimeter and submillimeter telescopes including CMB observation e.g BICEP2 [25], ACT [26], SPT [27], and POLARBEAR [28] use a large format TES camera as a focal plane detector, because we can deep survey as the number of detectors increases. The next generation CMB experiments, e.g., Simons Observatory [29], and LiteBIRD [30] have a plan to install TES as a focal plane detector. Especially, the Simons observatory is planed to install 0.1 Mega pixel TES camera. Figure 1.2 shows the growth history of the number of detector pixels installed on the millimeter and submillimeter astronomical telescope. This figure tells followiing two things. Number of focal plane detector pixels grows exponentially. Change of the fundamental detector technology happened after 20 years from the first application of the semiconductor thermister to the astronomical observation to accelerate the increase of the number of the detector pixels. Although the figure suggests that the number of the detector pixel exceeds mega pixel in the next decade, renovation of detector technology might be required to realize the mega pixel era since it gets the 20th anniversary at 2025 after the first application of TES to the astronomical observations. In reality, the number of the detector pixel of TES camera is getting saturated. The bottle neck is that the number of pixels which is read out by a single multiplexer arrives at the limit. To break this wall, a new technology for the read out multiplexer of TES has been studied [31]. Microwave Kinetic Inductance Detector (MKID) is the cutting-edge superconducting detector which may be able to break the mega pixel wall. The DemoCam [32] used MKID as a focal plane detector for the first time. From 2007, many observations e.g., MUSIC[33], NIKA[34], NIKA2[35], DESHIMA[36], and BLAST-TNG[37] use MKID as a focal plane detector. Many experiments e.g., DESHIMA2.0 and TolTEC [38] have a plan to use MKID as a focal plane detector. In the next decade, the mega pixel focal plane detector will be required in order to do more precise measurement and observation. Since the MKID has an ability to read over kilo pixels per signal readout line [39], the MKID contain great pontential to realize mega pixel focal plane detector array.

Note that MKID is also used for near-infrared and visible light astronomical observations [40, 41] as well as millimeter and submillimeter observations.

The various types of the superconducting detectors and these detection mechanism are summarized in Appendix B.

1.3.2 The advantage of the MKID

Various studies have shown that performance of the MKID reached the photon noise limit [42, 39]. The following is the advantage of the MKID comparing the other superconducting photon detectors.

- The MKID is easy to fabricate.
- The MKID has a fast time response ($\tau < 100$ μs).
- The MKID has an ability to read over 1000 pixels per single readout line.

1.3.3 The fundamental problems of MKID to be overcome

Although the MKID is the detector technology which is supposed to explore the mega pixel era, it has several fundamental problems which have to be overcome. The one is that there is significant systematic uncertainty involved in the calibration of the detector performance since there is no novel method for the calibration. The

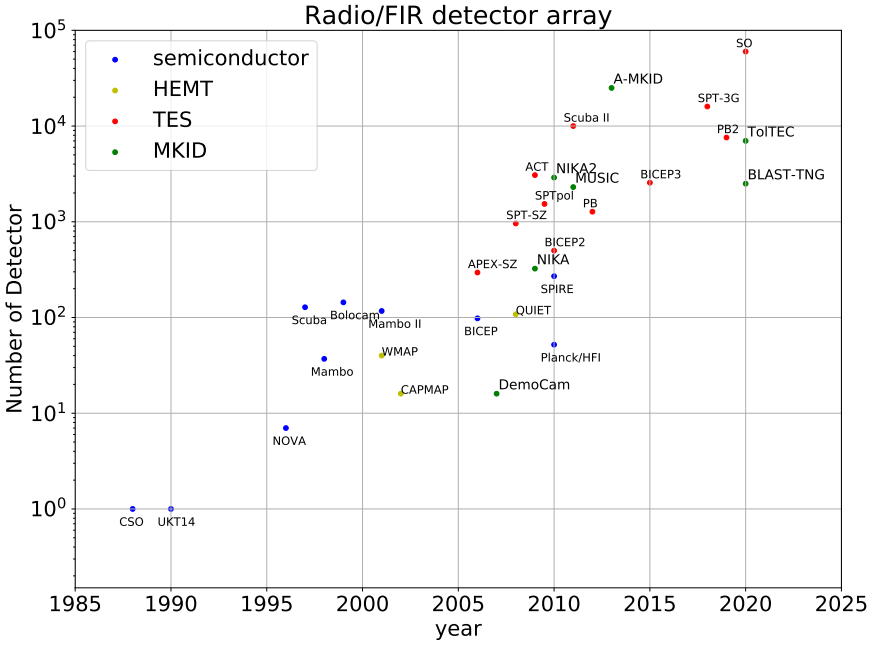

FIGURE 1.2: The number of focal plane detector as a function of year. The blue, yellow, red, and green dots show the experiment using semiconductor detector, HEMT, TES, and MKID, respectively.

ideal operation temperature of the MKID must be at least 4 times less than the superconducting transition temperature, T_c, otherwise it is hard to perform sensitive measurement due to thermal noise. Since the transition temperature of the typical metals which have been applied to MKID is in the range from 1 to 10 K, the focal plane must be cooled down to sub-Kelvin. To realize sub-Kelvin, special refrigerators are used. When the required temperature is $250 - 300$ mK, the Helium 3 sorption refrigerator is used. The duration to keep $250 - 300$ mK by the sorption refrigerator is one day or a few days. Every day or a few day, the MKID is once warmed up above the transition temperature and cooled down below the transition temperature again. Since the performance of the MKID changes every cooling cycle due to the tiny environment difference of the superconducting transition, we have to perform calibration of the performance of the MKID, especially its responsivity, every cooling cycle. Conventionally, the calibration of responsivity of MKID has been performed by measuring the change of the response when the temperature of the detector mount plate is heated up by controlling the heater attached to the mount plate as shown in Chapter 4. This method is inevitable from following systematic error. It always accompanies uncertainties whether the plate temperature measured by the thermometer coincides with the detector temperature. This method is also time consuming. It takes several hours for every calibration. Therefore, a few 10% of the observational time is consumed by the responsivity calibration. The invention of the novel calibration method of the MKID responsivity is highly demanded.

The other problem is that the $1/f$ type noise always appears [43] and it limits the performance in the low sampling frequency. This noise is supposed to be attributed to the two level system (TLS) [44, 45] formed in the interface of the superconducting material and substrate. Hereafter, we refer this noise as the TLS noise. To realize the photon noise limit high sensitivity MKID down to low sampling frequency, we have to mitigate the TLS noise in someway.

Aperture Diameter	300 mm
Optics system	Cross Dragone
Field of View	$\pm$10 deg
Detector	MKID
Frequency band	145 GHz, 220 GHz
Angular resolution	0.6 deg for 145 GHz, 0.4 deg for 220 GHz
Scan speed	120 deg/s
Sky coverage	44% of the full sky

TABLE 1.1: The concept of the GroundBIRD telescope[54]

The third problem is that there is not method to measure the superconducting transition temperature of the hybrid type MKID [46, 42] which is used two superconducting material for the resonator. The superconducting transition temperature of the MKID is one of the crucially important parameters to fix the design of MKID and evaluate performance. The hybrid type MKID has been widely used for the astronomical observation because of its merits as described in Chapter 2. Invention of the novel method which is able to measure the transition temperature of the hybrid type MKID is highly demanded.

1.4 GroundBIRD experiment

1.4.1 Concepts of the experiment

GroundBIRD [47, 48, 49, 50, 51, 52, 53] is a ground-based CMB polarization experiment to probe the inflationary cosmology and to observe the precise optical depth to reionization. A photo of the GroundBIRD installed in the Teide observatory, Tenerife, Spain is shown in Figure 1.3. Enable to attack the reionization bump of the primordial B-mode CMB polarization from the ground by mitigating the $1/f$ atmospheric fluctuation, the GroundBIRD performs the rapid rotation scan around the zenith direction with inclining the telescope 30 degree from zenith at rotation speed of 20 rotations per minute, which corresponds to 3 seconds for one rotation. Because of the earth rotation 44% of the full sky area is covered in a day. This scanning strategy makes the GroundBIRD unique ground-based CMB experiment. Since the time response of MKID is significantly faster than TES and satisfies the requirements from the rapid rotation scan strategy, MKID is installed on the focal plane of the GroundBIRD. It makes possible not only to address the reionization bump but also to resolve the recombination bump by the GroundBIRD. The GroundBIRD starts test observation from September 2019 at Teide observatory in Institute de Astrofisca de Canaries (IAC). Mainly, RIKEN, Kyoto University, Tohoku University, Korea University and IAC join the project. The summary of concepts of the GroundBIRD experiment is shown in Table 1.1.

The GrououndBIRD has three main features.

- Rapid rotation scan
- Cold optics
- Superconducting detector MKID

Some details of these features are explained in the followings.

FIGURE 1.3: A photo of the GroundBIRD installed in the Teide observatory, Tenerife, Spain. The photo is taken by J. Suzuki (Kyoto University)

Rapid rotation scan

The key feature of the GroundBIRD telescope is the rapid rotation scan around the zenith direction with inclining the telescope 30 deg from zenith at 20 rotations per minute, which corresponds to be 3 seconds for one rotation. By this observational method, a scale of the sky larger than a few 10th degree is covered faster than the 1/f atmospheric fluctuation. Because of the earth rotation and rapid scanning, 44% of the full sky area will be covered in a day. It makes possible to address the CMB polarization signal down to the multipole of $l \sim 6$.

Cold optics

To enable high sensitive observations, all optical components are installed in the cryostat which is cooled down to 4 K with pulse tube cooler (PT415, Cryomech. Co. LTD). To enable rapid rotation scan, the compact cryostat is adopted to the GroundBIRD. The telescope of the GroundBIRD is Cross Dragone reflecting mirror system [55]. The first and second mirrors are mounted inside of the 4 K shield in order to reduce thermal radiation from the surface of the mirrors in Figure 1.4.

Superconducting detector MKID

The GroundBIRD experiment uses MKID [56, 57] as a focal plane detector. The fast time response matches with the rapid rotation scan adopted by the GroundBIRD. Due to the fast time response (< 100 μs), the GroundBIRD can observe in the diffraction limit. This also allows GroundBIRD to observe the recombination bump ($l \sim 100$). The detail detection mechanism of the MKID are summarized in

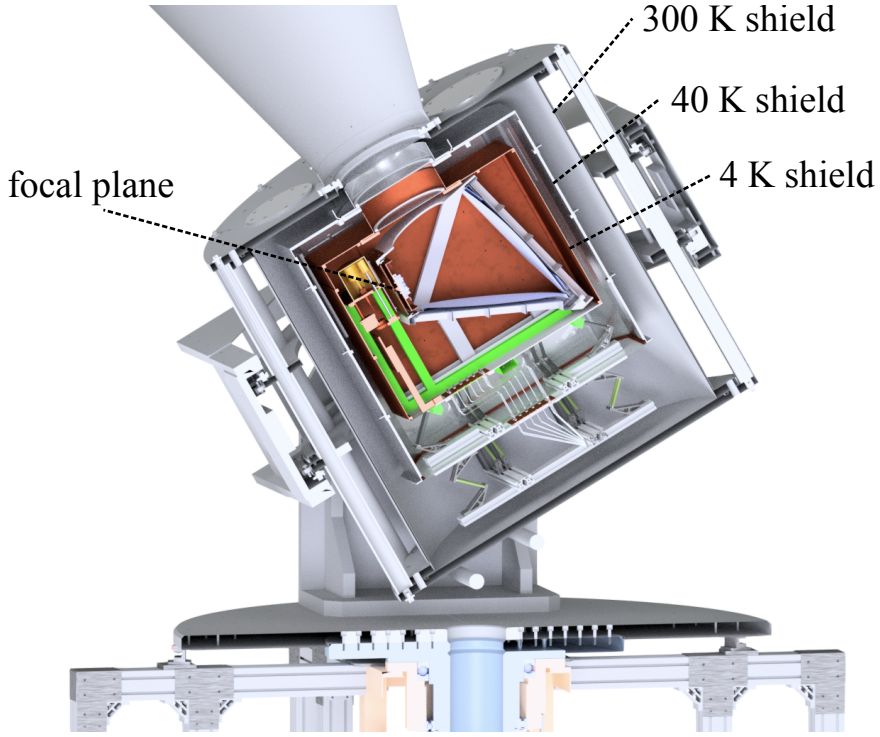

FIGURE 1.4: The CAD image of the GroundBIRD cryostat designed by H. Watanabe (RIKEN). The first and second mirrors are mounted inside of the 4 K shield in order to reduce thermal radiation from the surface of the mirrors.

Chapter 2. The GroundBIRD has two frequency band whose central frequencies are 145 GHz and 220 GHz, respectively, to enable high accuracy removal of the foreground emission shown in Figure 1.5. The amplitude of the foreground emission is higher than the expected amplitude of the primordial B-mode CMB polarization. In the frequency bands adopted by the GroundBIRD, the dominant component of the foreground emission is thermal emission from the interstellar dust. The focal plane is cooled down to 250 mK with the Helium 3 sorption refrigerator.

1.4.2 Requirements for the GroundBIRD instruments

The noise equivalent temperature (NET) and noise equivalent power are the fundamental parameters which characterize the sensitivity of the direct detectors. Roughly saying, the NET (NEP) is the source temperature (power) when the source is observed for one second (hertz), a signal-to-noise ratio becomes 1. The NEP of MKID [57, 58] is given by

$$NEP = \sqrt{\frac{2h\nu P_{\mathrm{rad}}(1+\eta_{\mathrm{opt}}\eta_{\mathrm{em}}\bar{n}) + 4\Delta P_{\mathrm{rad}}/\eta_{\mathrm{pb}}}{\eta_{\mathrm{opt}}}}, \tag{1.2}$$

where the first two terms come from photon noise of atmosphere or source when the blackbody source with temperature of T_{amb}, is observed, that is the occupation number of $\bar{n}$ is given by

$$\bar{n} = \frac{1}{\exp\left(\frac{h\nu}{k_{\mathrm{B}}T_{\mathrm{amb}}}\right) - 1}, \tag{1.3}$$

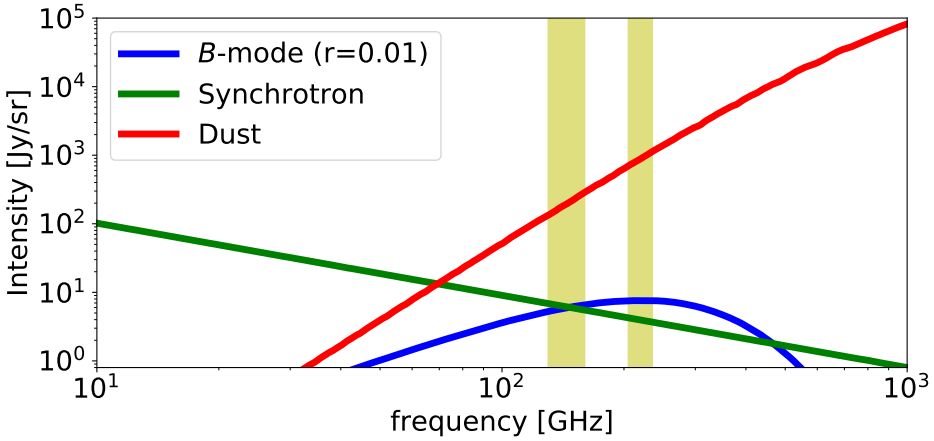

FIGURE 1.5: The expected B-mode polarization (blue line), synchrotron (green line), and dust intensity (red line) as a function of frequency. The yellow region shows the observational frequency band of the GroundBIRD. The foreground and the expected B-mode spectrum is analysed and calculated by M. Nashimoto (NAOJ)

the third term comes from the intrinsic noise of MKID device. The sum of the photon noise and the intrinsic noise of MKID is called BLIP noise (Background LImited Performance noise) noise. $P_{\rm rad}$ is the radiation power of the source or the atmosphere, $\eta_{\rm em}$ is the emissivity of the source or the atmosphere, Δ is the gap energy of the superconductor given by $\Delta = 1.76 k_{\rm B} T_c$ where T_c is the superconducting transition temperature [59] and $k_{\rm B}$ is the Boltzmann constant, $\eta_{\rm pb}$ is the pair braking efficiency [60, 61], ν is the optical frequency, and h is the Planck constant. The noise equivalent temperature in Rayleigh–Jeans Law (RJ) limit is given by

$$NET_{\rm RJ} = \frac{\sqrt{2} NEP}{k_{\rm B} \int F(\nu) {\rm d}\nu}, \tag{1.4}$$

where $F(\nu)$ is the filter transmission. The noise equivalent temperature for CMB is given by

$$NET_{\rm CMB} = NEP \left(\frac{\partial B(\nu, T)}{\partial T} \right)^{-1}_{T=T_{\rm CMB}}, \tag{1.5}$$

where

$$\left(\frac{\partial B(\nu, T)}{\partial T} \right)_{T_{\rm CMB}} = \exp\left(\frac{h\nu}{k_{\rm B} T_{\rm CMB}} \right) \left(\frac{h\nu / k_{\rm B} T_{\rm CMB}}{\exp\left(\frac{h\nu}{k_{\rm B} T_{\rm CMB}} \right) - 1} \right)^2, \tag{1.6}$$

where $T_{\rm CMB} = 2.725$ K is the temperature of CMB.

The sensitivity of the GroundBIRD must be achieved the photon noise limit of the atmosphere. The GroundBIRD telescope installs four optical filters that the first one (low pass filter) is installed at the aperture of the 40 K shield, the second one (low pass filter) is installed at the aperture of the 4 K shield, third one (low pass filter) at the 350 mK stage, and the final one (low pass and high pass filters) is installed in front of the detector at 250 mK stage. The transmittance of the vacuum window with anti reflection coating mounted at 300 K shield aperture is $\sim$ 96% [62]. The Figure 1.6 shows the transmission of the each optical filter and the total transmission of the GroundBIRD telescope as a function of frequency. The transmissions at 145 GHz

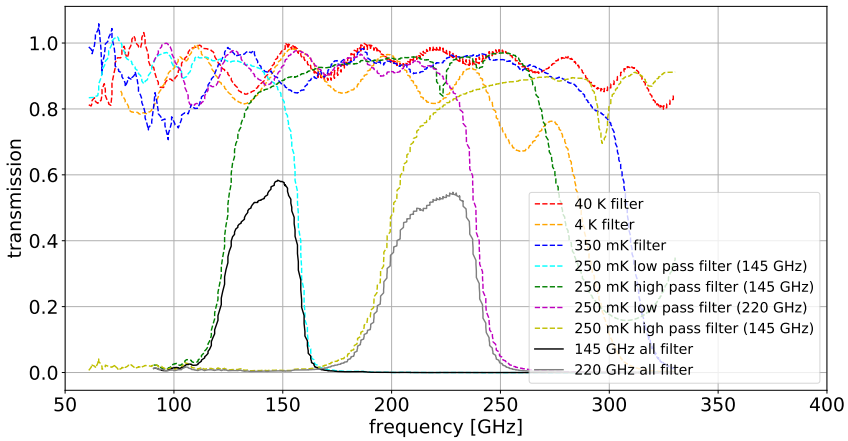

FIGURE 1.6: The filter transmission as a function of frequency. The red, orange, blue, cyan, green, magenta, and yellow dashed line show the transmission of the low pass filter at 40 K aperture, the low pass filter at 4 K aperture, the low pass filter at 350 mK stage, the low pass filter at 250 mK stage for 145 GHz, high pass filter at 250 mK stage for 145 GHz, low pass filter at 250 mK stage for 220 GHz, and high pass filter at 250 mK stage for 220 GHz, respectively. The black and grey solid line show the summation of the filter transmission with the transmission of the vacuum window for 145 GHz and 220 GHz, respectively.

band and 220 GHz band are optimized to be $\sim$ 50% for the GroundBIRD optical setup. The atmospheric emission is calculated using the precipitable water vapor (PWV) at the Teide observatory and the atmospheric model called ATM model [63]. The PWV is the depth of water in a column of the atmosphere. The annual mean of the PWV at the Teide observatory is 3.8 mm [64]. The atmospheric transmission is overlaid on the total transmission of the GroundBIRD optical filters in Figure 1.7.

The radiation power of the blackbody source with temperature of T, P_{rad}, is defined by

$$P_{\mathrm{rad}} = \frac{1}{2}\int \left(\frac{c}{\nu}\right)^2 F(\nu)B(\nu,T)\mathrm{d}\nu, \tag{1.7}$$

where c is the speed of light, ν is the frequency, and $B(\nu)$ is the source brightness. The source brightness for the blackbody source is given by

$$B(\nu,T) = \frac{2h\nu^3}{c^2}\frac{1}{\exp\left(\frac{h\nu}{k_{\mathrm{B}}T}\right)-1}. \tag{1.8}$$

The radiation power from atmospheric emission is given by

$$P_{\mathrm{rad,sky}} = \eta_{\mathrm{em}}P_{\mathrm{rad}}(T_{\mathrm{amb}}), \tag{1.9}$$

where T_{amb} is the ambient temperature, and η_{em} is the emissibity of the atmosphere ($1-$ atmospheric transmission). In the Rayleigh–Jeans limit, the radiation temperature of the atmospheric emission is given by

$$T_{\mathrm{sky}} = \frac{P_{\mathrm{rad,sky}}}{k_{\mathrm{B}}\int F(\nu)\mathrm{d}\nu}. \tag{1.10}$$

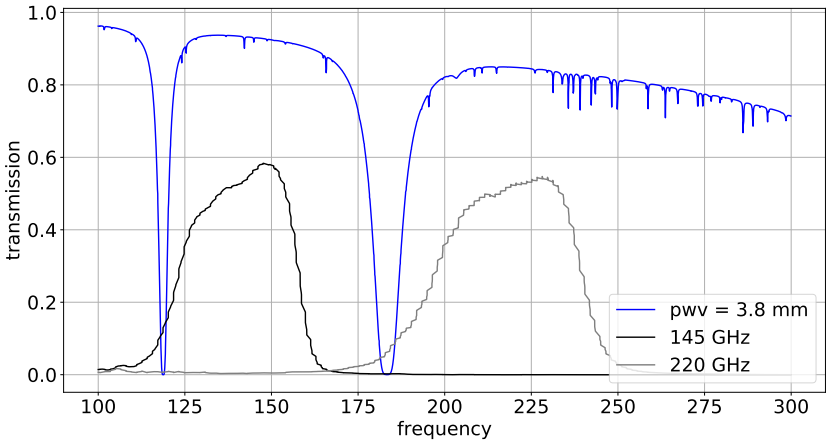

FIGURE 1.7: The black and gray lines show the sum of the filter transmission with the transmission of the vacuum window for 145 and 220 GHz, respectively. The blue line shows atmospheric transmission when PWV = 3.8 mm. We use ATM model for this calculation [63].

The radiation power of the atmosphere for PWV = 3.8 mm and $T_{\rm amb}$ = 273 K is obtained as

$$P_{\rm rad,145\ GHz} = 7.1\ {\rm pW}\ ({\rm for\ 145\ GHz}), \tag{1.11}$$

and

$$P_{\rm rad,220\ GHz} = 17.2\ {\rm pW}\ ({\rm for\ 220\ GHz}). \tag{1.12}$$

The absorbed power of the atmosphere for PWV = 3.8 mm and $T_{\rm amb}$ = 273 K in MKID is obtained as

$$P_{\rm abs,145\ GHz} = 7.1\eta_{\rm opt}\ {\rm pW}\ ({\rm for\ 145\ GHz}), \tag{1.13}$$

and

$$P_{\rm abs,220\ GHz} = 17.2\eta_{\rm opt}\ {\rm pW}\ ({\rm for\ 220\ GHz}), \tag{1.14}$$

where $\eta_{\rm opt}$ is the optical efficiency which is the ratio of the absorbed power by the detector to the incoming radiation power to the detector. The brightness temperatures of the atmosphere for PWV = 3.8 mm and $T_{\rm amb}$ = 273 K at two GroundBIRD frequency bands are given by

$$T_{\rm sky,145\ GHz} = 27\ {\rm K}\ ({\rm for\ 145\ GHz}), \tag{1.15}$$

and

$$T_{\rm sky,220\ GHz} = 51\ {\rm K}\ ({\rm for\ 220\ GHz}). \tag{1.16}$$

For an aluminum MKID (T_c = 1.28 K [65] and $\eta_{\rm pb}$ = 0.57 [60, 61]). The noise equivalent power of the GroundBIRD with the prototype MKID with $\eta_{\rm opt}$ = 0.39 [54, 66, 67] for 145 GHz is given by

$$NEP_{\rm sky,145\ GHz} = 1.0\times10^{-16}\ {\rm W}/\sqrt{\rm Hz}\ ({\rm for\ 145\ GHz}), \tag{1.17}$$

and with $\eta_{\rm opt}$ = 0.30 [54, 68, 67] for 220 GHz is given by

$$NEP_{\rm sky,220\ GHz} = 1.9\times10^{-16}\ {\rm W}/\sqrt{\rm Hz}\ ({\rm for\ 220\ GHz}). \tag{1.18}$$

The noise equivalent temperature in Rayleigh–Jeans limit with $\eta_{\rm opt} = 0.39$ for 145 GHz is given by

$$NET_{\rm sky-RJ,145\ GHz} = 530\ \mu{\rm K}\sqrt{\rm s}\ ({\rm for\ 145\ GHz}), \tag{1.19}$$

and with $\eta_{\rm opt} = 0.30$ for 220 GHz is given by

$$NET_{\rm sky-RJ,220\ GHz} = 813\ \mu{\rm K}\sqrt{\rm s}\ ({\rm for\ 220\ GHz}). \tag{1.20}$$

The noise equivalent temperature for CMB observation [67] with $\eta_{\rm opt} = 0.39$ for 145 GHz is given by

$$NET_{\rm sky-CMB,145\ GHz} = 860\ \mu{\rm K}\sqrt{\rm s}\ ({\rm for\ 145\ GHz}), \tag{1.21}$$

and with $\eta_{\rm opt} = 0.30$ for 220 GHz is given by

$$NET_{\rm sky-CMB,220\ GHz} = 2384\ \mu{\rm K}\sqrt{\rm s}\ ({\rm for\ 220\ GHz}). \tag{1.22}$$

Based on these results, the expected achievable sensitivity of the tensor-to-scalar ratio r after three years observations of the GroundBIRD is estimated to be $r = 0.29$ [69]. Although this is about 4 times larger than the current upper limit on r constrained from the observations of the recombination bump [12], the role of the GroundBIRD is the pathfinder to show that the scan strategy adopted by GroundBIRD is able to mitigate the atmospheric fluctuation and able to achieve the designed sensitivity against the reionization bump from the ground-based observation.

The requirements for the MKID to achieve above mentioned performance are summarized as follows;

- The detector performance is limited by BLIP noise.
- The TLS noise becomes prominant only below the rotation frequency of the GroundBIRD telescope (0.3 Hz).
- The time constant of MKID is less than sampling speed (1 ms).

As shown in Chapter 3, the performances of the prototype MKID mounted in the GroundBIRD which is fabricated based on the current design, are far from these requirements. Further improvement of the performance of MKID is mandatory.

1.5 Themes of this thesis

The themes of the thesis are developing novel methods to overcome fundamental problems of MKID listed in subsection 1.3.3 and fixing new design of MKID installed in the GroundBIRD which satisfies the requirements for MKID to extract the design performance of the GroundBIRD experiment as mentioned in subsection 1.4.2. We take two approaches. One is the development of the novel calibration methods in order to improve precision of the observation. The other is the development of the performance forecaster of MKID to shorten the research and development process dramatically until high performance MKID is fabricated.

The responsivity calibration of the MKID per each cooling cycle is important for the astronomical observation, because the performance of the MKID changes every cooling cycle. To calibrate the responsivity, the measurement of the MKID response during changing the device temperature is the standard method. However, the method needs a lot of time and causes the uncertainty of the responsivity due to the deference between the real device temperature and the temperature obtained by

the thermometer. We propose new method for the responsivity calibration in Chapter 4. The method is based on excess quasiparticles generated by microwave readout power signal. By changing microwave readout power signal from high power to low power, the excess quasiparticle decreases with time constant. This time constant is called quasiparticle lifetime and the time has an relation between the number of quasiparticles in the MKID. We evaluate the number of quasiparticles by the quasiparticle lifetime using theoretical formula. This measurement yields the responsivity. We apply this method for the real measurement using the MKID maintained at 285 mK. We also confirm the consistency between the results obtained using this method and the conventional calibration method in terms of the accuracy. Since our method is free from the above mentioned systematically accompanying in the conventional method, the our method provides much more secure results compared with the conventional method. Furthermore, the time duration consumed for the calibration dramatically shorted, down to 10 minutes, by our proposed method.

The superconducting transition temperature (T_c) of the MKID is an important parameter for both design and performance evaluation, because various parameters depend on the temperature. However, the hybrid type MKID, which is adopted for the GroundBIRD observation, is not able to be measured this temperature directly. In Chapter 5, we propose a new method to measure the T_c of MKID by rapidly changing the applied readout microwave signal. A small fraction of the readout power signal is deposited in the MKID, and the number of quasiparticles in the MKID increases with this applied power. Furthermore, the quasiparticle lifetime decreases with the number of quasiparticles. Therefore, we can measure the relation between the quasiparticle lifetime and the detector phase response by rapidly changing the readout power signal. From this relation, we estimate the intrinsic quasiparticle lifetime. This lifetime is theoretically modeled by T_c, the physical temperature of the device, and other known parameters. We obtain T_c by comparing the measured lifetime with theoretical model. Using an MKID fabricated with aluminium, we demonstrate this method at a 0.3 K operation. The results are consistent with those obtained by T_c measured by monitoring the transmittance of the readout microwave signal with the variation in the device temperature. The method proposed in Chapter 5 is applicable to the hybrid type MKID.

As mentioned in Chapter 3, the performance of the prototype MKID does not meet the GroundBIRD requirements. Further research and development is required to optimize performance of the MKID to the GroundBIRD observation. However, the one cycle from the design to evaluation is about three months. We have to iterate this cycle several times to feed back the results to new design. Dramatic reduction of the consumption for this research and development cycle is desired. For this purpose, we develop the forecaster which evaluate the performance of MKID quantitatively by setting environmental variables and design parameters. The development of the forecaster and evaluation of the prototype MKID performance are shown in Chapter 6. By inputting the design parameters of the prototype MKID into the forecaster, we confirmed that the TLS noise dominates over the BLIP noise below 100 Hz and that the main problem of the prototype MKID is its design. Since the total width of the coplanar waveguide (CPW) line made from Nb of the prototype MKID is too narrow, the contribution of the TLS noise became dominant. We propose new design MKID for the GroundBIRD observation and evaluate the performance using the forecaster in Chapter 7. We showed that the TLS noise is significantly reduced from that of the prototype MKID and is suppressed below the BLIP noise down to the GroundBIRD rotation speed (0.3 Hz).

Chapter 2

Microwave Kinetic Inductance Detector

In this chapter, we briefly introduce the detection mechanism and the noise of the MKID.

2.1 The detection mechanism of MKID

Microwave Kinetic Inductance Detector (MKID) was proposed by Caltech group in 2003 [56]. It consists of an antenna, a quarterwave resonator, and a readout feedline shown in Figure 2.1. The detection principle of the resonator, a photon which has $h\nu > 2\Delta$ (Δ is gap energy of the Cooper pairs) breaks Cooper pairs and generates quasiparticles shown in Figure 2.2. a. The Cooper pairs change inductance and quasiparticles increase resistance in the resonator. The equivalent circuit of the MKID consists of a capacitance C, a resistance R, and an inductance L coupled by the readout feedline with a capacitance shown in Figure 2.2. b. Each resonator has a resonance frequency ($\omega \propto 1/\sqrt{LC}$). It is equivalent to RLC circuit. When the photon is absorbed by the resonator, the surface impedance of the resonator is changed. It results the change of resonance frequency of the resonator, amplitude, and phase of the complex transmission shown in Figure 2.2. c, and Figure 2.2. d. The resonance frequency is adjusted by the length of the quarterwave resonator. Because of this characteristics, using frequency multiplexing, it is enable to read 100-1,000 pixels in a single readout line [39].

2.2 Quasiparticle dynamics

The microscopic description of the superconductivity was given by the BCS theory [59]. Inside of the superconductor, pair of two electrons with opposite spin and momentum called Cooper pair exist. The binding energy of the pair called gap energy depends on the temperature described by the BCS theory [59]. The gap energy at $T = 0$ K (T is the temperature) is given by

$$2\Delta_0 = 3.52 k_{\mathrm{B}} T_c, \tag{2.1}$$

where k_{B} is Boltzmann constant and T_c is the superconducting transition temperature. The gap energy depends on the superconducting transition temperature. For an aluminum, the twice of the gap energy $2\Delta_0$ is $\sim$ 360 μeV. The twice of the gap energy for an aluminum corresponds to the photon energy of 90 GHz.

A photon which has energy larger than the twice of the gap energy breaks the Cooper pairs and generates quasiparticles. The energy breaking Cooper pairs is not

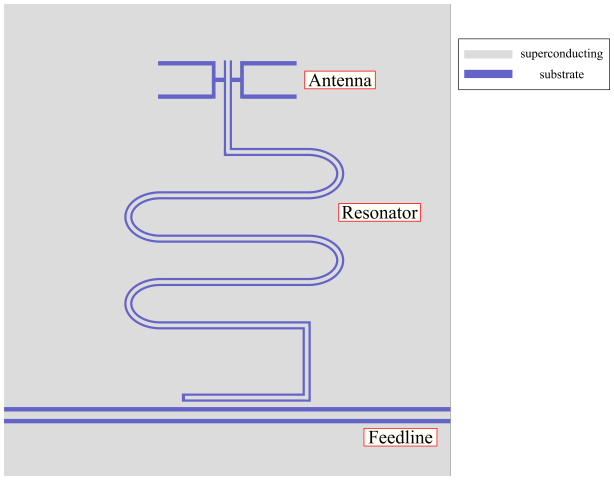

FIGURE 2.1: The MKID consists of antenna, resonator, and feedline. The superconducting thin film is on the substrate.

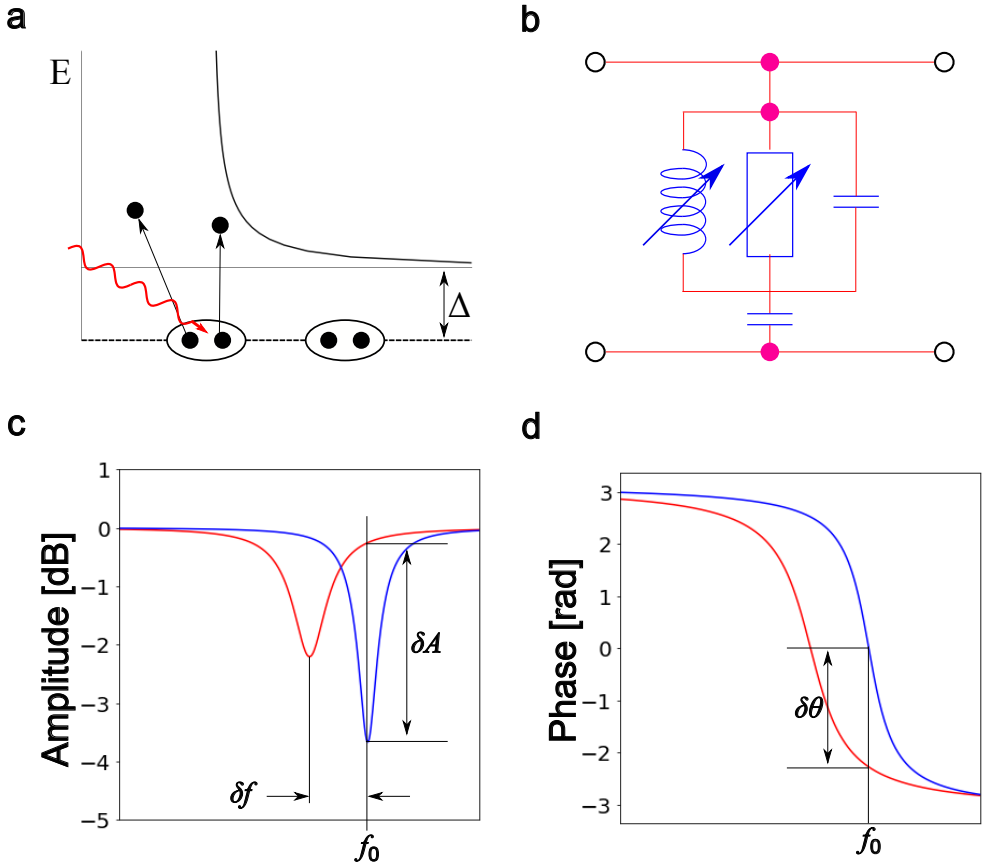

FIGURE 2.2: An illustration of the detection mechanism.

only photon energy ($h\nu > 2\Delta$) but also thermal energy [70] and the absorption of readout power [71, 72, 73, 74, 57, 75, 65]. The relation between the temperature and the number density of quasiparticles n_{qp} under the low temperature ($T \ll T_c$) , the dark and zero readout power condition [59] is given by

$$n_{\mathrm{qp}} = 2N_0\sqrt{2\pi k_{\mathrm{B}}T\Delta}\exp\left(-\frac{\Delta}{k_{\mathrm{B}}T}\right), \tag{2.2}$$

where Δ is the gap energy and N_0 is the single spin density of states at Fermi level ($N_0 = 1.74 \times 10^{10}\ \mathrm{eV}^{-1}\mu\mathrm{m}^{-3}$ for an aluminum [76, 77]). The number density of the quasiparticles exponentially increase with increasing the temperature. The number of quasiparticles in the MKID, N_{qp}, is given by $N_{\mathrm{qp}} = n_{\mathrm{qp}}V$, where V is the volume of the resonator.

The intensity of the source is measured by measuring the change of the number of quasiparticles in the MKID. The relation between the number of quasiparticles N_{qp} and the power absorbed in the MKID, P_{abs}, [78] is given by

$$\eta_{\mathrm{pb}}P_{\mathrm{abs}} = \frac{N_{\mathrm{qp}}\Delta}{\tau_{\mathrm{qp}}}, \tag{2.3}$$

where η_{pb} is the pair braking efficiency (nominal value for an aluminum is $\eta_{\mathrm{pb}} = 0.57$ [60, 61]), and τ_{qp} is the quasiparticle lifetime. The quasiparticle lifetime depends on the number of quasiparticles. The relation between quasiparticle lifetime and device temperature in the low temperature $T \ll T_c$ [79] is given by

$$\tau_{\mathrm{qp}} = \frac{\tau_0}{\sqrt{\pi}}\left(\frac{k_{\mathrm{B}}T_c}{2\Delta}\right)^{5/2}\sqrt{\frac{T_c}{T}}\exp\left(\frac{\Delta}{k_{\mathrm{B}}T}\right) = \frac{\tau_0}{n_{\mathrm{qp}}}\frac{N_0(k_{\mathrm{B}}T_c)^3}{2\Delta^2}, \tag{2.4}$$

where τ_0 is the electron phonon interaction time ($\tau_0 = 458$ ns for an aluminum [80]). The quasiparticle lifetime increases with decreasing the number of quasiparticles.

2.3 Complex conductivity

The change of the number of quasiparticles causes the change of the MKID response. The complex conductivity is the parameter which connect the number of quasiparticles with MKID response.

In the MKID, since the mean free path of the motion of the Cooper pair l is limited by the thickness of the MKID d, the size of the Cooper pair called coherence length ξ_0 is limited by the mean free path. This limit is called dirty limit ($d = l \ll \xi_0$). In the case of the dirty limit and $k_{\mathrm{B}}T, \hbar\omega < 2\Delta$ (ω is the angular frequency), the complex conductivity of real part σ_1 and imaginary part σ_2 given by the Mattis-Bardeen theory [81, 70] are simplified by

$$\frac{\sigma_1}{\sigma_N} = \frac{4\Delta}{\hbar\omega}\exp\left(-\frac{\Delta}{k_{\mathrm{B}}T}\right)\sinh\left(\frac{\hbar\omega}{2k_{\mathrm{B}}T}\right)K_0\left(\frac{\hbar\omega}{2k_{\mathrm{B}}T}\right), \tag{2.5}$$

and

$$\frac{\sigma_2}{\sigma_N} = \frac{\pi\Delta}{\hbar\omega}\left[1 - 2\exp\left(-\frac{\Delta}{k_{\mathrm{B}}T}\right)\exp\left(-\frac{\hbar\omega}{2k_{\mathrm{B}}T}\right)I_0\left(\frac{\hbar\omega}{2k_{\mathrm{B}}T}\right)\right], \tag{2.6}$$

where σ_N is the normal state conductivity, and I_0 and K_0 are the modified Bessel function of the first and second kind, respectively. The complex conductivity of the real part and imaginary part as a function of temperature are shown in Figure 2.3.

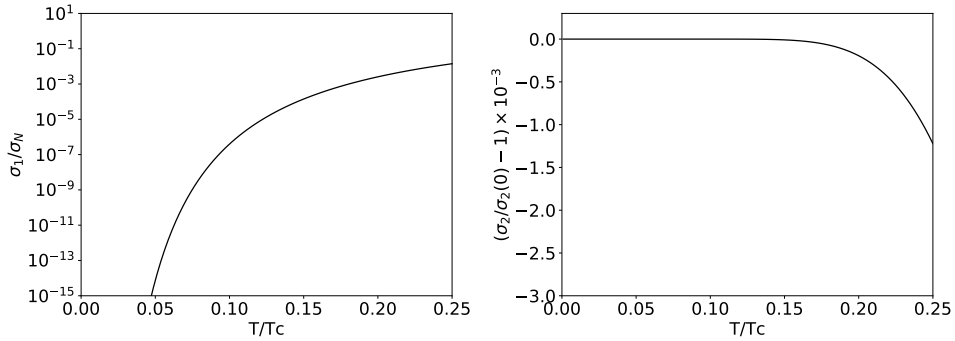

FIGURE 2.3: The left (right) figure shows the real (imaginary) part of complex conductivity as a function of temperature. We use 1.2 K as a superconducting transition temperature and 5 GHz as a readout frequency in this figure.

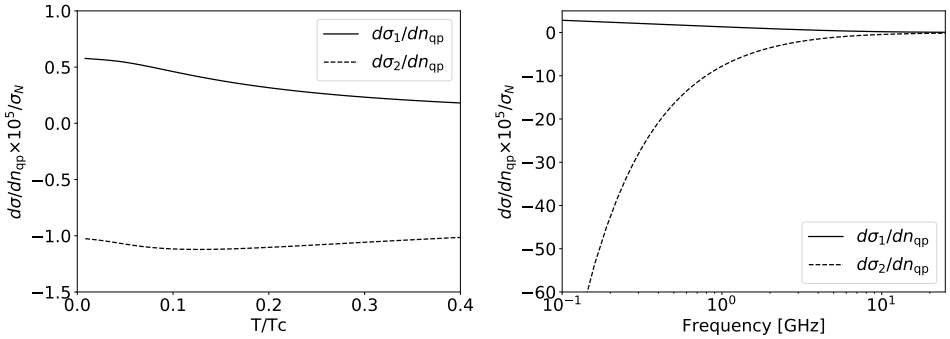

FIGURE 2.4: The responsivity of the complex conductivity as a function of temperature (left figure) and readout frequency (right). We use 1.2 K as a superconducting temperature and 5 GHz as a readout frequency in this figure.

Since the number of quasiparticles decreases with decreasing the temperature, the complex conductivity of real (imaginary) part decreases with decreasing (increasing) the temperature. The rate of change of the complex conductivity for the number density of quasiparticles [70] is given by

$$\frac{\mathrm{d}\sigma_1}{\mathrm{d}n_{\mathrm{qp}}} = \sigma_N \frac{1}{N_0\hbar\omega}\sqrt{\frac{2\Delta_0}{\pi k_\mathrm{B}T}}\sinh\left(\frac{\hbar\omega}{2k_\mathrm{B}T}\right)K_0\left(\frac{\hbar\omega}{2k_\mathrm{B}T}\right), \tag{2.7}$$

and

$$\frac{\mathrm{d}\sigma_2}{\mathrm{d}n_{\mathrm{qp}}} = \sigma_N \frac{-\pi}{2N_0\hbar\omega}\left[1+\sqrt{\frac{2\Delta_0}{\pi k_\mathrm{B}T}}\exp\left(-\frac{\hbar\omega}{2k_\mathrm{B}T}\right)I_0\left(\frac{\hbar\omega}{2k_\mathrm{B}T}\right)\right]. \tag{2.8}$$

The rate of change of the complex conductivity for the number density of quasiparticles of the real part and imaginary part as a function of temperature and readout frequency are shown in Figure 2.4. Based on Eq. 2.7 and Eq. 2.8, the complex conductivity lineally change with the number density of quasiparticles. It is known that the magnetic field penetrate into the surface of a superconductor. The characteristic length scale is called penetration depth. The penetration depth for the dirty limit

and low temperature ($T \ll T_c$) is given by [57]

$$\lambda_{\text{dirty}} \sim \sqrt{\frac{1}{\mu_0 \omega \sigma_2}}. \tag{2.9}$$

The penetration depth depends on the complex conductivity of the imaginary part.

2.4 Microwave resonator circuit

When the power is absorbed in the resonator, the surface impedance is also changed due to the change of the complex conductivity. The MKID response lineally depends on the change of the impedance in the low temperature $T \ll T_c$. Therefore we measure the intensity of the optical source as a MKID response.

2.4.1 Surface impedance

The surface impedance Z_s depends on the complex conductivity. In the dirty limit, the surface impedance [82, 83] is given by the following formula,

$$Z_s = \sqrt{\frac{i\mu_0\omega}{\sigma_1 - i\sigma_2}} \coth(\sqrt{i\omega\mu_0\sigma} d) = R_s + i\omega L_s, \tag{2.10}$$

where $\sigma = \sigma_1 - i\sigma_2$, R_s is the surface resistance of the resonator, and L_s is the surface inductance of the resonator. Using Eq. (2.9), the surface impedance is rewritten by

$$Z_s = \sqrt{\frac{i\mu_0\omega}{\sigma_1 - i\sigma_2}} \coth\left(\frac{d}{\lambda_{\text{dirty}}}\sqrt{1 + i\frac{\sigma_1}{\sigma_2}}\right). \tag{2.11}$$

In the low temperature $T \ll T_c$ and $\sigma_1 \ll \sigma_2$ limit, using $\coth(x + iy) \approx \coth(x) - \frac{iy}{\sinh^2(x)}$, the equation is approximated by

$$Z_s = i\omega\mu_0\lambda_{\text{dirty}} \coth\left(\frac{d}{\lambda_{\text{dirty}}}\right) + \mu_0\omega\lambda_{\text{dirty}}\frac{\sigma_1}{2\sigma_2}\beta_\lambda \coth\left(\frac{d}{\lambda_{\text{dirty}}}\right), \tag{2.12}$$

where $\beta_\lambda = 1 + \frac{2d/\lambda_{\text{dirty}}}{\sinh(2d/\lambda_{\text{dirty}})}$. Therefore the surface resistance and inductance is given by

$$R_s = \mu_0\omega\lambda_{\text{dirty}}\frac{\sigma_1}{2\sigma_2}\beta_\lambda \coth\left(\frac{d}{\lambda_{\text{dirty}}}\right), \tag{2.13}$$

and

$$L_s = \mu_0\lambda_{\text{dirty}} \coth\left(\frac{d}{\lambda_{\text{dirty}}}\right). \tag{2.14}$$

As a results, the change of the impedance is due to the change of the complex conductivity.

2.4.2 Resonance frequency

The MKID are transmission line resonators based on the coplanar waveguide (CPW). In the CPW resonator, the resonance frequency is determined by its phase velocity

$v_{\rm ph}$ and its length l. The phase velocity is given by

$$v_{\rm ph} = 1/\sqrt{C_l(L_g + L_k)}, \tag{2.15}$$

where L_k is the kinetic inductance per unit length, and L_g and C_l are geometric inductance and capacitance per unit length, respectively. For the quaterwave resonator ($\lambda_{\rm res} = 4l$, where $\lambda_{\rm res}$ is the wave length of the readout microwave.), using $\lambda_{\rm res} = 2\pi v_{\rm ph}/\omega_0$, the angular resonant frequency ω_0 is given by

$$\omega_0 = \frac{2\pi}{4l\sqrt{(L_g + L_k)C_l}}. \tag{2.16}$$

The geometrical inductance and capacitance of CPW line [84] are given by

$$L_g = \frac{\mu_0}{4}\frac{K(k')}{K(k)}, \tag{2.17}$$

and

$$C_l = 4\epsilon_0\epsilon_{\rm eff}\frac{K(k)}{K(k')}, \tag{2.18}$$

where $k = s/(s + 2w)$ (s: center strip width of CPW line, w: slot width between the center strip and groundplane), $k'^2 = 1 - k^2$, K is the complete elliptic integral of the first kind, ϵ_0 is the vacuum permittivity, and $\epsilon_{\rm eff}$ is the effective dielectric constant of the CPW line given by $\epsilon_{\rm eff} = (1 + \epsilon_{\rm sub})/2$ ($\epsilon_{\rm sub}$: relative permittivity of substrate). The kinetic inductance is originated from the inertia of the Cooper pairs in the superconductor. The relation between the kinetic inductance and the surface inductance [84] is given by

$$L_k = (g_c + g_g)L_s, \tag{2.19}$$

where g_c and g_g are the geometry factors of the central strip and the groundplane [84] describing the current density distribution in the CPW line given by

$$g_c = \frac{1}{4s(1-k^2)K^2(k)}\left[\pi + \ln\left(\frac{4\pi s}{d}\right) - k\ln\left(\frac{1+k}{1-k}\right)\right], \tag{2.20}$$

and

$$g_g = \frac{k}{4s(1-k^2)K^2(k)}\left[\pi + \ln\left(\frac{4\pi(s+2w)}{d}\right) - \frac{1}{k}\ln\left(\frac{1+k}{1-k}\right)\right], \tag{2.21}$$

where d is the thickness of the resonator. These expression provide by the good approximations for $d < s/20$ and $k < 0.8$ [84]. The kinetic inductance fraction α_k is the ratio of the kinetic inductance to the total inductance of the resonator per unit length given by

$$\alpha_k = \frac{L_k}{L_k + L_g}. \tag{2.22}$$

Using Eqs. (2.16), (2.17), (2.18), and (2.22), the resonance frequency f_r is rewritten by

$$f_r = \frac{c}{4l}\sqrt{\frac{1-\alpha_k}{\epsilon_{\rm eff}}}, \tag{2.23}$$

where c is the speed of light. The resonance frequency depends on the kinetic inductance. Since the kinetic inductance is changed by the radiation absorption, the resonance frequency is shifted. For high response of the resonance frequency due to the change of the complex conductivity, it is advantage to have a high kinetic inductance fraction.

2.4.3 Quality factor

The quality factor is a quantity that characterizes the loss in the resonator circuit. The quality factor is defined as the ratio of the energy stored in the resonator E_{stored} divided by the energy loss per one cycle P_{loss}/ω,

$$Q_r = \frac{\omega E_{\text{stored}}}{P_{\text{loss}}}. \tag{2.24}$$

The quality factor is divided coupling quality factor Q_c which depends on the coupling strength between the resonator and feedline and internal quality factor Q_i which characterize the internal loss given by

$$\frac{1}{Q_r} = \frac{1}{Q_i} + \frac{1}{Q_c}. \tag{2.25}$$

The internal quality factor include various losses. When the origin of the loss is quasiparticles, the internal quality factor [85] is given by

$$Q_i = \frac{\omega L_{\text{tot}}}{R} = \frac{1}{\alpha_k}\frac{\omega L_s}{R_s} = \frac{2}{\alpha_k \beta_\lambda}\frac{\sigma_2}{\sigma_1}, \tag{2.26}$$

where L_{tot} is the total inductance of the resonator per unit length given by $L_{\text{tot}} = L_{\text{g}} + L_{\text{k}}$, and total resistance of the resonator per unit length $R = (g_c + g_g)R_s$. The internal quality factor Q_i decreases with increasing absorbed power.

2.4.4 Quarterwave resonator

The MKID shown in Figure 2.1, use a quarterwave resonators, which consists of a transmission line with open end near the feedline and shorted end near the antenna. The resonator is coupled to the feedline with a capacitance C. The characteristic impedance of the feedline Z_0 is given by

$$Z_0 = \sqrt{\frac{L_k + L_g}{C_l}} = \sqrt{\frac{L_{\text{tot}}}{C_l}}. \tag{2.27}$$

The impedance of the quarterwave resonator, Z_{res}, [86] is given by

$$\begin{aligned} Z_{\text{res}} &= Z_0 \tanh(\alpha + i\beta)l \\ &= Z_0 \frac{\tanh \alpha l + i \tan \beta l}{1 + i \tan \beta l \tanh \alpha l} \\ &= Z_0 \frac{1 - i \tanh \alpha l \cot \beta l}{\tanh \alpha l - i \cot \beta l}, \end{aligned} \tag{2.28}$$

where $\alpha + i\beta$ is the complex propagation constant ($\alpha = R/2Z_0$ and $\beta = \omega\sqrt{LC}$ for the low loss line). Using Eq. (2.26), $Q_i = \beta/2\alpha$. We assume that the characteristic impedance of the resonator coincides with that of readout feedline. We redefine the

resonance frequency $\omega_{1/4}$ (the resonance frequency of the resonator without capacitance) and the readout frequency close to the resonance frequency $\omega = \omega_{1/4} + \delta\omega$. The product of the resonator length and complex propagation constant of the imaginary part is approximated by

$$\beta l = \frac{\pi}{2} + \frac{\pi\delta\omega}{2\omega_{1/4}}, \tag{2.29}$$

and

$$\cot\beta l = \cot\left(\frac{\pi}{2} + \frac{\pi\delta\omega}{2\omega_{1/4}}\right) = -\tan\frac{\pi\delta\omega}{2\omega_{1/4}} \approx \frac{-\pi\delta\omega}{2\omega_{1/4}}. \tag{2.30}$$

In the small loss, $\tanh(\alpha l) \approx \alpha l$ and $i\tanh\alpha l\cot\beta l = -i\alpha l\frac{\pi\delta\omega}{2\omega_{1/4}} \approx 0$. The impedance of the resonator is approximated by

$$Z_{\rm res} = Z_0\frac{1 + i\alpha l\pi\delta\omega/2\omega_{1/4}}{\alpha l + i\pi\delta\omega/2\omega_{1/4}} \approx \frac{Z_0}{\alpha l + i\pi\delta\omega/2\omega_{1/4}}. \tag{2.31}$$

Using $Q_i = \frac{\beta}{2\alpha}$ and $\alpha l = \frac{\beta l}{2Q_i} = \frac{1}{2Q_i}\frac{\pi}{2}\left(1 + \frac{\delta\omega}{\omega_{1/4}}\right)$, the impedance of the resonator is approximated by

$$Z_{\rm res} \approx Z_0\frac{4Q_i/\pi}{1 + 2iQ_i\frac{\delta\omega}{\omega_{1/4}}} = Z_0\frac{\frac{4Q_i}{\pi} - \frac{8iQ_i^2}{\pi}\frac{\delta\omega}{\omega_{1/4}}}{1 + 4Q_i^2\left(\frac{\delta\omega}{\omega_{1/4}}\right)^2}. \tag{2.32}$$

The quarterwave resonator is capacitively coupled to the feedline shown in Figure 2.1. Adding the capacitance C, the total impedance including the impedance of the resonator line and that of the capacitance is given by

$$Z = Z_{\rm res} + \frac{1}{i\omega C} = Z_0\frac{\frac{4Q_i}{\pi} - \frac{8iQ_i^2}{\pi}\frac{\delta\omega}{\omega_{1/4}} - \frac{i}{\omega CZ_0}\left(1 + 4Q_i^2\left(\frac{\delta\omega}{\omega_{1/4}}\right)^2\right)}{1 + 4Q_i^2\left(\frac{\delta\omega}{\omega_{1/4}}\right)^2}. \tag{2.33}$$

The new resonance frequency of the resonator and the capacitance ω_0 is shifted due to adding the capacitance. Since the imaginary part of total impedance is zero at the new resonance frequency, $\mathrm{Im}(Z) = 0$, the new resonance frequency is given by

$$\frac{\delta\omega}{\omega_{1/4}} = \frac{\omega CZ_0}{2Q_i}\left(-\frac{2Q_i}{\pi} \pm \sqrt{\frac{4Q_i^2}{\pi^2} - \frac{1}{\omega^2C^2Z_0^2}}\right) \approx -\frac{2\omega CZ_0}{\pi} \text{ or } 0, \tag{2.34}$$

where $\frac{1}{\omega^2C^2Z_0^2} \ll 4Q_i^2/\pi$ is used. We adopt the first solution. The relation between the resonance frequency of the resonator and the new resonance frequency including the quarterwave resonator and the capacitance is given by

$$\frac{\delta\omega}{\omega_{1/4}} = \frac{\delta\omega}{\omega_0} - \sqrt{\frac{2}{\pi Q_c}}, \tag{2.35}$$

where $Q_c = \frac{\pi}{2\omega^2 C^2 Z_0^2}$ is used. Using the new resonance frequency, the total impedance is given by

$$\frac{Z}{Z_0} = \sqrt{\frac{2Q_c}{\pi}} \frac{2Q_i \frac{\delta\omega}{\delta\omega_0} - i}{1 + 2iQ_r \frac{\delta\omega}{\omega_0} - 2iQ_i \sqrt{\frac{2}{\pi Q_c}}}. \tag{2.36}$$

The complex transmission S_{21} [86] as a function of readout frequency is given by

$$S_{21} = \frac{2}{2 + \frac{Z_0}{Z}} = \frac{Q_r/Q_i + 2iQ_i \frac{\delta\omega}{\omega_0}}{1 + 2iQ_r \frac{\delta\omega}{\omega_0}} = 1 - \frac{Q_r/Q_c}{1 + 2iQ_r \frac{f - f_r}{f_r}}, \tag{2.37}$$

where we use Eq. (2.25) and $\frac{\delta\omega}{\omega_0} = \frac{f - f_r}{f_r}$.

By measuring the complex transmission S_{21} as a function of readout frequency shown in Eq. 2.37 close to the resonance frequency, we can know the resonance frequency and the quality factors.

Coupling quality factor

We derive coupling quality factor Q_c following the procedure explored by P. J. de Visser [71]. The stored energy of the resonator is $\frac{1}{2} C_l l V_{\text{res}}^2$, where V_{res} is the voltage over resonator. The voltage over the coupling and resonator V is given by $V_{\text{res}} = Z/Z_{\text{res}} V$. The current is given by $I = V/Z = V_{\text{res}}/Z_{\text{res}}$. The lost power in feedline (P_{loss}^c) is given by

$$P_{\text{loss}}^c = |I^2| \frac{Z_0}{2} = \frac{V_{\text{res}}^2}{|Z_{\text{res}}|^2} \frac{Z_0}{2}. \tag{2.38}$$

At $\omega = \omega_0$, the impedance of the resonator is given by $|Z_{\text{res}}| = \frac{1}{\omega C}$. And using Eq. (2.15) and Eq. (2.27), $\omega C_l l = \frac{\pi}{2Z_0}$. Therefore, Q_c is given by

$$Q_c = \frac{\omega E_{\text{stored}}}{P_{\text{loss}}^c} = \frac{\omega \frac{1}{2} C_l V_{\text{res}}^2}{\frac{V_{\text{res}}^2}{|Z_{\text{res}}|^2} \frac{Z_0}{2}} = \frac{\pi}{2\omega^2 C^2 Z_0^2}. \tag{2.39}$$

2.5 Responsivity

In the measurement, we measure the phase and amplitude response of the each resonator. The response of the resonance frequency and inverse of internal quality factor have a linear relation with the phase and amplitude response in the small change of source intensity.

Using Eq. (2.37), the real part and imaginary part of the complex transmission S_{21} are given by

$$\text{Re}(S_{21}) = \frac{Q_r/Q_i + 4Q_r^2 \left(\frac{\delta\omega}{\omega_0}\right)^2}{1 + 4Q_r^2 \left(\frac{\delta\omega}{\omega_0}\right)^2} \approx \frac{Q_r}{Q_i}, \tag{2.40}$$

and

$$\text{Im}(S_{21}) = \frac{2Q_r \frac{\delta\omega}{\omega_0}(1 - Q_r/Q_i)}{1 + 4Q_r^2 \left(\frac{\delta\omega}{\omega_0}\right)^2} \approx 2Q_r \frac{\delta\omega}{\omega_0}(1 - Q_r/Q_i). \tag{2.41}$$

For small change, the real part of complex transmission S_{21} is given by

$$\delta \mathrm{Re}(S_{21}) = -\frac{Q_c Q_i}{(Q_c + Q_i)^2} \frac{\delta Q_i}{Q_i}. \tag{2.42}$$

To calculate the amplitude and the phase with respect to the resonance circle, the center point of the resonance circle is given by

$$x_c = \frac{1 + Q_r/Q_i}{2}. \tag{2.43}$$

Using Eq. (2.43), the amplitude A and phase θ of the MKID are given by

$$A = \frac{\sqrt{(\mathrm{Re}(S_{21}) - x_c)^2 + \mathrm{Im}(S_{21})^2)}}{1 - x_c} \approx \frac{|\mathrm{Re}(S_{21}) - x_c|}{1 - x_c}, \tag{2.44}$$

and

$$\tan(\theta) = \frac{\mathrm{Im}(S_{21})}{x_c - \mathrm{Re}(S_{21})}. \tag{2.45}$$

Near the resonance frequency ω_0, using $\delta A = A - 1$ and $\delta\theta \approx \tan(\theta)$ the responses of the MKID in amplitude and phase are given by

$$\delta A = \frac{-\delta \mathrm{Re}(S_{21})}{1 - x_c} = \frac{Q_c Q_i}{(Q_c + Q_i)^2} \frac{\delta Q_i}{Q_i} \frac{2Q_c}{Q_r} = \frac{2Q_r}{Q_i} \frac{\delta Q_i}{Q_i} = 2Q_r \delta \left(\frac{1}{Q_i} \right), \tag{2.46}$$

and

$$\delta\theta = \frac{\mathrm{Im}(S_{21})}{x_c - \mathrm{Re}(S_{21})} = -4Q_r \frac{\delta\omega}{\omega_0}. \tag{2.47}$$

Using Eq. (2.26), the responsivity of the inverse of the internal quality factor is given by

$$\delta \left(\frac{1}{Q_i} \right) = \frac{\alpha_k \beta_\lambda}{2} \left(\frac{\delta\sigma_1}{\sigma_2} - \frac{\sigma_1 \delta\sigma_2}{\sigma_2^2} \right) \approx \frac{\alpha_k \beta_\lambda}{2} \frac{\delta\sigma_1}{\sigma_2}, \tag{2.48}$$

and using Eq. (2.16), the responsvity of the resonance frequency is given by

$$\frac{\delta\omega_0}{\omega_0} = \frac{\alpha_k \beta_\lambda}{4} \frac{\delta\sigma_2}{\sigma_2}. \tag{2.49}$$

Therefore, the small response of amplitude δA and phase $\delta\theta$ are given by

$$\delta A = -\alpha_k \beta_\lambda Q_r \frac{\delta\sigma_1}{\sigma_2}, \tag{2.50}$$

and

$$\delta\theta = -\alpha_k \beta_\lambda Q_r \frac{\delta\sigma_2}{\sigma_2}. \tag{2.51}$$

The relation between the responses of MKID in amplitude and phase as a function of the number of quasiparticles [78] are given by

$$\frac{\delta A}{\delta N_{\mathrm{qp}}} = -\frac{\alpha_k \beta_\lambda Q_r}{\sigma_2 V} \frac{\delta\sigma_1}{\delta n_{\mathrm{qp}}}, \tag{2.52}$$

and

$$\frac{\delta\theta}{\delta N_{\mathrm{qp}}} = -\frac{\alpha_k \beta_\lambda Q_r}{\sigma_2 V} \frac{\delta\sigma_2}{\delta n_{\mathrm{qp}}}, \tag{2.53}$$

where V is the volume of the resonator, $\frac{1}{\sigma_2}\frac{\delta\sigma_1}{\delta n_{\rm qp}}$ and $\frac{1}{\sigma_2}\frac{\delta\sigma_2}{\delta n_{\rm qp}}$ are given by Eq. (2.6), Eq. (2.7), and Eq. (2.8). Using Eq. (2.3), the rate of the change of the amplitude and the phase rensponses for absorbed power [78] is given by

$$\frac{\delta A}{\delta P_{\rm abs}} = \frac{\eta\tau_{\rm qp}}{\Delta_0}\frac{\delta A}{\delta N_{\rm qp}}, \tag{2.54}$$

and

$$\frac{\delta\theta}{\delta P_{\rm abs}} = \frac{\eta\tau_{\rm qp}}{\Delta_0}\frac{\delta\theta}{\delta N_{\rm qp}}. \tag{2.55}$$

The responsivity of the MKID is proportional to the inverse of the quasiparticle, because the quasiparticle lifetime is proportional to the inverse of the number of quasiparticle. The responsivity of the MKID also depends on the volume of the resonator.

2.6 Power spectrum density

The spectral features of the noise are represented by the power spectrum density (PSD). The contribution of the noise component to the sampling frequency can be determined by PSD.

The power spectrum density is defined by the Fourier transform of the auto-correlation. The auto-correlation is defined by $R(t') =< x(t)x^*(t-t') >$. The power spectrum density S_x is given by

$$S_x \equiv 2F\{< x(t)x^*(t-t') >\}, \tag{2.56}$$

where F is Fourier transform.

2.6.1 Generation and recombination noise

The noise given by the fluctuation of the number of quasiparticles due to the thermal loading or the optical loading or so on is called generation and recombination noise [87, 80].

In general, the fluctuation of the number of the quasiparticles has a characteristic time scale (τ). The auto-correlation function is defined by $R_x(t') =< xx^* > \exp(-|t'|/\tau) = \sigma_x^2\exp(-|t'|/\tau)$. Using this equation, the PSD is given by

$$\begin{aligned} S_x &= 2\int_{-\infty}^{\infty}\sigma_x^2\exp(-|t'|/\tau)\exp(-i\omega t')dt' \\ &= 4\sigma_x^2\int_0^{\infty}\exp(-|t'|/\tau)\cos(\omega t')dt' \\ &= \frac{4\sigma_x^2\tau}{1+(\omega\tau)^2}, \end{aligned} \tag{2.57}$$

where ω is the sampling angular frequency. In the MKID, the fluctuation of the number of quasiparticles follows Poisson statistics. The σ_x is defined by the square root of the number of the quasiparticles $\sqrt{N_{\rm qp}}$. The time constant is defined by the quasiparticle lifetime $\tau_{\rm qp}$. Therefore, the power spectrum density of the quasiparticles system is given by

$$S_{N_{\rm qp}} = \frac{4N_{\rm qp}\tau_{\rm qp}}{1+(\omega\tau_{\rm qp})^2}. \tag{2.58}$$

Using the relation between the MKID response and the number of quasiparticles, $\delta A/\delta N_{\rm qp}$ and $\delta\theta/\delta N_{\rm qp}$, the power spectrum densities in amplitude and phase are given by

$$S_A = \frac{4N_{\rm qp}\tau_{\rm qp}}{[1+(\omega\tau_{\rm qp})^2][1+(\omega\tau_{\rm res})^2]}\left(\frac{\delta A}{\delta N_{\rm qp}}\right)^2, \tag{2.59}$$

and

$$S_\theta = \frac{4N_{\rm qp}\tau_{\rm qp}}{[1+(\omega\tau_{\rm qp})^2][1+(\omega\tau_{\rm res})^2]}\left(\frac{\delta \theta}{\delta N_{\rm qp}}\right)^2, \tag{2.60}$$

where $\tau_{\rm res}$ is the resonator ring time given by $\tau_{\rm res} = Q_r/\pi f_r$. Since the quasiparticle lifetime is proportional to the inverse of the number of quasiparticles, the product of the number of quasiparticles and the quasiparticle lifetime is constant.

2.6.2 Amplifier noise

The amplifier noise is not MKID specific noise. In general, the noise is limited by the thermal noise of the amplifier. The PSD of the amplifier noise in both amplitude and phase [85] is given by

$$S_{\rm system} = \frac{k_{\rm B}T_N}{P_{\rm read}}\left(\frac{2}{1-Q_r/Q_i}\right)^2 = \frac{4k_{\rm B}T_N}{P_{\rm read}}\left(1+\frac{Q_c}{Q_i}\right)^2, \tag{2.61}$$

where T_N is the noise temperature of the amplifier, and $P_{\rm read}$ is the readout power at the feedline.

2.6.3 Two Level System noise

In the phase PSD, the 1/f type noise due to the two level system [44, 45] will appear. It is known that the noise is came from the fluctuations by TLS with a dipole moment. The TLS noise changes the effective dielectric constant of the resonator $\epsilon_{\rm eff}$. The noise spectrum depends on the sampling frequency $S_\theta = f^\alpha$, where f is the sampling frequency. Previous MKID studies propose $\alpha = -0.5$ [88, 89, 90, 91, 92]. TLS noise model for the MKID is deeply studied by J. Gao Ph.D. thesis [43].

The following is the summary of the feature of PSD from the TLS noise.

- The TLS noise decreases with increasing the microwave readout power. The noise level follows $P_{\rm int}^{-1/2}$, where $P_{\rm int}$ is the internal power in the resonator [88, 89, 91, 93].
- The TLS noise depends on the structure of the MKID [46]. To use wide CPW line and wide slot of CPW line is effective to reduce the TLS noise [91, 89, 92] (see Appendix D).
- The TLS exists at an oxide on the top of the metal and the metal substrate interface. In order to reduce the effect, the nitride materials, e.g., NbTiN [91] and TiN [94] are effective, because the oxidization of the substrate is protected. The Hydrofluoric acid treatment to avoid the oxide at the substrate interface is also advantage [91].
- The TLS noise level decreases with increasing the device temperature [90].

2.7 Noise Equivalent power

The noise equivalent power is the parameter of the sensitivity for the photon detector. The definition of the noise equivalent power is the signal power that gives a signal-to-noise ratio of one in one hertz output bandwidth given by

$$NEP = \sqrt{\frac{< P^2(f) >}{\mathrm{d}f}}, \tag{2.62}$$

where $\mathrm{d}f$ is the output bandwidth and $< P(f)^2 >$ is the power fluctuation in the Fourier space.

2.7.1 The noise equivalent power from the generation and recombination noise

The noise of the MKID is limeted by the generation and recombination noise. The noise equivalent power $NEP_{\mathrm{G-R}}$ [95] is given by

$$NEP_{\mathrm{G-R}} = \frac{2\Delta_0}{\eta_{\mathrm{pb}}}\sqrt{\frac{N_{\mathrm{qp}}}{\tau_{\mathrm{qp}}}}. \tag{2.63}$$

The noise equivalent power due to generation and recombination has a temperature and the resonator volume dependence, $NEP_{\mathrm{G-R}} \propto \sqrt{V}\exp(-\Delta/k_{\mathrm{B}}T)$. In order to lower the NEP, the device temperature should lowered or the volume of the resonator should be reduced.

2.7.2 The BLIP noise equivalent power

In the optically bright condition, the noise equivalent power is limited by the quasiparticle fluctuation caused by the optical loading and the fluctuation of the photon number. The generation and recombination noise is limited by the quasiparticles generated by the optical loading. Using Eq. (2.3) and Eq. (2.63), the generation and recombination noise in the optically bright condition is given by

$$NEP_{\mathrm{GR}} = \sqrt{\frac{4\Delta_0 P_{\mathrm{rad}}}{\eta_{\mathrm{opt}}\eta_{\mathrm{pb}}}}, \tag{2.64}$$

where P_{rad} is the radiation power of the source and η_{opt} is the optical efficiency.

The NEP of the BLIP (Background LImited Performance) [57, 58] noise is given by

$$NEP_{\mathrm{BLIP}} = \sqrt{\frac{2h\nu P_{\mathrm{rad}}(1+\eta_{\mathrm{opt}}\bar{n}) + 4\Delta_0 P_{\mathrm{rad}}/\eta_{\mathrm{pb}}}{\eta_{\mathrm{opt}}}}, \tag{2.65}$$

where the fist two terms of right hand side is due to the fluctuation of the photon noise, the third term of that is the generation and recombination noise, ν is the optical frequency, and $\bar{n}$ is the photon occupation number given by

$$\bar{n} = \frac{1}{\exp\left(\frac{h\nu}{k_{\mathrm{B}}T}\right) - 1}, \tag{2.66}$$

where the thermal radiation with temperature of T is assumed as a source. The amplitude of the BLIP noise depends on the optical efficiency. The NEP decreases with increasing the optical efficiency.

Comparing the measured NEP and NEP_{BLIP}, we can know the optical efficiency if TLS noise and amplifier noise is lower than the BLIP noise, because the deference of these NEP is came from the optical efficiency.

2.8 Hybrid type MKID

The above discussion shows that reduction of the generation and recombination noise of MKID is realized by reducing the volume of the photon sensitive part of the resonator. The hybrid type MKID [46, 42] shown in Figure. 2.5 has been proposed to reduce the generation and recombination noise by reducing the volume of the photon sensitive part of the resonator. The antenna side of the resonator which must be sensitive to detection of photon, is made from the metal with low superconducting transition temperature such as aluminum. The rest of the resonator is made from the metal with high superconducting transition temperature such as niobium. It results in that only the antenna side is sensitive to the photon absorption and the rest of resonator is not sensitive to the photon absorption since the gap energy is too high to absorb millimeter wave photon. The volume of the resonator which is active for photon detection, is reduced dramatically. As a result, the generation and recombination noise of hybrid type MKID is able to be reduced significantly. Therefore, it is expected that the performance of the hybrid type MKID is much better than that of the MKID made from single superconducting metal. In addition, the hybrid type MKID has advantage to mitigate the TLS noise. In the case of single metal MKID, to reduce the volume of the resonator to improve the sensitivity, that is to reduce the generation and recombination noise, total volume of the resonator must be reduced. To realize this, the center strip width of the resonator must be reduced. As a result, contribution of the TLS noise becomes significant. On the other hand in the case of the hybrid type MKID, we do not have to reduce the center strip width of the resonator made from the metal with high superconducting transition temperature since it is not sensitive to photon detection. As a result, the effect of the TLS noise is suppressed while keeping low generation and recombination noise. Details of the physical processes related to these are introduced in Chapter. 6. In the hybrid type MKID, the groundplane and feedline are also made from the metal with high superconducting transition temperature.

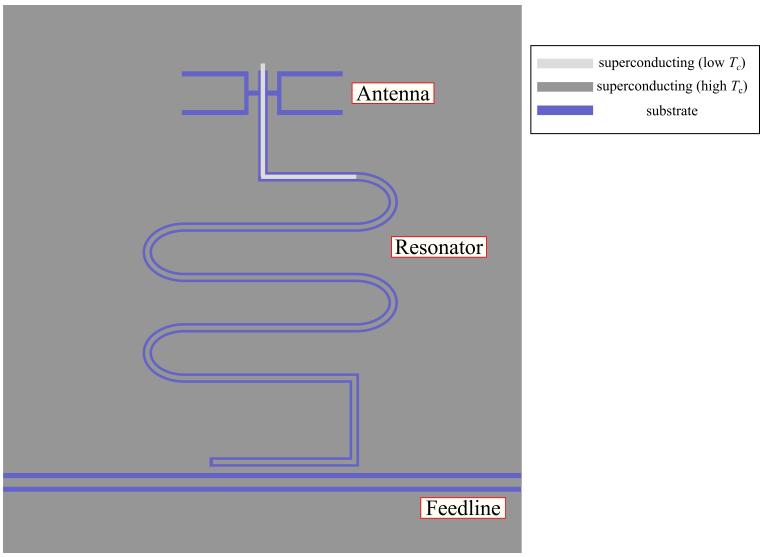

FIGURE 2.5: The geometry of the hybrid type MKID. The hybrid type MKID separates the resonator into two superconducting materials. The first part on the antenna side is used material with low superconducting transition temperature such as aluminum and the second part on the feedline side is used material with high superconducting transition temperature such as niobium.

Chapter 3

A performance measurement of prototype MKID for the GroundBIRD observation

We evaluate and discuss the performance of a prototype MKID for the GroundBIRD observation in the dark condition in this chapter.

3.1 An outline of the method to measure the noise equivalent power in the dark condition

The noise equivalent power is the important parameter which characterize the sensitivity of the photon detector. To obtain NEP of the MKID, we need to obtain the resonance frequency (f_r), quality factors (Q_r, Q_c, and Q_i), power spectrum density (S_θ and S_A), the responsivity ($\mathrm{d}\theta/\mathrm{d}P$ and $\mathrm{d}A/\mathrm{d}P$), and quasiparticle lifetime (τ_{qp}). The outline to obtain the NEP is shown in the following.

1. Measuring the complex transmission as a function of readout frequency close to the resonance frequency.
2. Fitting the complex transmission and obtaining the resonance frequency f_r, resonator quality factor Q_r, a coupling quality factor Q_c, and an internal quality factor Q_i.
3. Measuring the time order data at the resonance frequency f_r and obtaining the power spectrum density ($S_x, x = \theta, A$).
4. Measuring the quasiparticle lifetime (τ_{qp}) by the measurement of the cosmic ray muon hit.
5. Measuring the rate of the change of the MKID response for the power ($\mathrm{d}x/\mathrm{d}P$).
   (a) Measuring phase and amplitude response during the change of the device temperature
   (b) The temperature is converted to the number of quasiparticles (N_{qp}) with theoretical formula.
   (c) The rate of the change of the MKID response for the number of quasiparticles ($\mathrm{d}x/\mathrm{d}N_{\mathrm{qp}}$) is converted to the rate of the change of the MKID response for the power ($\mathrm{d}x/\mathrm{d}P$) using the quasiparticle lifetime, and known material parameters.
6. The noise equivalent power is evaluated by PSD , τ_{qp}, and $\mathrm{d}x/\mathrm{d}P$.

3.2 Measurement setup

3.2.1 Cryostat

The thermal shields of the cryostat are consist of 300 K, 40 K, and 4 K shield cooled by the Pulse Tube Cooler (PT415, Cryomech. Co. LTD). The Multi Layer Insulation which suppress thermal radiation are installed between $4-40$ K shield and $40-300$ K shield. The cooling stages are consist of 350 mK stage and 250 mK stage cooled by the sorption refrigerator (Gas-Light type, Simon chase. CO. LTD.). The magnetic shields (MS-FR, Hitach material) were set outside of the 40 K and 300 K shields; three sheets were set the wall of 40 K shield and three sheets (four sheets) were set outside the wall (bottom plate) of the 300 K shield to mitigate the geomagnetism effect. The MKID device is set inside of the light tight aluminum box to suppress stray light effect. The average temperature of the stages where an MKID devises is mounted is 285 mK.

3.2.2 The prototype MKID

The MKID device is fabricated in RIKEN [96, 97, 52]. This device consists of aluminum and niobium hybrid type MKID and has 10 resonators on a silicon wafer. The resonators are quarterwave resonator. The volume of an aluminum part is 920 μm^3 (the width, length, and thickness of the resonator are 4 μm, 2300 μm, and 100 nm, respectively.). The one of resonator which we evaluate has no antenna.

3.2.3 Readout setup

The readout setup is shown in Figure 3.1. We installed a variable attenuator and a warm amplifier (a variable attenuator and two warm amplifier) in the input (output) readout line. We adjusted the readout power to the feedline using the input variable attenuator. In the 4 K shield, we set HEMT amplifier, DC block and circulator. The analog board is used our original system which is called RHEA (Rhea is a High spEed Analog board) [98, 99, 100] and FPGA (field-programmable gate array, Kintex-7 Ultrascale KCU105 evaluation kit). The digital signal is converted to the analog signal using RHEA. The output signal from RHEA is mixed with local oscillator (LO) signal (up-convert). The signal came back from the cryostat is mixed with local oscillator (down-convert).

3.3 Complex transmission

At first, we measure the complex transmission S_{21} as a function of readout frequency f close to the resonance frequency shown in Figure 3.2. We fit the data with theoretical formula given by

$$t_{21} = a\exp(-2\pi i f\tau)\left[1 + c(f-f_r) - \frac{Q_r/Q_c\exp(i\phi_0)}{1+2iQ_r\left(\frac{f-f_r}{f_r}\right)}\right], \tag{3.1}$$

where a is the gain and phase shift through the system, τ is a cable delay, c is a slope of the baseline, Q_r is a resonator quality factor, Q_c is a coupling quality factor, f_r is a resonance frequency, and ϕ_0 is a impedance mismatch of the readout feedline [43, 102, 103]. From the fitting results, the resonance frequency and the quality factors

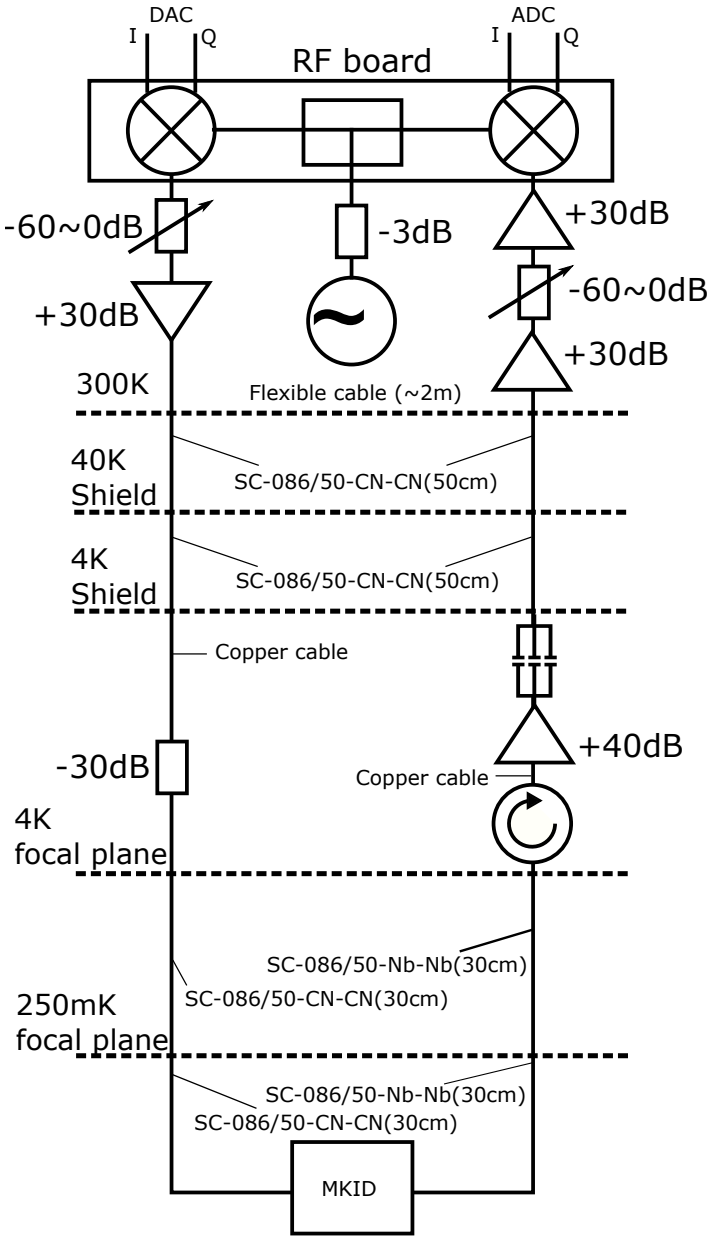

FIGURE 3.1: A diagram of the MKID readout system. The local oscillator (LO) is the NI Microwave Components FSL-0010, and the detail of the mixer is described in [101]. We used a variable attenuator, LDA-602E Vaunix. Co. LTD. We set attenuation value of input and output variable attenuator -11.5 dB and -17.5 dB, respectively. Output microwaves from the MKID is amplified by the low noise amplifier, LNF-LNC4_8C. and warm amplifiers, ZVE-8G+ Mini-Circuits.

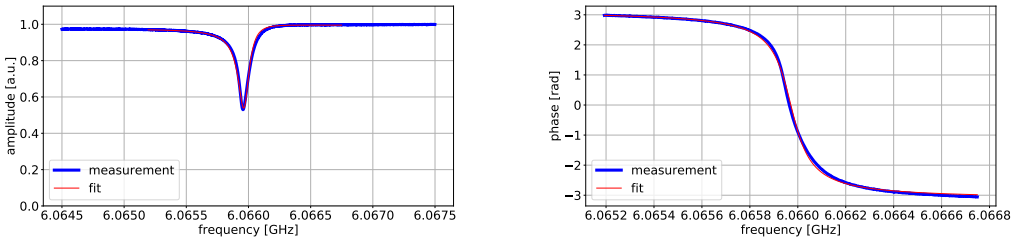

FIGURE 3.2: The amplitude (left) and phase (right) of the complex transmission S_{21} of the prototype MKID as a function of readout frequency. The blue and red line show the measurement data and fitting result, respectively.

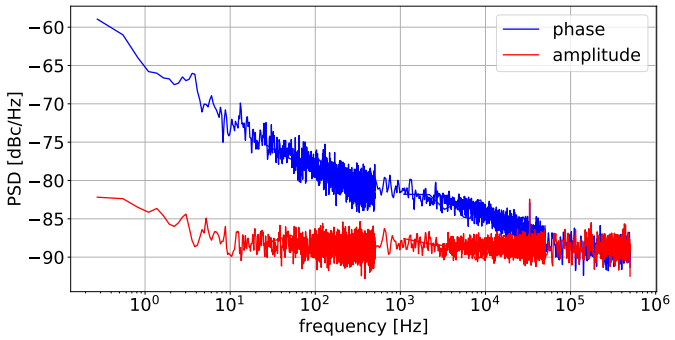

FIGURE 3.3: The PSD of the prototype MKID. The blue and red line show the phase and the amplitude of PSD for the prototype MKID. The PSD of phase is dominated by the 1/f type noise.

are obtained. An internal quality factor Q_i is defined by

$$\frac{1}{Q_r} = \frac{1}{Q_c}\cos\phi_0 + \frac{1}{Q_i}. \tag{3.2}$$

The Q_r and f_r of one of the prototype MKID are 4.88×10^4 and 6.07 GHz from the fitting, respectively.

3.4 Power spectrum density (PSD)

We perform the measurement and on resonance frequency and off resonance frequency simultaneously to subtract readout noise. The detail subtraction method of the readout subtraction is shown in Ref. [97]. After the noise subtraction, we can obtain PSD by analysing time ordered data using Welch method shown in Figure. 3.3. The PSD of phase has a high 1/f type noise which is supposed to be caused by the two level system. The roll-off feature appeared in the phase PSD is originated from the resonator ring time. The PSD of amplitude is limited by the amplifier noise.

3.5 Noise equivalent power (NEP)

To convert from the PSD to NEP, we evaluate the quasiparticle lifetime using cosmic ray muon hit measurement and responsivity using change of the physical temperature of the device.

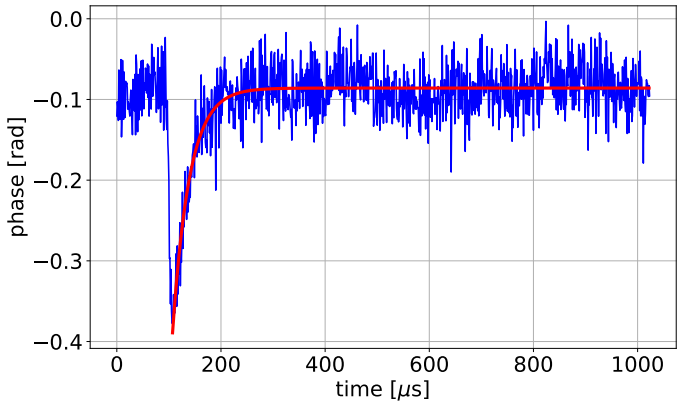

FIGURE 3.4: The phase response with the cosmic ray muon hit. The blue line and red line show the measurement data and the fitting result, respectively.

3.5.1 The quasiparticle lifetime measurement

We measured the quasiparticle lifetime by the cosmic ray muon hit. When the cosmic ray muon penetrate and deposit the energy in the detector, the Cooper pairs are broken and quasiparticles are generated. The phase response is changed with time constant characterized by the quasiparticle lifetime shown in Fiugre. 3.4. The cosmic ray muon hit widely change the phase response. Therefore we correct the deviation of the phase response from linear response using the following formula [43, 104],

$$\theta' = 2\tan(\theta/2). \tag{3.3}$$

The fit function is given by

$$\theta' = \delta\theta \exp\left(-\frac{t-t_0}{\tau_{\rm qp}}\right) + \theta_{\rm base}, \tag{3.4}$$

where t is the time, $\delta\theta$ is the phase response of MKID, t_0 is the time of the muon hit, and $\theta_{\rm base}$ is the base line of phase. The quasiparticle lifetime of the prototype MKID is 27.5 ± 0.4 μs with cosmic ray muon hit measurement using 100 samples.

3.5.2 Changing the physical temperature of the device

We measure the temperature dependence of the MKID response controlling the temperature of the MKID. The relation between the number of quasiparticles and temperature is given by the following formula [59],

$$N_{\rm qp} = 2N_0 V\sqrt{2\pi k_{\rm B}T\Delta}\exp\left(-\frac{\Delta}{k_{\rm B}T}\right), \tag{3.5}$$

where N_0 is the single spin density of states at Fermi level ($N_0 = 1.74\times10^{10}$ eV$^{-1}\mu$m^{-3} for an aluminum [76, 77]), $k_{\rm B}$ is the Boltzmann constant, V is the aluminum volume of the prototype MKID, and Δ is the superconducting gap energy given by $\Delta = 1.76k_{\rm B}T_c$. We use $T_c = 1.28$ in our past measurement result [65] in the analysis. The phase response of MKID is calculated by the change of the resonance frequency (δf_r), the resonance frequency (f_{r0}), and resonance quality factor (Q_{r0}) at original

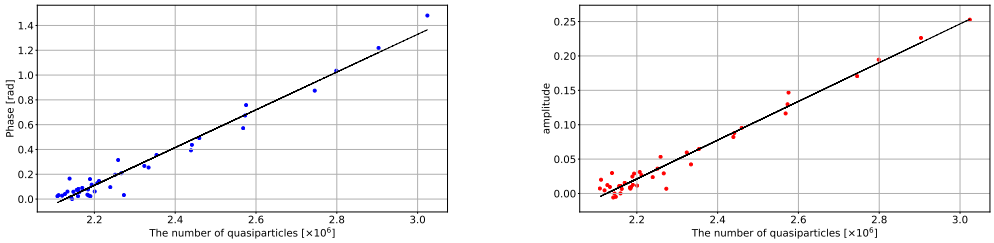

FIGURE 3.5: The responsivity of phase (left figure) and amplitude (right figure) for the perototype MKID. The blue and red dots are measurement data. The black line shows the linear fitting results.

position given by

$$\delta\theta = -\frac{4Q_{r0}}{f_{r0}}\delta f_r. \tag{3.6}$$

The amplitude response of MKID is calculated by the change of the inverse of the internal quality factor ($\delta(1/Q_i)$) and the resonance quality factor at original position given by

$$\delta A = 2Q_{r0}\delta\left(\frac{1}{Q_i}\right). \tag{3.7}$$

We adopt Q_{r0} and f_{r0} at lowest temperature ($T = 285$ mK) in the analysis. The $\mathrm{d}\theta/\mathrm{d}N_{\mathrm{qp}}$ and $\mathrm{d}A/\mathrm{d}N_{\mathrm{qp}}$ are $(1.52 \pm 0.04) \times 10^{-6}$ rad and $(2.82 \pm 0.08) \times 10^{-7}$, respectively shown in Figure 3.5. The relation between the MKID response and power [78] is given by

$$\frac{\mathrm{d}x}{\mathrm{d}P} = \frac{\eta_{\mathrm{pb}}\tau_{\mathrm{qp}}}{\Delta}\frac{\mathrm{d}x}{\mathrm{d}N_{\mathrm{qp}}}\ (x = A, \theta) \tag{3.8}$$

where η_{pb} is the pair braking efficiency (0.57 for an aluminum).

3.5.3 Noise Equivalent Power (NEP)

In the dark condition, the NEP of MKID is given by

$$NEP = \sqrt{S_x}\left(\frac{\mathrm{d}x}{\mathrm{d}P}\right)\sqrt{1+(2\pi f\tau_{\mathrm{qp}})^2}\sqrt{1+(2\pi f\tau_{\mathrm{res}})^2}\ (x = \theta, A), \tag{3.9}$$

where S_x is the power spectrum density, and τ_{res} is the resonator ring time given by $\tau_{\mathrm{res}} = Q_r/\pi f_r$. The NEP of the prototype MKID in the dark condition is shown in Figure 3.6. According to the results, the 1/f type noise due to the TLS noise in the phase is significantly higher than the generation and recombination noise. The noise level is limited by 1/f type noise due to the TLS noise. The NEP in amplitude is limited by the amplifier noise.

3.6 Discussions

The performance of the prototype MKID is far from the GroundBIRD observation requirements. The NEP of the MKID has a high 1/f type noise. It is higher than the generation and recombination noise. For the photon noise limit observation, we need to reduce this noise under the photon noise.

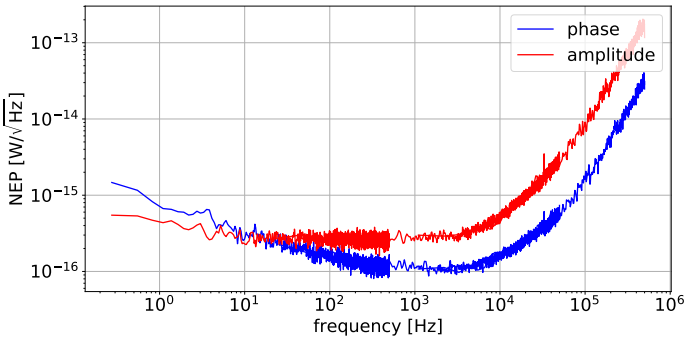

FIGURE 3.6: Noise Equivalent Power of the prototype MKID. The NEP of phase is dominated by the 1/f type noise.

Chapter 4

Novel calibration method for responsivity of MKID by changing power of readout microwaves

The responsivity calibration of the MKID per each cooling cycle is important for the astronomical observation, because the responsvity of the MKID changes every cooling cycle. To calibrate the responsivity, the measurement of the MKID response during changing the device temperature is the standard method. However, the method needs a lot of time and causes the uncertainty of the responsivity due to the deference between the real device temperature and the temperature obtained by the thermometer. We propose new method for the responsivity calibration. The method is based on excess quasiparticles generated by microwave readout power signal. By changing microwave readout power signal from high power to low power, the excess quasiparticle decreases with time constant. This time constant is called quasiparticle lifetime and the time has an relation between the number of quasiparticles in the MKID. We evaluate the number of quasiparticles by the quasiparticle lifetime using theoretical formula. This measurement yields the rate of the change of the phase response for the number of quasiparticles. We apply this method for the real measurement using the MKID maintained at 285 mK. We also compare the result using the proposed method and the results using conventional methods.

4.1 Conventional calibration methods of responsvity of MKID

For the astronomical observation using MKID, we need to convert the phase response of MKID to the power absorbed in the MKID. The rate of the change of the phase response for the absorbed power, $\mathrm{d}\theta/\mathrm{d}P$, [78] is given by

$$\frac{\mathrm{d}\theta}{\mathrm{d}P} = \frac{\eta_{\mathrm{pb}}\tau_{\mathrm{qp}}}{\Delta}\frac{\mathrm{d}\theta}{\mathrm{d}N_{\mathrm{qp}}} \tag{4.1}$$

where η_{pb} is a pair breaking efficiency (e.g. $\eta_{\mathrm{pb}} = 0.57$ for an aluminium [60, 61]), and $\mathrm{d}\theta/\mathrm{d}N_{\mathrm{qp}}$ is the rate of change of the phase response for the number of quasiparticles called responsivity. It is important to know the responsivity for the precise observations and development of an MKID design. There are two major calibration methods: a calibration by changing the physical temperature of an MKID device and a calibration by fitting the power spectral density (PSD). We propose third calibration method for the responsivity using readout microwave signal rapidly change.

4.1.1 Changing physical temperature of an MKID

Changing the physical temperature of an MKID device is the most standard calibration method [70]. For controlling the temperature of an MKID device, we set the heater at an MKID device (or we control the cooling power of the refrigerator). When the heater is warmed up, we measure the phase response of MKID. The temperature of the device is measured by the thermometer. The number of quasiparticles in the volume N_{qp} is calculated by the temperature with theoretical formula [59]:

$$N_{\mathrm{qp}} = 2N_0 V\sqrt{2\pi k_{\mathrm{B}} T\Delta}\exp\left(-\frac{\Delta}{k_{\mathrm{B}}T}\right), \tag{4.2}$$

where N_0 is the single spin density of states at the Fermi level (e.g., $N_0 = 1.74\times 10^{10}$ eV$^{-1}\mu$m^{-3} for an aluminium [76, 77]), V is the volume of the device, k_{B} is the Boltzmann constant, T is the detector temperature, and Δ is the gap energy. Based on BCS theory [59], the gap energy (Δ) in the low temperature condition ($T \ll T_c$, T_c is the superconducting transition temperature) is given by

$$2\Delta = 3.52\mathrm{k_B}T_c. \tag{4.3}$$

The superconducting transition temperature T_c and gap energy Δ of an aluminium is 1.2 K and 180 μeV. The phase response of MKID is calculated by the change of the resonance frequency (δf_r), the resonance frequency and quality factor at original position (typically selected in the lowest temperature) given by

$$\delta\theta = \frac{\delta\theta}{\delta f_r}\delta f_r = -\frac{4Q_{r0}}{f_{r0}}\delta f_r. \tag{4.4}$$

The resonance frequency and quality factor is obtained by fitting the complex transmission as a function of the readout frequency as mentioned in Chapter 3.3. $\mathrm{d}\theta/\mathrm{d}N_{\mathrm{qp}}$ is obtained by linear fitting the relation between the number of quasiparticles calculated by Eq. (4.2) and phase response of MKID calculated by Eq. (4.4).

However, this method has four main issues. The change of T is too large compared with the conditions in real operations which is typically 10 mK $-$ 100 mK. The difference of the temperature of the MKID device and that from the thermometer causes systematic uncertainty of responsivity. The excess power due to stray lights, readout microwave signal power causes excess quasiparticles as an offset to the Eq. (4.2). It take a long time to change the temperature and stabilization of the system.

4.1.2 Responsivity measurement using power spectral density (PSD)

The phase power spectral density (PSD, S_θ) due to the generation and recombination noise and system noise (X_{system}) [71] is given by

$$S_\theta(f) = \frac{4N_{\mathrm{qp}}\tau_{\mathrm{qp}}}{(1+(2\pi f\tau_{\mathrm{qp}})^2)(1+(2\pi f\tau_{\mathrm{res}})^2)}\left(\frac{\mathrm{d}\theta}{\mathrm{d}N_{\mathrm{qp}}}\right)^2 + X_{\mathrm{system}}, \tag{4.5}$$

where the first term of the right hand side is generation and recombination noise, f is the sampling frequency of the detector, τ_{res} is the resonator ring time given by $\tau_{\mathrm{res}} = Q_r/\pi f_r$, and X_{system} is the readout noise characterized by the low noise amplifier in the cryostat. By fitting the PSD with this formula, we can get responsivity $\mathrm{d}\theta/\mathrm{d}N_{\mathrm{qp}}$.

The biggest issue of this method is the effect of the Two Level System (TLS) noise[88, 43, 89] described in Chapter 2 . The TLS noise arises a frequency dependent

noise, i.e., 1/f type noise. This noise causes the uncertainty of fitting parameters. We can not obtain responsivity when the TLS noise level is higher than the generation and recombination noise level.

4.2 New responsivity calibration method by changing readout power rapidly

The number of quasiparticles N_{qp} depends on the readout microwave signal powers as mentioned in Ref. [71, 72, 73, 74, 57, 75, 65]. Based on this knowledge, we propose new responsivity calibration method. Figure 4.1 shows the diagram of our proposed method. The response of N_{qp} and θ under rapidly changing readout microwave signal power from high power to low power at $t = t_0$. N_{qp} decreases with the time constant. Likewise, the MKID phase response (θ) is also changed with time constant. The phase response as a function of the time is given by

$$\theta = \begin{cases} \theta_H & (t < t_0) \\ (\theta_H - \theta_L) \exp\left(-\frac{t-t_0}{\tau_{qp}}\right) & (t \geq t_0), \end{cases} \tag{4.6}$$

where θ_H and θ_L are the phase response before and after the power change, respectively. Using this method, the change of the phase response and the quasiparticle lifetime (τ_{qp}) can be obtained simultaneously. In order to obtain the number of quasiparticles, we change the τ_{qp} to the N_{qp} using the following formula [79, 80]:

$$N_{qp} = \frac{\tau_0 V}{\tau_{qp}} \frac{N_0 (k_B T_c)^3}{2\Delta^2}, \tag{4.7}$$

where τ_0 is the electron phonon interaction time (458 ns for an aluminium [80]). Using the various set of initial readout power, we obtain the phase response as a function of the number of quasiparticles. Fitting this relation, we can obtain responsivity.

4.3 Setup

We apply this method for the real measurements. The setup of the readout system inside and outside of the cryostat is shown in Figure 4.2. Our cryostat consists of three thermal shields (4 K, 40 K, and 300 K from inside to outside) [52]. They are cooled by the pulse tube refrigerator (PT415, Cryomech. Co. LTD). The magnetic shields (MS-FR, Hitach material) were set outside of the 40 K and 300 K shields; three sheets were set the wall of 40 K shield and three sheets (four sheets) were set outside the wall (bottom plate) of the 300 K shield. The MKID device is set inside of the light tight aluminum box to suppress stray light effect. The average temperature of the stages where an MKID devises is mounted is 285 mK. The stage is cooled by the helium sorption refrigerator (Gas-Light type, Simon chase Co. Ltd.). Our MKID device is fabricated in RIKEN [96, 97, 52]. This device consists of Al and Nb hybrid type quarterwave resonator and has 10 resonators on the wafer. The volume for Al part is 920 μm^3 (the length, width, and thickness is 2300 μm, 4 μm, and 100 nm, respectively.). The resonator we measure has no antenna. For dark condition, the resonant frequency and resonant quality factor are $f_{r0} = 6.07$ GHz and $Q_{r0} = 4.78 \times 10^4$, respectively. Our readout system has an direct down conversion logic with 200 MHz sampling speed [98, 99, 100].

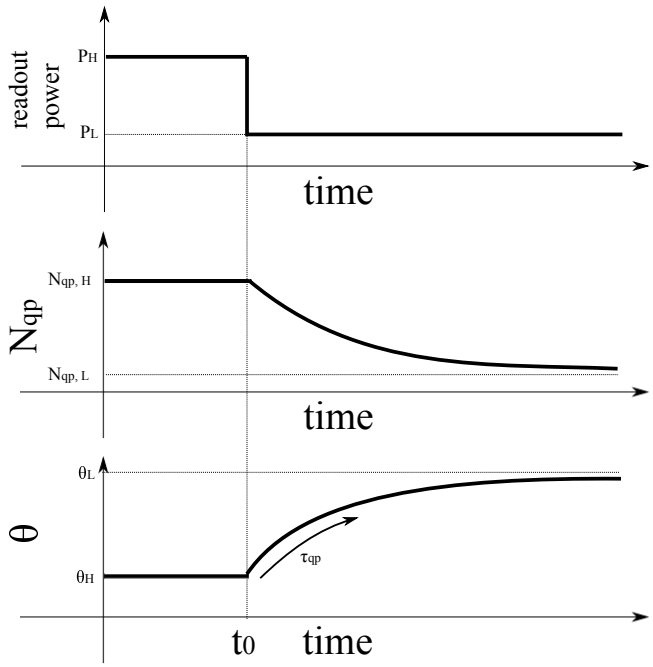

FIGURE 4.1: The illustration of the number of quasiparticles and the phase response of MKID under rapidly power change from high power (P_{H}) to low power (P_{L}) at $t = t_0$. The number of quasiparticles is decreased with quasiparticle lifetime as illustrated in middle figure. This change causes change of phase response with quasiparticle lifetime as described in the bottom figure. We can measure the phase response as a function of time as illustrated in the bottom figure [75].

The applied readout microwave signals power is adjusted by the variable attenuator (LDA-602E, Vaunix Co. Ltd.). We use five initial attenuation set up to stable attenuation value from high power to low power P_{H} to P_{L}: -11.0 dB $\rightarrow$ -17.5 dB, -12.0 dB $\rightarrow$ -17.5 dB, -13.0 dB $\rightarrow$ -17.5 dB, -14.0 dB $\rightarrow$ -17.5 dB and -15.0 dB $\rightarrow$ -17.5 dB. The applied power at the point of MKID feedline is approximately -70 dBm in the case of P_{L}.

4.4 Results

The measured phase response ($\theta_{\mathrm{measured}}$) has the MKID signal ($\theta_{\mathrm{MKID}}$) and phase offset due to the system (θ_{system}) e.g., a cable delay,

$$\theta_{\mathrm{measured}} = \theta_{\mathrm{MKID}} + \theta_{\mathrm{system}}. \tag{4.8}$$

θ_{system} is changed before and after readout microwave signal power change. We measured this effect by the complex transmission S_{21} as a function of microwave frequency at P_{H} and P_{L}, respectivily. We subtract them in the analysis. We estimate the systematic uncertainty as 0.3 rad. After that, we correct non linear response due to deviation from resonance frequency using the following formula [43, 104],

$$\theta = 2\tan(\theta_{\mathrm{MKID}}/2). \tag{4.9}$$

Figure 4.3 shows measured phase response as a function of time. We reset the attenuation value at $t = 100$ μs with a precision of 1 μs. The phase response is

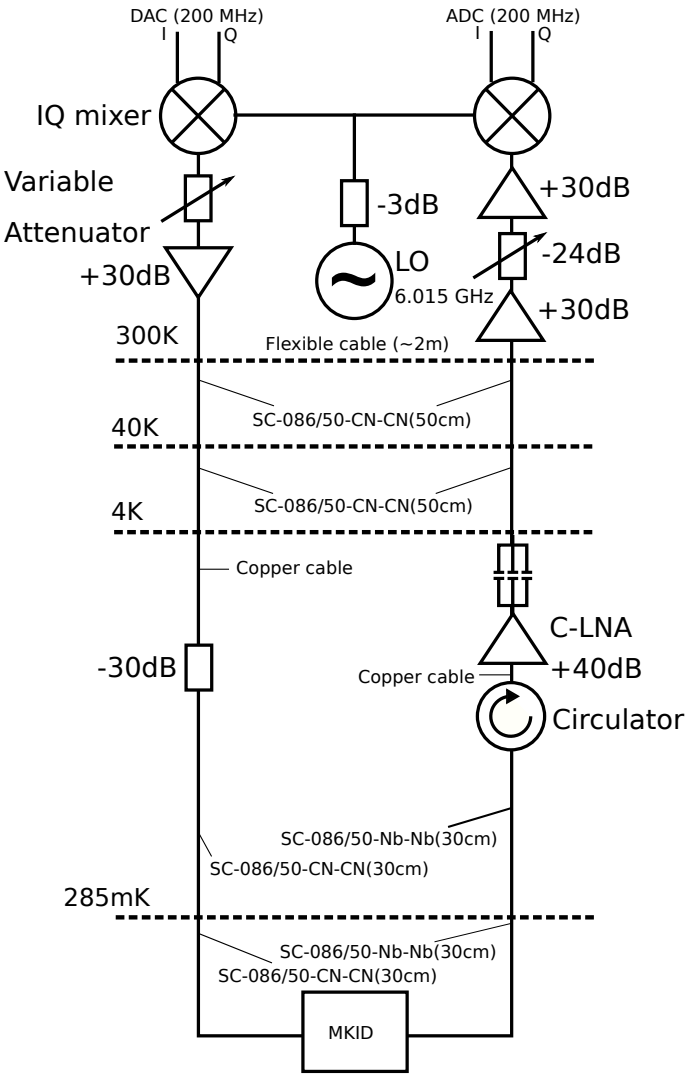

FIGURE 4.2: A diagram of the MKID readout system. Our readout system generate feed signal at a 200 MHz bandwidth, which is up-converted in the microwave range. The local oscillator (LO) is the NI Microwave Components FSL-0010, and the details of the mixer is described in Ref. [101]. We uses a varialble attenuator as described in the text to control the fedding microwave power into MKID. Output microwaves from the MKID is amplified by the low noise amplifier (LNF-LNC4_8C) and warm amplifiers (ZVE-8G+, Mini-Circuits). After down-conversion of microwaves, we sampled them at 200 MHz [75].

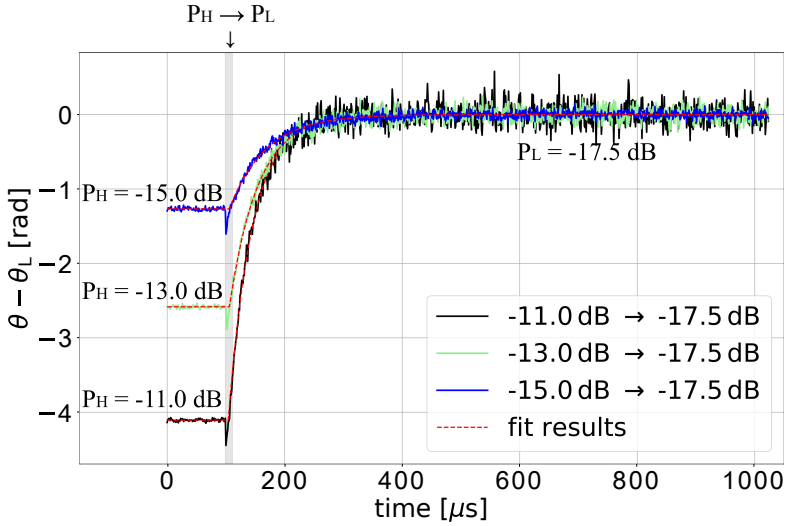

FIGURE 4.3: Phase response as a function of time when the readout microwave signal change at $t = 100\ \mu$s. It takes several microseconds to change the power. Therefore, we mask the region from $t = 100\ \mu$s to 110 μs. The dashed line represents fitting results [75].

TABLE 4.1: Measurement results for each readout power setup. Errors are included statistical and systematic errors. In our measurement, the statistical errors are smaller than systematic errors[75].

$P_H \to P_L$	$\theta_L - \theta_H$ [rad]	τ_{qp} [μs]	$N_{qp}/10^6$
$-11.0 \to -17.5$	4.17 ± 0.31	41.6 ± 1.0	2.94 ± 0.07
$-12.0 \to -17.5$	3.37 ± 0.30	43.4 ± 1.0	2.82 ± 0.06
$-13.0 \to -17.5$	2.60 ± 0.30	48.1 ± 1.0	2.54 ± 0.05
$-14.0 \to -17.5$	2.00 ± 0.30	54.9 ± 1.0	2.22 ± 0.04
$-15.0 \to -17.5$	1.26 ± 0.30	60.7 ± 1.0	2.02 ± 0.03

changed with time constant after rapidly readout power change. We fit the data by Eq. (4.6) and obtain phase response of MKID and quasiparticle lifetime. We mask the region, $t = 100\ \mu$s $- 110\ \mu$s, due to the uncontrolled state of attenuation after the reset as mentioned above. We repeat this measurement 40 times for each attenuation setup. The results are summarized in Table 4.1. Figure 4.4 shows the relation between the measured phase response as a function of N_{qp} based on Table 4.1. We obtain $d\theta/dN_{qp} = (2.8 \pm 0.3) \times 10^{-6}$ rad from fitting the linear relation. For comparison, we also measure the responsivity of same device by the conventional methods: the heater control method and PSD method as mentioned above. From the heater control method, we change the stage temperature from 285 mK to 300 mK and obtain resonance frequency. From this measurement, we can obtain $d\theta/dN_{qp} = (9.9 \pm 0.3) \times 10^{-7}$ rad, here we only take into account for the statistical error. Using PSD method, we obtain $d\theta/dN_{qp} = (2.4 \pm 0.2) \times 10^{-6}$ rad.

The results have a little difference. We estimate that the difference between these three method is from the difference between the temperature measured by the thermometer and the detector temperature. Another problem is that the parameters by the PSD method are biased by the $1/f$ type noise due to TLS noise. Also, the uncertainty of the superconducting transition temperature T_c causes the difference,

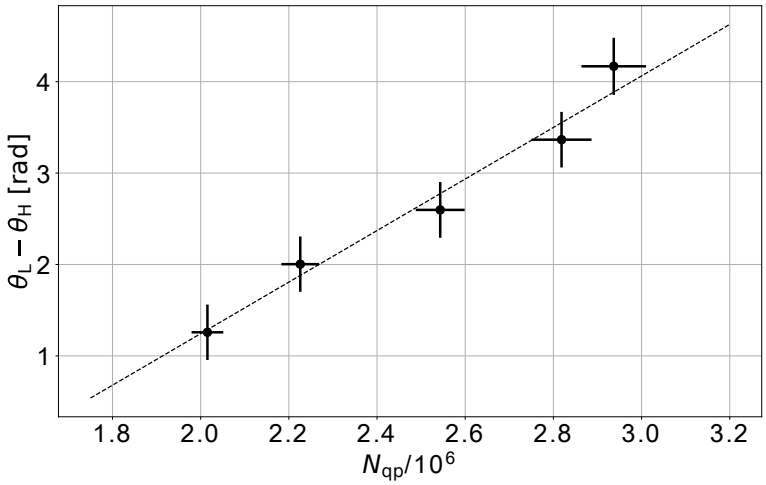

FIGURE 4.4: The relation between the phase response ($\theta_L - \theta_H$) and the number of qussiparticles (N_{qp}) in Table 4.1. We obtain the responsivity from the linear fit [75].

because our proposed method and PSD method is lineally scaled by T_c, on the other hand the heater control method is exponentially scaled by T_c.

4.5 Conclusion and Discussion

We propose the method to measure the responsivity of an MKID device by changing the power of the readout microwave signal. We propose new calibration method based on the excess quasiparticles depending on the readout microwave signal power. The number of quasiparticles is obtained by the measured lifetimes, geometrical parameter, and physical properties parameters with theoretical formula. We apply this method for the real system and demonstrate the advantage of this method. We compare the result and the results using conventional methods: heater control method and PSD method. The results have a little difference. We estimate that the difference between these three method is from the difference between the temperature measured by the thermometer and the detector temperature. Another problem is that the parameters by the PSD method are biased by the 1/f type noise due to TLS noise. The uncertainty of the T_c also causes the difference. To solve the uncertainty of T_c, we propose new T_c measurement method in the next Chapter. The conventional responsivity calibration method is biased by the difference between the temperature taken by the thermometer and device temperature. The proposed method does not depend on the temperature.

We evaluate the advantage of using the proposed method for the GroundBIRD observation. Since GroundBIRD can not observe during the cooling cycle or when the sun is in its field of view, we estimate the time of the observation and responsivity calibration per day is about twelve hours. The heater control method takes about two hours. If we use the calibration method at the beginning and end of the observation everyday, the observation time per day is limited to about eight hours. If we use the proposed responsivity calibration, since the proposed method is almost no limit to the observation time, the observation time per day is about twelve hours.

Since the resonance frequency is easy to be changed by the condition of the sky radiation, we calibrate the resonance frequency of each MKID every hour using the fitting the complex transmission as a function of readout frequency. Our proposed method also can be used after every resonance frequency calibration. The advantage of the responsivity calibration after the resonance frequency calibration is to achieve more precise observation *.

*This chapter is based upon H. Kutsuma, M. Hattori, R. Koyano, S. Mima, S. Oguri, C. Otani, T. Taino, and O. Tajima, *Applied Physics Letters* **115**, 032603 (2019).

Chapter 5

Novel method to measure superconducting transition temperature of MKID by changing power of readout microwaves

The superconducting transition temperature (T_c) of the MKID is an important parameter for both design and performance evaluation, because various parameters has dependent on the temperature. However, hybrid type MKID, which is adopted for the GroundBIRD observation, is not able to measure this temperature directly, because the material of the feedline and that of the absorb part are not same. In this chapter we propose a new method to measure the T_c of MKID by rapidly changing the applied readout microwave signal. A small fraction of the readout power signal is deposited in the MKID, and the number of quasiparticles in the MKID increases with this applied power. Furthermore, the quasiparticle lifetime decreases with the number of quasiparticles. Therefore, we can measure the realation between the quasiparticle lifetime and the detector phase response by rapidly changing the readout power signal. From this relation, we estimate the intrinsic quasiparticle lifetime. This lifetime is theoretically modeled by T_c, the physical temperature of the device, and other known parameters. We obtain T_c by comparing the measured lifetime with theoretical model. Using an MKID fabricated with aluminium, we demonstrate this method at a 0.3 K operation. The results are consistent with those obtained by T_c measured by monitoring the transmittance of the readout microwave signal with the variation in the device temperature. The method proposed in this chapter is applicable to other types, such as a hybrid type MKID.

5.1 Superconducting transition temperature (T_c)

The superconducting transition temperature (T_c) of the MKID is an important parameter. This is because various MKID parameters depend on T_c. Applying MKID for astronomical observation, the 10% deference of the T_c dramatically change the NEP. In this chapter, we propose new method to measure the T_c of the MKID by changing the readout power signal rapidly [65].

According to the BCS theory [59], the relation between the gap energy (Δ), and T_c is given by the following formula:

$$\Delta = 1.76 k_{\mathrm{B}} T_c, \tag{5.1}$$

where k_B is the Boltzmann constant. A coefficient in the relation is confirmed 1% accuracy for an aluminum [105]. Using Δ, the number of quasiparticles (N_{qp}) under the low temperature condition (i.e. $T \ll T_c$) [59] is obtained by the following formula:

$$N_{qp} = 2N_0 V\sqrt{2\pi k_B T\Delta}\exp\left(-\frac{\Delta}{k_B T}\right), \tag{5.2}$$

where N_0 is the single spin density of states at Fermi level ($N_0 = 1.74\times10^{10}\,\mathrm{eV}^{-1}\mu\mathrm{m}^{-3}$ for an aluminium [76, 77]), and V is the volume of the resonator. The intrinsic quasiparticle lifetime (τ^i_{qp}) is obtained by the following formula [79, 80]:

$$\tau^i_{qp} = \frac{\tau_0}{\sqrt{\pi}}\left(\frac{k_B T_c}{2\Delta}\right)^{5/2}\sqrt{\frac{T_c}{T}}\exp\left(\frac{\Delta}{k_B T}\right), \tag{5.3}$$

where τ_0 is the electron-phonon interaction time ($\tau_0 = 458 \pm 10$ ns for an aluminium MKID [80]). The noise equivalent power derived from the generation and recombination of the quasiparticles (NEP_{gr}) is obtained by the following formula [95]:

$$NEP_{gr} = \frac{2\Delta}{\eta_{pb}}\sqrt{\frac{N_{qp}}{\tau^i_{qp}}}, \tag{5.4}$$

where η_{pb} is the pair breaking efficiency ($\eta_{pb} = 0.57$ for an aluminium [61, 60]). Figure 5.1 shows the parameters of an aluminum MKID as a function of T_c, where we show the plots of the device temperature at approximately 0.3 K. They are sensitive to T_c. Various previous studies have used different T_c, with the deviation being approximately 10% [80, 106, 107]. The reason of the difference is pointed out by a recent research topic, e.g. Fyhire *et al.* [106]. They pointed out the T_c is strongly depend on the film thickness.

5.2 Superconducting transition temperature measurement for MKID

Monitoring the transmittance of the readout microwave signal with the device temperature variation is a conventional method to measure the T_c of an MKID [78, 108]. This method is called as the "S21 method" in this thesis. However, this method is not applicable for a hybrid type MKID because the feedline material of the hybrid type MKID [46, 42] is not same as the response part of the MKID.

Another method evaluates T_c using the power spectrum density (S_x), which is modeled by the following formula [71]:

$$S_x = \frac{4N_{qp}\tau_{qp}}{(1+(2\pi f\tau_{qp})^2)(1+(2\pi f\tau_{res})^2)}\left(\frac{\mathrm{d}x}{\mathrm{d}N_{qp}}\right)^2 + X_{system}, \tag{5.5}$$

where subscript x denotes the phase (θ) or amplitude (A) response, τ_{qp} is the quasiparticle lifetime for the measurement condition, f is the sampling frequency, and X_{system} is the noise of the readout system featured by the low noise amplifier inside of the cryostat. τ_{res} is the resonator ring time given by $\tau_{res} = Q_r/\pi f_r$ (where Q_r is the quality factor of the resonance and f_r is the resonant frequency). We extract τ_{qp} by fitting the power spectrum density with the above formula. Under the assumption of $\tau^i_{qp} = \tau_{qp}$, we obtain T_c using Eq. (5.3). This method requires that X_{system} is lower than the contribution of the generation and recombination noise which is the first

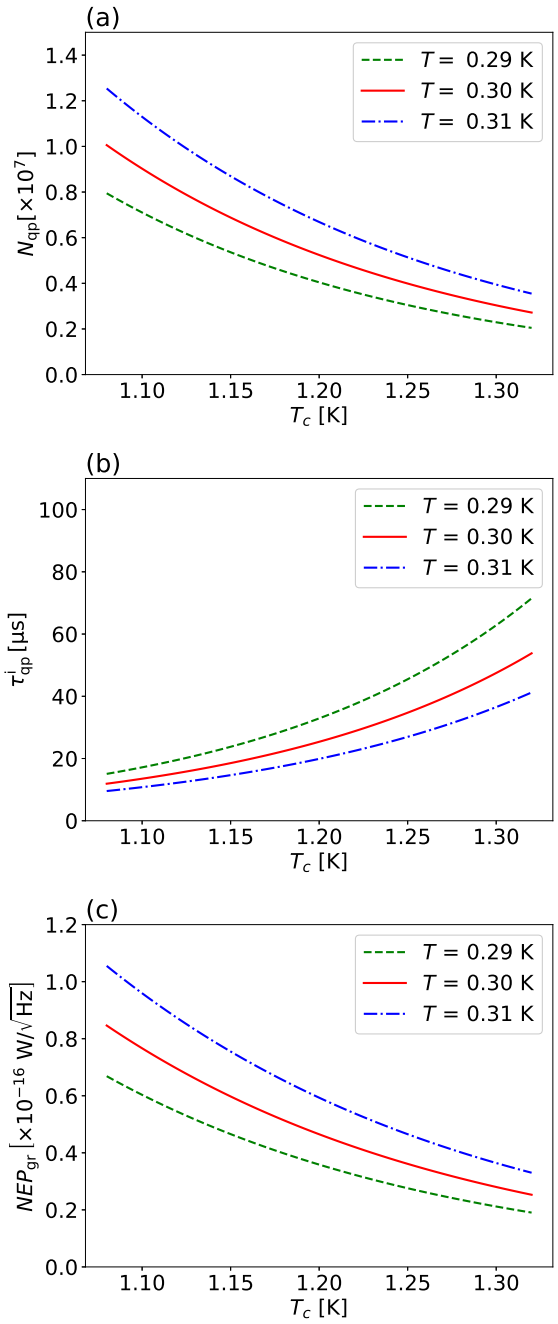

FIGURE 5.1: Parameters characterizing an MKID as a function of the superconducting transition temperature, (a) the number of quasiparticles, (b) intrinsic quasiparticle lifetime, and (c) noise equivalent power. They are simulated in the case of an aluminum MKID with volume 1000 μm^3 [65].

term in Eq. (5.5). Moreover, another contribution due to a TLS noise should be low enough in the case of the phase response [88, 43, 89].

5.3 New method for obtaining T_c

We propose the third method to measure T_c, which uses a loss of the readout microwave signal in the MKID. The quasiparticle lifetime (τ_{qp}) decreases with the increase of the number of additional quasiparticles (N'_{qp}) produced by the readout power signal loss [71, 72, 73, 74, 57, 75, 65]:

$$\tau_{qp} = \frac{\tau^i_{qp}}{1 + \frac{N'_{qp}}{N_{qp}}}. \tag{5.6}$$

Since the phase response (θ) of the MKID is proportional to the number of additional quasiparticles [70], the above formula is rewritten by:

$$\tau_{qp} = \frac{\tau^i_{qp}}{1 + \alpha\theta}, \tag{5.7}$$

where $\alpha\theta = N'_{qp}/N_{qp}$. This relation suggests that τ^i_{qp} can be estimated from the relation between τ_{qp} and θ [57, 70]. This relation is easily measured using our previous method to measure the phase responsivity shown in previous chapter and Ref. [75]. A small fraction of the readout power signal is deposited in the MKID, and the response of the MKID increases with this power.

5.4 The measurement setup

We demonstrate the measurement of this relation for an aluminum MKID. Subsequently, we obtain T_c with Eq. (5.3) and estimate τ^i_{qp}. Figure 5.2 shows the diagram of the MKID readout. Our cryostat (Niki Glass Co., LTD,) consists of 4 K, and 40 K thermal shields from inside to outside. They are insulated from the room temperature (300 K) in a vacuum chamber and are cooled by a pulse tube refrigerator (PT407RM, Cryomech Co., LTD.). The 4 K thermal shield also acts as a magnetic shield (A4K, Amuneal Co., LTD.) for mitigating the effects of geomagnetism. The MKID device is set in a light-tight copper box. The box is cooled a ^{3}He-sorption refrigerator, and it is maintained at $T = 311$ mK with an accuracy of 6 mK.

The MKID device is fabricated in RIKEN. This device consists of a quarterwave resonator without any antenna. The width of the center strip and gap of the resonator (the feedline) are 4 μm (12 μm) and 1.5 μm (8 μm), respectively. All the circuits patterns are formed using an aluminum film on a silicon wafer. The volume of the resonator is $2,600$ μm^3 (the width is 4 μm, the length is $6,500$ μm, and the thickness is 100 nm). Its resonant frequency and quality factor are $f_r = 4.30$ GHz and $Q_r = 2.61 \times 10^4$, respectively. Our readout system measures the response based on a direct down-conversion logic with a 200 MHz sampling speed, and the data are down-sampled to a 1 MHz step [98, 99, 100]. The power of the readout microwave is controlled by a variable attenuator (LDA-602, Vaunix Co., LTD). It requires a few microseconds to change the attenuation value.

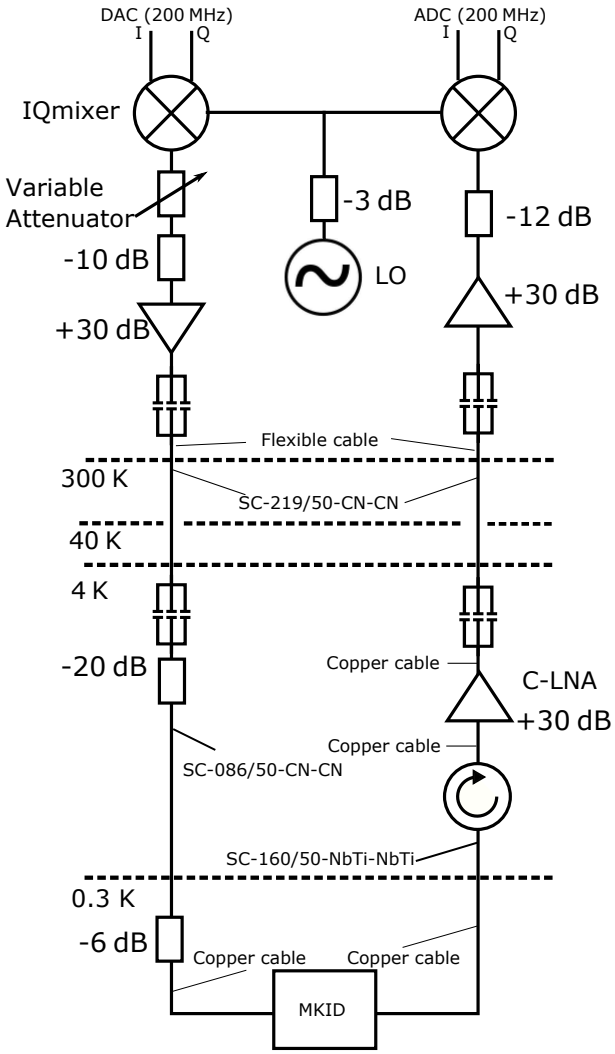

FIGURE 5.2: Diagram of the readout chain of the MKID. Our system feeds the readout signal at 200 MHz bandwidth, which is upconverted into the microwave range. We use an NI Microwave Components FSL-0010 as a local oscillator (LO). The mixer is a Marki Microwave MLIQ-0218L. The input power into MKID is controlled by a variable attenuator. The output microwave from the MKID are amplified by a low noise amplifier (C-LNA, LNF-LN4_8, LOWNOISE FACTORY) and a warm amplifier (ZVE-8G+, Mini-Circuits). Subsequenmtly, the down-converted signal is sampled [65].

TABLE 5.1: Measured results for each setup of the readout power signal change. Only statistical errors are assigned here [65].

$P_H \rightarrow P_L$	θ [rad]	τ_{qp} [μs]
$-15.5 \rightarrow -22.0$	1.374 ± 0.007	25.5 ± 0.2
$-16.0 \rightarrow -22.0$	0.972 ± 0.004	26.6 ± 0.1
$-16.5 \rightarrow -22.0$	0.894 ± 0.002	26.7 ± 0.1
$-17.0 \rightarrow -22.0$	0.805 ± 0.003	27.1 ± 0.1
$-17.5 \rightarrow -22.0$	0.728 ± 0.004	27.6 ± 0.1
$-18.0 \rightarrow -22.0$	0.538 ± 0.004	28.4 ± 0.1
$-18.5 \rightarrow -22.0$	0.462 ± 0.005	28.9 ± 0.2
$-19.0 \rightarrow -22.0$	0.391 ± 0.004	29.4 ± 0.2

5.5 Results

We use eight attenuation setups to change the readout power signal from high power (P_H) to low power (P_L) summarised in Table 5.1. The readout power signal into the feedline is approximately -65 dBm at P_L. We use the same treatment for the effects of a cable delay and linearity correction as described in the previous chapter and Ref. [75]. Figure 5.3 shows the phase response as a function of time. We reset the attenuation value at $t = 100$ μs. We fit the data to Eq. 4.4, and obtain the phase response (θ) and the quasiparticle lifetime (τ_{qp}) for each setup using Eq. 5.7. We mask the data in the short period, $t = 95 - 105$ μs, because of the uncontrolled state of attenuation soon after the reset. We measure 50 samples for each set of power change. Table 5.1 summarizes the fitted results for each setup. Figure 5.4 shows the relation between τ_{qp} and θ. We obtain $\tau^i_{qp} = 31.3 \pm 0.2$ μs from the fit with Eq. 5.7. Subsequently, we obtain $T_c = 1.278 \pm 0.001$ K using Eq. (5.3), where we only estimate the statistical error. We include the systematic uncertainties for T_c; device temperature (0.025 K), time for changing the attenuation value (0.014 K), and electron-phonon interaction time (0.004 K). We finally obtain $T_c = 1.28 \pm 0.03$ K , including the systematic error.

For comparison, we also measure T_c by the S21 method. Figure 5.5 presents the S21 intensity results at 4.35 GHz as a function of the device temperature. We determine T_c as a temperature at the middle of the transition, $T_c = 1.27 \pm 0.04$ K. Here, the error includes the difference from the onset of the superconducting transition and the uncertainty of the thermometer. We confirm the consistency in the results from the two methods.

5.6 Summary

We propose the method to measure the T_c of an MKID device by changing the power of the readout microwave signal. In this method, we obtain the intrinsic quasiparticle lifetime using the device temperature and the material properties parameters. Subsequently, we estimate T_c using them. We demonstrate our method using an aluminum MKID maintained at 311 mK. We obtain $T_c = 1.28 \pm 0.03$ K. This result is consistent with the conventional method: monitoring the microwave transmittance by changing the device temperature, $T_c = 1.27 \pm 0.04$ K. The method has an ability to apply other types, such as a hybrid type MKID.

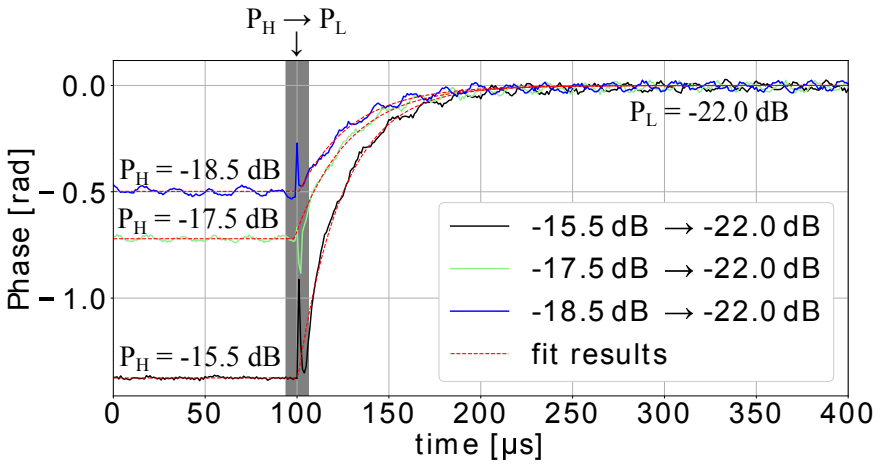

FIGURE 5.3: Phase response to the rapid change in the power of the readout signal. The change is introduced at $t = 100$ μs with a few μs uncertainty. Therefore, we mask the region at $t = 95 - 105$ μs in the fitting. The dashed line s are fitting results [65].

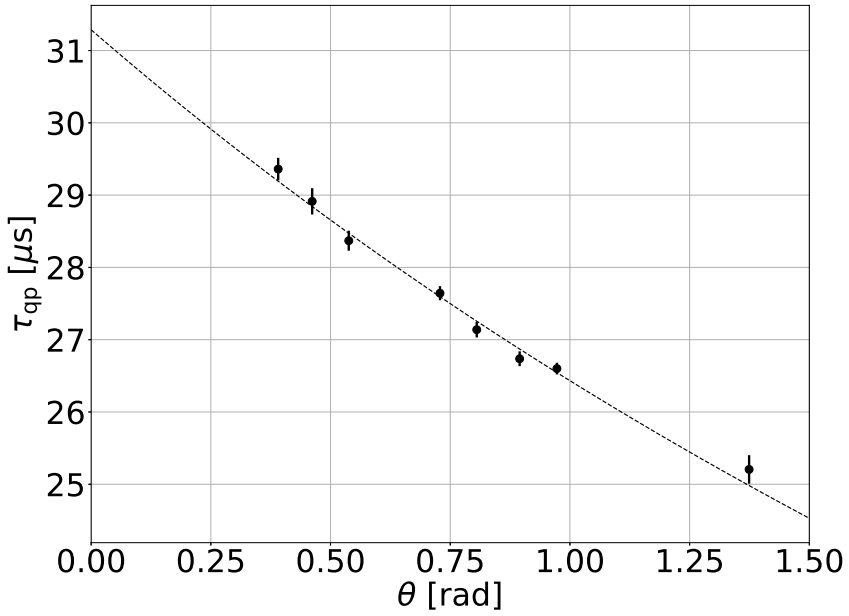

FIGURE 5.4: Measured relation between the quasiparticle lifetime (τ_{qp}) and the phase response (θ). The black dots shows the measurement results. The dashed line represents the fit result. The value at $\theta = 0$ corresponds to the intrisic quasiparticle lifetime [65].

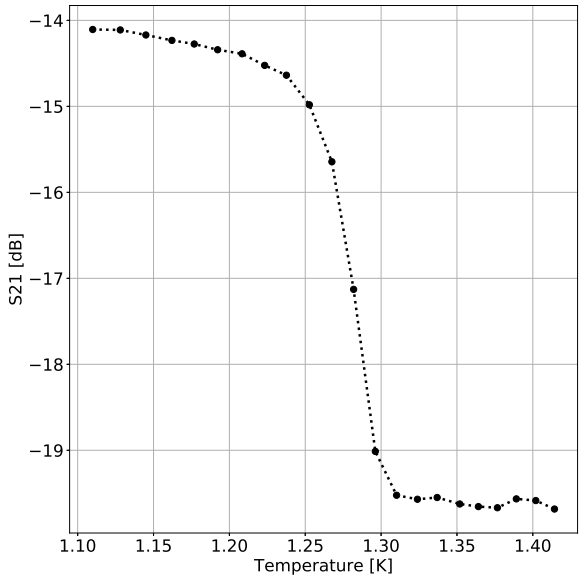

FIGURE 5.5: Transmittance of the readout microwave signal as a function of the MKID temperature [65].

We evaluate the systematic uncertainty of the T_c for various observations. The typical T_c for an aluminum MKID is 1.1 $\sim$ 1.5 K [80, 107, 109, 110]. The uncertainty of the superconducting transition temperature causes the systematic error of the observational predictions. The noise equivalent power of the MKID for the optical bright condition is given by

$$NEP = \sqrt{\frac{2h\nu P_{\rm rad}(1+\eta_{\rm opt}\eta_{\rm em}\bar{n}) + 4\Delta P_{\rm rad}/\eta_{\rm pb}}{\eta_{\rm opt}}}, \tag{5.8}$$

where $P_{\rm rad}$ is the radiation power, $\eta_{\rm opt}$ is the optical efficiency, $\eta_{\rm em}$ is the emissivity of the source or the atmosphere, $\bar{n}$ is the photon occupation number given by $\bar{n} = 1/\exp(h\nu/k_{\rm B}T_{\rm amb} - 1)$ ($T_{\rm amb}$ is the ambient temperature), and $\eta_{\rm pb}$ is the pair braking efficiency ($\eta_{\rm pb} = 0.57$ for an aluminium [61, 60]). We estimate the systematic effect of T_c for the NEP of atmospheric observation by the GroundBIRD telescope as shown in Chapter 1. When T_c of an aluminum is 1.1 K (1.5 K), the estimated NEP of 145 GHz and 220 GHz band sky observation by the GroundBIRD are 9.7 $\times 10^{-17}$ W/$\sqrt{\rm Hz}$ (1.0 $\times 10^{-16}$ W/$\sqrt{\rm Hz}$) and 1.9 $\times 10^{-16}$ W/$\sqrt{\rm Hz}$ (2.0 $\times 10^{-16}$ W/$\sqrt{\rm Hz}$), respectively. As a results, the uncertainty of the typical T_c value causes about 20% NEP deference for the atmospheric observations by the GroundBIRD telescope. We can have an optical efficiency for comparing measured NEP and theoretical NEP given by Eq. (5.8), because the difference is caused by the optical efficiency. However if we do not know the exact value of T_c, the 20% uncertainty of the calibration of the optical efficiency is caused due to the uncertainty of T_c.

Assuming that MKID is used in the space CMB satellite mission, the background loading is CMB itself. In this case, when the center frequency is 145 GHz and the frequency band width is 20 GHz, the NEP at $T_c = 1.1$ K and at $T_c = 1.5$ K are 2.0×10^{-17} W/$\sqrt{\rm Hz}$ and 2.2×10^{-17} W/$\sqrt{\rm Hz}$, respectively. As a results, the uncertainty of the typical T_c value causes about 10% NEP deference. If MKID is used in a near dark condition, e.g. the dark matter search experiment, the NEP of MKID is given

by Eq. (5.4). In this case, when the detector temperature is 250 mK and the resonator volume is 1000 μm^3, the NEP at $T_c = 1.1$ K and at $T_c = 1.5$ K are 1.9×10^{-17} W$/\sqrt{\text{Hz}}$ and 1.5×10^{-18} W$/\sqrt{\text{Hz}}$, respectively. About tenfold NEP difference is caused. To measure T_c of the MKID is the important to evaluate the performance of MKID*.

*This chapter is based upon H. Kutsuma, Y. Sueno, M. Hattori, S. Mima, S. Oguri, C. Otani, J. Suzuki, and O. Tajima, *AIP Advances* **10**, 095320 (2020).

Chapter 6

Development of the performance forecaster of MKID

As show in Chapter 3, the performance of the prototype MKID mounted on the GroundBIRD telescope is too low to extract required performance of the GroundBIRD. The NEP has a high 1/f type noise. It is higher than the G-R noise. Further optimization of fundamental design of MKID is required. The one cycle from design to the evaluation for the MKID needs a lot of time. We have to iterate this cycle several times to feed back the results to new design. Dramatic reduction of the time consumption for this research and development cycle is desired. For this purpose, we develop the forecaster which evaluate the MKID performance quantitatively by setting environmental variables and design parameters. Detail of the design parameters which control the performance of the MKIDs are introduced in the following chapter.

6.1 Modeling for dark condition

The performance of MKID depends on the material specification (low temperature resistivity, superconducting transition temperature, and reference of the two level system noise), geometry, and measurement condition (readout power, device temperature, amplifier thermal noise, and optically bright condition). In this section, we modeled the performance of the hybrid type MKID in the dark condition. The hybrid type MKID [46, 42] which consists of two superconducting materials is widely used for the recent astronomical observation. The sensitive part on the antenna side shown in Figure 2.5 is consist of material with low superconducting transition temperature, e.g., aluminum. The non-sensitive part on the feedline side shown in Figure 2.5 is consist of materiel with high superconducting transition temperature, e.g., niobium. In this thesis, the sensitive part and non-sensitive part are called "absorb part" and "transmission part", respectively.

6.1.1 Modeling of the hybrid type MKID

We extend the MKID theory described in Chapter 2 to the hybrid type MKID and calculate the parameters of the prototype MKID as shown in Chapter 3. The geometry and material specification of the prototype MKID are summarized in Table 6.1. The resonator is quarterwave resonator and the substrate is silicon. The relative permittivity of the silicon is set to $\epsilon_{\mathrm{sub}} = 11.49$ [110] in the forecaster.

The performance of the MKID depends on the kinetic inductance fraction α_k which is the ratio of the kinetic inductance of the center strip of the absorb part $L_{k,c}$ to the total inductance L_{tot}. The total inductance L_{tot} is summation of the kinetic inductance L_{k} and the geometrical inductance L_g. The kinetic inductance L_k is due

	Aluminum	Niobium	reference
T_c	1.28 K	9.2 K	[65, 85]
ρ_N	1.5 $\mu\Omega \cdot$ cm	5 $\mu\Omega \cdot$ cm	[110, 85]
l	2300 μm	2700 μm	/
s	4 μm	3 μm	/
w	1.5 μm	4 μm	/
d	0.1 μm	0.2 μm	/
d_g	/	0.2 μm	/

TABLE 6.1: The geometry and material property of the prototype MKID design. The absorb and transmission material are aluminum and niobium, respectively. T_c is the superconducting transition temperature. ρ_N is the low temperature resistivity (resistivity just before the superconducting transition). l is the length of the absorb part. s is the center strip width. w is the slot width between the center strip and groundplane. d and d_g are the thickness of the center strip and groundplane, respectively.

to the motion of the Cooper pair. The geometrical inductance L_g is defined by the geometry. The kinetic inductance per unit length [84] of the absorb part $L_{k,\mathrm{abs}}$ is given by

$$L_{k,\mathrm{abs}} = g_c L_{s,\mathrm{abs}} + g_g L_{s,\mathrm{ground}} = L_{k,c} + L_{k,\mathrm{ground}}, \tag{6.1}$$

where $L_{s,\mathrm{abs}}$ is the surface inductance of the center strip of the absorb part and $L_{s,\mathrm{ground}}$ is the surface inductance of the groundplane. In general, the material of the center strip of the transmission part and that of the groundplane and the readout feedline are same. The kinetic inductance [84] per unit length of the transmission part is given by

$$L_{k,\mathrm{trans}} = (g_c + g_g) L_{\mathrm{s,trans}}, \tag{6.2}$$

where $L_{s,\mathrm{trans}}$ is the surface inductance of the transmission part and g_c and g_g are the geometry factor for the center strip and the groundplane, respectively. The surface inductance L_s [83] is given by

$$L_{\mathrm{s}} = \mu_0 \lambda_{\mathrm{dirty}} \coth(d/\lambda_{\mathrm{dirty}}), \tag{6.3}$$

where μ_0 is the permeability of the free space and λ_{dirty} is the penetration depth for the dirty limit at $T = 0$ K [57] given by

$$\lambda_{\mathrm{dirty}} \sim 105\ \mathrm{nm} \times \sqrt{\frac{\rho_N}{[\mu\Omega \cdot \mathrm{cm}]} \frac{[\mathrm{K}]}{T_c}}, \tag{6.4}$$

where ρ_N is the low temperature resistivity (resistivity just before the superconducting transition) and T_c is the superconducting transition temperature. The geometry factor g_c for the center strip and for the groundplane g_g [84] are characterized the current density distribution for the CPW line are given by

$$g_c = \frac{1}{4s(1-k^2)K^2(k)} \left[\pi + \ln\left(\frac{4\pi s}{d_c}\right) - k \ln\left(\frac{1+k}{1-k}\right) \right], \tag{6.5}$$

and

$$g_g = \frac{k}{4s(1-k^2)K^2(k)} \left[\pi + \ln\left(\frac{4\pi(s+2w)}{d_g}\right) - \frac{1}{k} \ln\left(\frac{1+k}{1-k}\right) \right], \tag{6.6}$$

	Aluminum	Nibium
λ_{dirty} [nm]	114	77
L_{s} [pH/sq]	0.2	0.1
g_{c} [/m]	0.27	0.29
g_{g} [/m]	0.12	0.07
L_{k} [μH/m]	0.06	0.04
L_{g} [μH/m]	0.37	0.53
L_{tot} [μH/m]	0.44	0.57

TABLE 6.2: The penetration depth, the inductance, and the geometry factor of the prototype MKID. λ_{dirty} is the penetration depth, L_{s} is the surface inductance, g_c and g_g is the geometry factor for the center strip and the groundplane, respectively, L_{k} is the kinetic inductance, L_{g} is the geometrical inductance, and L_{tot} is the total inductance.

where s is the center strip width, $k = s/(s+w)$ (w is the slot width of the CPW line), K is the complete elliptic integral of the first kind, d_{c} is the thickness of the center strip, and d_g is the thickness of the groundplane. The geometrical inductance per unit length L_g is described by the CPW geometry

$$L_g = \frac{\mu_0}{4}\frac{K(k')}{K(k)}, \tag{6.7}$$

where $k' = \sqrt{1-k^2}$. The total inductance L_{tot} is given by

$$L_{\mathrm{tot}} = L_k + L_g. \tag{6.8}$$

Since the transmission part has high T_c, the response of the transmission part is negligible. Therefore, the kinetic inductance fraction α_k of the hybrid type MKID is given by

$$\alpha_k = \frac{L_{\mathrm{k,c}} l_{\mathrm{abs}}}{L_{\mathrm{tot,abs}} l_{\mathrm{abs}} + L_{\mathrm{tot,trans}} l_{\mathrm{trans}}}, \tag{6.9}$$

where l_{abs} and l_{trans} are the length of the absorb part and the transmission part, respectively, $L_{\mathrm{tot,abs}}$ and $L_{\mathrm{tot,trans}}$ are the total inductance per unit length of the absorb part and the transmission part, respectively. The kinetic inductance fraction depends on the length of the absorb part. The penetration depth, the inductance, and the geometry factor of the prototype MKID design are summarized in Table 6.2.

By giving the kinetic inductance fraction and the geometry, we can calculate the resonance frequency and quality factors. The resonance frequency at $T = 0$ K, f_{r0}, is described by the resonator length and total kinetic inductance fraction as follows

$$f_{r0} = \frac{c}{4l}\sqrt{\frac{1-\alpha_{k,\mathrm{tot}}}{\epsilon_{\mathrm{eff}}}}, \tag{6.10}$$

where c is the speed of light, l is the total length of the resonator, and ϵ_{eff} is the effective dielectric constant given by $\epsilon_{\mathrm{eff}} = (1+\epsilon_{\mathrm{sub}})/2$. The total kinetic inductance fraction $\alpha_{k,\mathrm{tot}}$ is given by

$$\alpha_{k,\mathrm{tot}} = \frac{L_{\mathrm{k,abs}} l_{\mathrm{abs}} + L_{k,\mathrm{trans}} l_{\mathrm{trans}}}{L_{\mathrm{tot,abs}} l_{\mathrm{abs}} + L_{\mathrm{tot,trans}} l_{\mathrm{trans}}}. \tag{6.11}$$

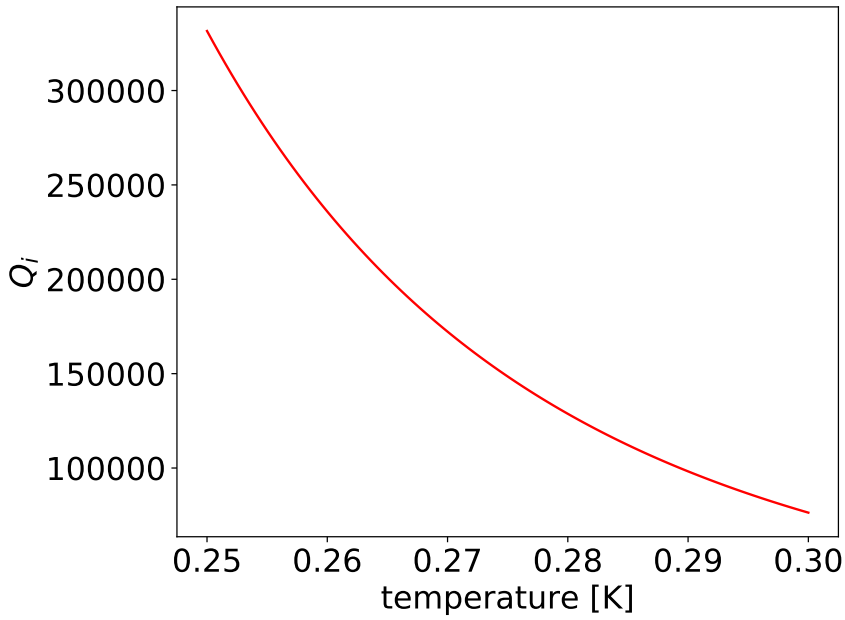

FIGURE 6.1: The relation between the internal quality factor and the device temperature of the prototype MKID design.

The frequency responsivity $\delta f_r / f_r$ is described by the kinetic inductance fraction and the complex conductivity given by

$$\frac{\delta f_r}{f_{r0}} = \frac{\alpha_k \beta_\lambda}{4} \frac{\delta \sigma_2}{\sigma_2}, \tag{6.12}$$

where σ_2 is the complex conductivity of the imaginary part given by Eq. (2.6), and $\delta\sigma_2$ is the responseivity of the complex conductivity of the imaginary part given by Eq. (2.8), and β_λ is the correction factor due to the faintness of the thickness and is given by

$$\beta_\lambda = 1 + \frac{2d/\lambda_{\text{dirty}}}{\sinh(2d/\lambda_{\text{dirty}})}. \tag{6.13}$$

The resonance frequency including temperature dependence is given by

$$f_r = \left[1 + \frac{\alpha_k \beta_\lambda}{4} \frac{\delta\sigma_2}{\sigma_2 V} \frac{\delta\sigma_2}{\delta n_{\text{qp}}} N_{\text{qp}}\right] f_{r0}, \tag{6.14}$$

where N_{qp} is the number of quasiparticles. The internal quality factor due to the thermal loading Q_i [85] is given by

$$Q_i = \frac{2}{\alpha_k \beta_\lambda} \frac{\sigma_2}{\sigma_1} \tag{6.15}$$

where σ_1 is the complex conductivity of real part given by Eq. (2.5). The relation between the internal quality factor and device temperature of the prototype MKID is shown in Figure 6.1. The internal quality factor increases with decreasing the device temperature.

The coupling quality factor Q_c is determined by the geometry of the coupling

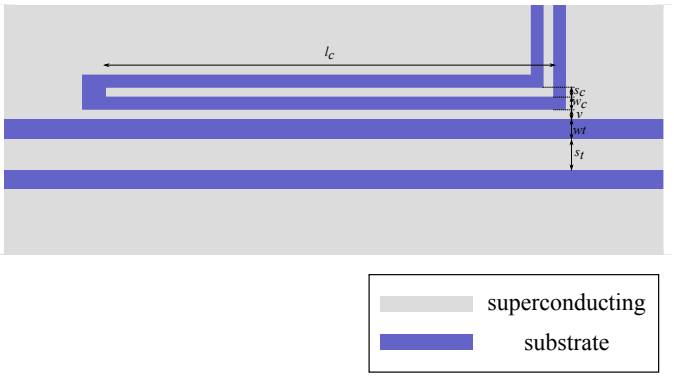

FIGURE 6.2: The coupling geometry.

l_c	140 μm
s_c	3 μm
w_c	4 μm
v	3 μm
s_t	10 μm
w_t	6 μm

TABLE 6.3: The geometry of the coupling of the prototype MKID design. l_c is the coupling length. s_c is the coupling line width. w_c is the coupling slot width. v is the deference between the coupling and the feedline. s_t is the feedline strip width. w_t is the feedline slot width.

with the readout feedline as shown in Figure. 6.2. The Q_c can be calculated applying Schwarz-Christoffel mapping [111]. We calculate Q_c using the public code "cpw_coupling" [111]. The coupling geometry of the prototype MKID design summarized in Table 6.3. The inverse of the resonator quality factor $1/Q_r$ is the summation of the inverse of the internal quality factor and coupling quality factor. The relation between Q_r, Q_c and Q_i is given by

$$\frac{1}{Q_r} = \frac{1}{Q_c} + \frac{1}{Q_i}. \tag{6.16}$$

The complex transmission S_{21} as a function of readout frequency is given by

$$S_{21} = 1 - \frac{Q_r/Q_c}{1 + 2iQ_r\frac{f_{\text{read}} - f_r}{f_r}}, \tag{6.17}$$

where f_{read} is the readout frequency. The amplitude and the phase of the complex transmission S_{21} as a function of readout frequency of the prototype MKID design in various device temperature are shown in Figure 6.3. The resonance frequency and the resonance depth of the absorption line like feature appeared at the resonance frequency decrease with increasing temperature. Here after, we refer the depth of this feature as resonance depth. The complex transmission S_{21} takes minimum value at $f_{\text{read}} = f_r$. Therefore, the resonance depth is given by Q_r/Q_i. To extract the good performance from MKID, the resonance depth must not be too small. To realize the good performance MKID $Q_c \sim Q_i$. When $Q_c \gg Q_i$, the resonance depth becomes very small. In this case, it is hard to identify the resonance feature.

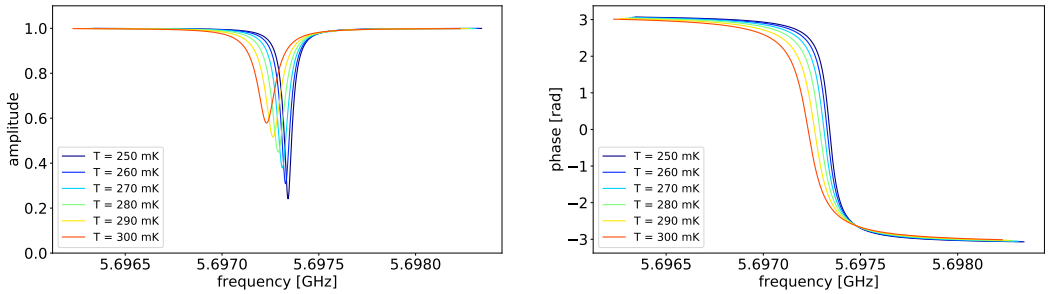

FIGURE 6.3: The amplitude (left figure) and the phase (right figure) of the complex transmission S_{21} as a function of readout frequency in various device temperature of the prototype MKID design.

	model	measurement	model/measurement
f_r [GHz]	5.70	6.07	0.94
Q_r [$\times 10^4$]	5.4	4.9 ± 0.1	1.10
Q_c [$\times 10^4$]	10.5	10.6 ± 0.1	0.99
Q_i [$\times 10^4$]	11.2	8.8 ± 0.2	1.27
$\mathrm{d}A/\mathrm{d}N_{\mathrm{qp}}$ [$\times 10^{-7}$]	4.72	2.82 ± 0.02	1.67
$\mathrm{d}\theta/\mathrm{d}N_{\mathrm{qp}}$ [$\times 10^{-6}$rad]	1.71	1.52 ± 0.04	1.13
τ_{res} [μs]	3.02	2.56 ± 0.04	1.18

TABLE 6.4: The comparison of the model results and the measurement results. The device temperature is 285 mK.

The responsivity of the MKID [78] for amplitude $\mathrm{d}A/\mathrm{d}N_{\mathrm{qp}}$ and for phase $\mathrm{d}\theta/\mathrm{d}N_{\mathrm{qp}}$ are given by

$$\frac{\mathrm{d}A}{\mathrm{d}N_{\mathrm{qp}}} \approx -\frac{\alpha_k \beta_\lambda Q_r}{\sigma_2 V}\frac{\mathrm{d}\sigma_1}{\mathrm{d}n_{\mathrm{qp}}}, \tag{6.18}$$

and

$$\frac{\mathrm{d}\theta}{\mathrm{d}N_{\mathrm{qp}}} \approx -\frac{\alpha_k \beta_\lambda Q_r}{\sigma_2 V}\frac{\mathrm{d}\sigma_2}{\mathrm{d}n_{\mathrm{qp}}}, \tag{6.19}$$

respectrively, where V is the volume of the absorb part, and, $\mathrm{d}\sigma_2/\mathrm{d}n_{\mathrm{qp}}$ and $\mathrm{d}\sigma_2/\mathrm{d}n_{\mathrm{qp}}$ are the relation between the number density of the quasiparticles and the complex conductivity given by Eqs. (2.7) and (2.8). The responsivity is proportional to inverse of the volume of the absorb part. Therefore, the responsivity can be optimized by adjusting the volume of the absorb part.

The resonator ring time τ_{res} which is the time constant described by dumping time scale of the equivalent LCR circuit to MKID, is given by

$$\tau_{\mathrm{res}} = \frac{Q_r}{\pi f_r}. \tag{6.20}$$

In general, the resonator ring time is shorter than the quasiparticle lifetime for an aluminum MKID.

The comparison of the model results and the measurement results as mentioned in Chapter 3 is summarized in Table 6.4. The device temperature is 285 mK. The difference of the model and the measurement is less than 70%. It confirms that our forecaster provides reasonably good evaluation of the MKID performance.

6.1.2 PSD model

We introduce the PSD model based on the previous study [43, 110]. The amplitude PSD S_A is the summation of the generation and recombination noise (G-R noise) and the low noise amplifier noise (LNA noise) given by

$$S_A = S_{A,\mathrm{G-R}} + S_{A,\mathrm{LNA}}. \tag{6.21}$$

The phase PSD S_θ is the summation of the TLS noise (Two level system noise), the G-R noise, and the LNA noise given by

$$S_\theta = S_{\theta,\mathrm{TLS}} + S_{\theta,\mathrm{G-R}} + S_{\theta,\mathrm{LNA}}. \tag{6.22}$$

Note that previous study shows the existence of the amplitude TLS noise. However the effect is much lower than the LNA and the G-R noise [93]. We ignore the effect in our calculation.

G-R noise model

For the dark condition, the noise is limited by the fluctuation of the quasiparticles generation and recombination.

The PSD of the G-R noise $S_{x,\mathrm{G-R}}$ [87, 80] is given by

$$S_{x,\mathrm{G-R}} = \frac{4N_{\mathrm{qp}}\tau_{\mathrm{qp}}}{[1+(2\pi f\tau_{\mathrm{qp}})^2][1+(2\pi f\tau_{\mathrm{res}})^2]}\left(\frac{\mathrm{d}x}{\mathrm{d}N_{\mathrm{qp}}}\right)^2 \quad (x = A, \theta), \tag{6.23}$$

where f is the sampling frequency, N_{qp} is the number of quasiparticles, and τ_{qp} is the quasiparticle lifetime. The number of quasiparticles depends on the temperature. In the low temperature condition $T_c \ll T$, the relation between the number of quasiparticles N_{qp} and the device temperature [59] is given by

$$N_{\mathrm{qp}} = 2N_0 V\sqrt{2\pi k_{\mathrm{B}}\Delta_0 T}\exp\left(-\frac{\Delta_0}{k_{\mathrm{B}}T}\right), \tag{6.24}$$

where k_{B} is the Boltzmann constant, N_0 is the single spin density of state at the Fermi level ($1.74\times10^{10}\ \mu\mathrm{eV}^{-1}\mu\mathrm{m}^{-3}$ [76, 77]), and Δ_0 [59] is the gap energy given by

$$2\Delta_0 = 3.52 k_{\mathrm{B}} T_c. \tag{6.25}$$

The quasiparticle lifetime also depends on the temperature, because the pairing rate depends on the number of quasiparticles in the detector. The relation between the quasiparticle lifetime τ_{qp} and the device temperature [79] is given by

$$\tau_{\mathrm{qp}} = \frac{\tau_0}{\sqrt{\pi}}\left(\frac{k_{\mathrm{B}}T_c}{2\Delta_0}\right)^{5/2}\sqrt{\frac{T_c}{T}}\exp\left(\frac{\Delta_0}{k_{\mathrm{B}}T}\right), \tag{6.26}$$

where τ_0 is experimentally measured as $\tau_0 = 458$ ns for an aluminium [80]. The number of quasiparticles in the transmission part is negligible because the superconducting transition temperature of the transmission part is higher than that of the absorb part. The number of quasiparticles and the quasiparticle lifetime due to the thermal loading are shown in Figure 6.4. The number of quasiparticles (the quasiparticle lifetime) increases with increasing (decreasing) the device temperature. The product of the number of quasiparticles and the quasiparticle lifetime is constant

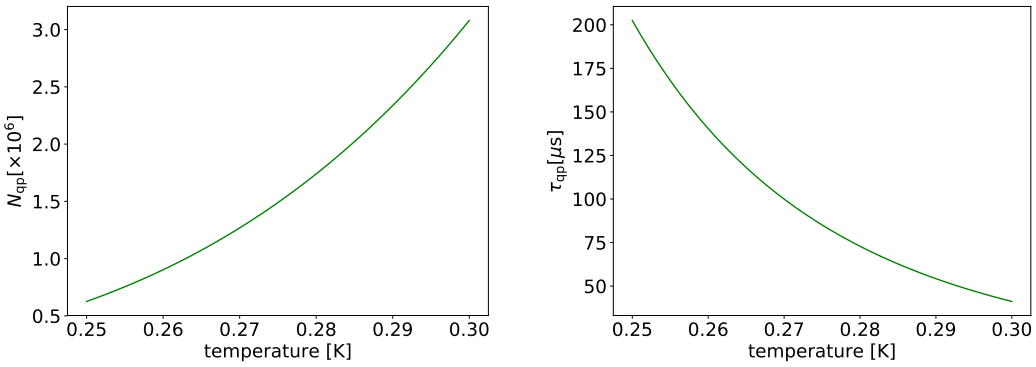

FIGURE 6.4: The number of quasiparticles (left figure) and the quasiparticle lifetime (right figure) as a function of temperature of the prototype MKID design.

with respect to temperature. On the other hand, because the internal quality factor depends on the device temperature, the flat level of the G-R noise PSD slightly depends on the device temperature.

TLS noise model

It is known that the Two Level System (TLS) noise causes the 1/f type noise in PSD of the phase [88, 89]. The TLS noise depends on superconducting and substrate material [91, 94], fabrication process [85], sampling frequency [88, 89, 90, 91, 92], internal power [88, 89, 91, 93], geometry [46, 91, 89, 92], and temperature [90]. J. Gao *et al*. 2007 [88] evaluated the level of the TLS noise of the MKID at $T = 120$ mK and $P_{\text{int}} = -40$ dBm whose center strip width and slot width are 3 μm and 2 μm [43] where P_{int} is the internal power given by

$$P_{\text{int}} = \frac{2}{\pi}\frac{Q_r^2}{Q_c}P_{\text{read}}, \tag{6.27}$$

where P_{read} is the readout power.

After the J. Gao *et al*. (2007) [88], the evaluations of the TLS noise level have been performed with the same geometry and the same condition as the J. Gao *et al*. (2007) [88] for comparison. The resuls of the previous studies are summarized in Ref. [110]. S. Verheul [110] showed that the experimental results of the TLS noise $\frac{S_{\delta fr}}{f_r^2}$ reported before 2019 is well fitted by the following functional form

$$\begin{aligned}\frac{S_{\delta f_r}}{f_r^2} &= \frac{S_{\delta f_r,\text{ref}}}{f_r^2}\left(\frac{f}{f_{\text{ref}}}\right)^k\left(\frac{P_{\text{int}}}{P_{\text{ref}}}\right)^l\left(\frac{Wt}{Wt_{\text{ref}}}\right)^m \\ &= \gamma\frac{S_{\delta f_r,\text{ref}}}{f_r^2},\end{aligned} \tag{6.28}$$

where $\frac{S_{\delta f_r,\text{ref}}}{f_r^2}$ is the reference of the amplitude of the TLS noise, f_{ref} is the reference of the sampling frequency, P_{ref} is the reference of the internal power, Wt is the summation of the center strip width and the slot width ($Wt = s + 2w$), and Wt_{ref} is the reference of the total CPW width. S. Kumar *et al*. (2008) [90] shows the TLS noise $\frac{S_{\delta fr}}{f_r^2}$ is proportional to T^n with $n = -1.1 \sim 2$. By combining these two results, we

propose following model as the TLS noise model given as

$$\begin{aligned}\frac{S_{\delta f_r}}{f_r^2} &= \frac{S_{\delta f_r,\mathrm{ref}}}{f_r^2}\left(\frac{f}{f_{\mathrm{ref}}}\right)^k\left(\frac{P_{\mathrm{int}}}{P_{\mathrm{ref}}}\right)^l\left(\frac{Wt}{Wt_{\mathrm{ref}}}\right)^m\left(\frac{T}{T_{\mathrm{ref}}}\right)^n \\ &= \gamma\frac{S_{\delta f_r,\mathrm{ref}}}{f_r^2},\end{aligned} \tag{6.29}$$

where T_{ref} is the reference of the device temperature. Following the TLS model criteria proposed by J. Gao and S. Verheul, we adopt $f_{\mathrm{ref}} = 1\,\mathrm{kHz}$, $P_{\mathrm{ref}} = -40\,\mathrm{dBm}(10^{-7}\,\mathrm{W})$, $Wt_{\mathrm{ref}} = 7\ \mu\mathrm{m}$, $T_{\mathrm{ref}} = 0.12\ \mathrm{K}$, $m = -1.6$, and $k = -0.5$. It is shown that $l = -0.5$ in high readout power limit [93]. Therefore our TLS model in the calculation is described as

$$\begin{aligned}\frac{S_{\delta f_r}}{f_r^2} &= \frac{S_{\delta f_r,\mathrm{ref}}}{f_r^2}\left(\frac{f}{1\ [\mathrm{kHz}]}\right)^{-0.5}\left(\frac{P_{\mathrm{int}}}{10^{-7}\ [\mathrm{W}]}\right)^{-0.5}\left(\frac{Wt}{7\ [\mu\mathrm{m}]}\right)^{-1.6}\left(\frac{T}{0.12\ [\mathrm{K}]}\right)^{-1.5} \\ &= \gamma\frac{S_{\delta f_r,\mathrm{ref}}}{f_r^2},\end{aligned} \tag{6.30}$$

where $n = -1.5$.

In the case of the hybrid type MKID, the TLS noise [110] is summation of the TLS effect of the absorb part and the transmission part given by

$$\frac{S_{\delta f_r}}{f_r^2} = \frac{S_{\delta f_r,\mathrm{trans}}}{f_r^2} + \frac{S_{\delta f_r,\mathrm{abs}}}{f_r^2}, \tag{6.31}$$

where $\frac{S_{\delta f_r,\mathrm{trans}}}{f_r^2}$ and $\frac{S_{\delta f_r,\mathrm{abs}}}{f_r^2}$ are the reference of the TLS noise of the transmission part and the absorb part. It is known that TLS noise is proportional to $|E|^3$ in the case of high readout power [89]. Since electric field distribution in resonator is proportional to $\cos\left(\frac{\pi}{2}\frac{l'}{l_{\mathrm{tot}}}\right)$ where l' is variable specifying a position in the resonator. The TLS noise model [110] can be described as

$$\frac{S_{\delta f_r,\mathrm{trans}}}{f_r^2} = \gamma_{\mathrm{trans}}\frac{S_{\delta f_r,\mathrm{ref,trans}}}{f_r^2}\frac{\int_0^{l_{\mathrm{trans}}}\cos^3\left(\frac{\pi}{2}\frac{l'}{l_{\mathrm{tot}}}\right)\mathrm{d}l'}{N}, \tag{6.32}$$

and

$$\frac{S_{\delta f_r,\mathrm{abs}}}{f_r^2} = \gamma_{\mathrm{abs}}\frac{S_{\delta f_r,\mathrm{ref,abs}}}{f_r^2}\frac{\int_{l_{\mathrm{trans}}}^{l_{\mathrm{tot}}}\cos^3\left(\frac{\pi}{2}\frac{l'}{l_{\mathrm{tot}}}\right)\mathrm{d}l'}{N}, \tag{6.33}$$

where γ_{abs} and γ_{trans} are the component dependence for the absorb part and the transmission part, respectively, $\frac{S_{\delta f_r,\mathrm{ref,abs}}}{f_r^2}$ and $\frac{S_{\delta f_r,\mathrm{ref,trans}}}{f_r^2}$ are the TLS reference for the absorb part and transmission part, respectively, l_{trans} and l_{tot} is the length of the transmission part and the total length of the resonator. The definition of l_{tot} and l_{trans} is given in Figure 6.5. N is the normalisation factor given by

$$N = \int_0^{l_{\mathrm{tot}}}\cos^3\left(\frac{\pi}{2}\frac{l'}{l_{\mathrm{tot}}}\right)\mathrm{d}l'. \tag{6.34}$$

The amplitude of the TLS noise distribution as a function of length is shown in 6.6. In the figure, the effect of TLS on the feedline side of the resonator is normalized to 1. This figure suggests that the transmission part is the dominant TLS noise source.

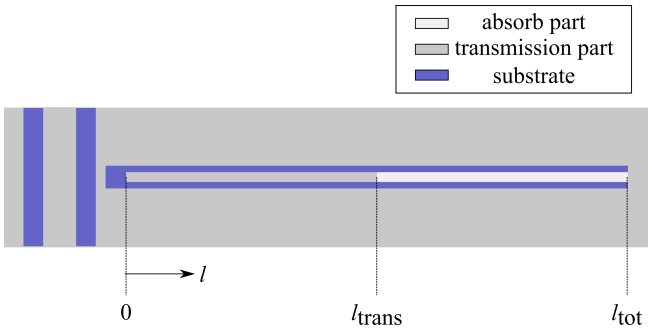

FIGURE 6.5: The length definition of the resonator.

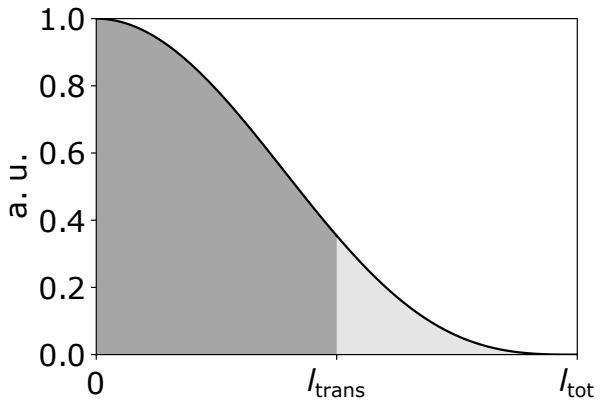

FIGURE 6.6: The TLS noise distribution.

The relation between the frequency TLS noise to the phase TLS noise $S_{\theta,\mathrm{TLS}}$ is given by

$$S_{\theta,\mathrm{TLS}} = (4Q_r)^2 \frac{S_{\delta f_r}}{f_r^2} \frac{1}{1+(2\pi f \tau_{\mathrm{res}})^2}. \tag{6.35}$$

The phase TLS noise has a resonator ring time cut-off [43]. In the formula, the TLS noise depends on the resonator quality factor. However G-R noise PSD also have a Q_r dependence. As a result, Q_r dependence of the TLS and the G-R noises are compensated each other. Therefore, just managing Q_r does not matter for improving the noise level.

When MKID is operated for high readout power, the TLS noise level decreases. However, high readout power results in distortion of the resonance shape and loss of the linear response due to the excess quasiparticles generated by the readout power [71, 72, 73, 74, 57, 75, 65]. The previous study found the evidence that the maximum readout power has a relation of the cross-section area of the CPW line [112]. It is physically reasonable, since current density decreases with increasing the area using same readout power.

Previous study [88, 110] shows the TLS noise reference of aluminum and niobium MKID are both of about -185 dBc/Hz. We adopt this value for the prototype MKID in our calculation. We have to remind that the TLS noise reference depends also on superconducting material, substrate material, and fabrication process.

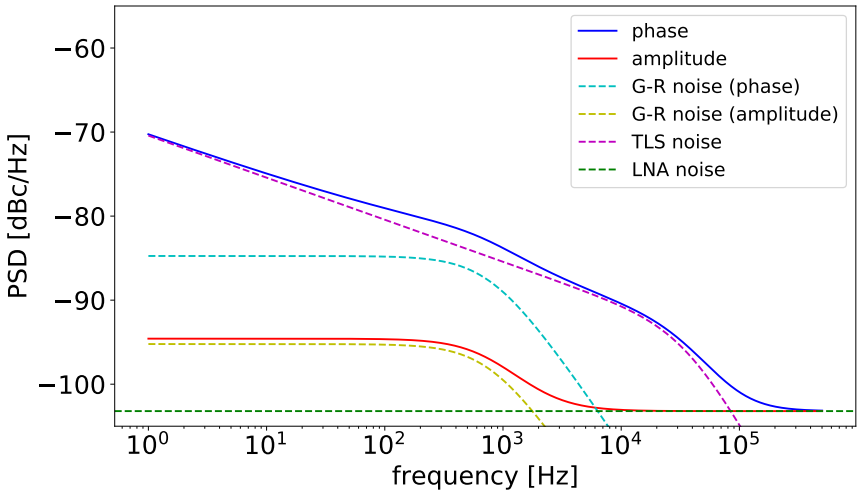

FIGURE 6.7: The PSD of the prototype MKID design, when $P_{\mathrm{read}} = -80$ dBm, $T = 250$ mK, and $T_N = 5$ K. The blue and red solid line show phase and amplitude PSD, respectively. The cyan and yellow dashed line show G-R noise in phase and amplitude, respectively. The magenta and green dashed line show the TLS noise and the LNA noise, respectively.

LNA noise model

The PSD of the LNA (low noise amplifier) noise model $S_{x,\mathrm{LNA}}$ [85] is given by

$$S_{x,\mathrm{LNA}} = \frac{4k_{\mathrm{B}}T_N}{P_{\mathrm{read}}}\left(1+\frac{Q_c}{Q_i}\right)^2 \quad (x = A, \theta), \tag{6.36}$$

where T_N is the LNA thermal noise. The LNA noise level becomes large when $Q_c \gg Q_i$. When we use common mode noise suppression which subtract readout noise using off resonance fluctuation, the noise level becomes 3 dB higher than the value. When there is the connector loss between the device to HEMT amplifier, we need to add the effect in the LNA noise.

PSD model results

When $P_{\mathrm{read}} = -80$ dBm, $T = 250$ mK, and $T_N = 5$ K, the noise contribution of PSD of the prototype MKID design is shown in Figure 6.7. The 1/f type noise from TLS noise is much higher than the G-R noise. Our measurements show that the 1/f type noise dominates and does not observe the clear G-R noise in the PSD of the phase, as mentioned in Chapter 3. This can be explained by this model. When $P_{\mathrm{read}} = -80$ dBm, and $T_N = 5$ K, PSD of the prototype MKID design in various device temperature and readout power is shown in Figure 6.8. As a results, the 1/f type noise is dominant in any case.

6.1.3 NEP model

The noise equivalent power (NEP) is the sensitivity of a detector system. It is defined as the signal power that is a signal-to-noise ratio of one in one hertz bandwidth. The

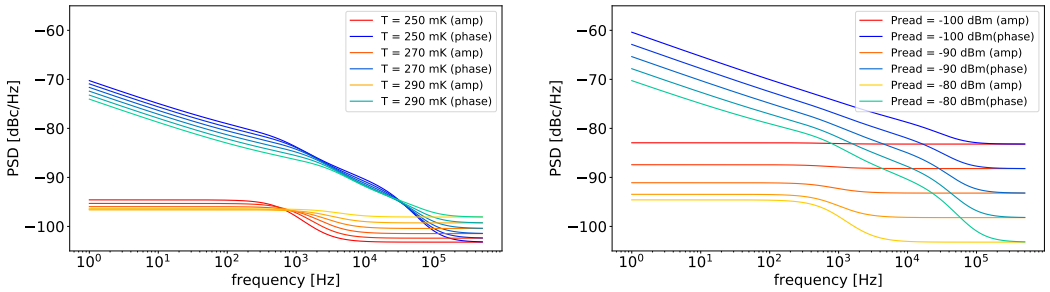

FIGURE 6.8: The PSD of the prototype MKID design in various device temperature (left figure) and readout power (right figure). The device temperature is from 250 mK to 300 mK in 10 mK steps. The readout power is from −100 dBm to −80 dBm in 5 dBm steps.

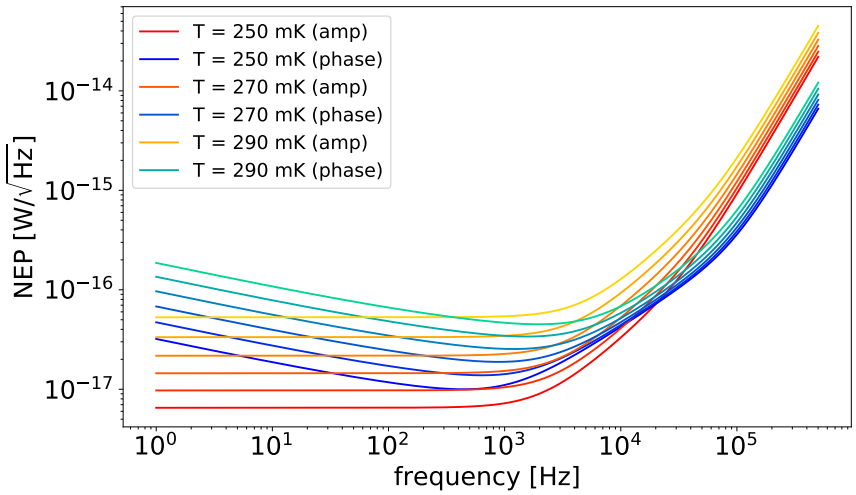

FIGURE 6.9: The NEP of the prototype MKID design in various device temperature. The device temperature is from 250 mK to 300 mK in 10 mK steps.

NEP for the dark condition is given by

$$NEP = \sqrt{S_x}\left(\frac{\mathrm{d}x}{\mathrm{d}P}\right)^{-1}\sqrt{1+(2\pi f\tau_{\mathrm{qp}})^2}\sqrt{1+(2\pi f\tau_{\mathrm{res}})^2}\ (x=A,\theta), \tag{6.37}$$

where $\mathrm{d}x/\mathrm{d}P$ is the power responsivity [78] given by

$$\frac{\mathrm{d}x}{\mathrm{d}P} = \frac{\eta_{\mathrm{pb}}\tau_{\mathrm{qp}}}{\Delta_0}\frac{\mathrm{d}x}{\mathrm{d}N_{\mathrm{qp}}}\ (x=A,\theta), \tag{6.38}$$

where η_{pb} is the pair braking efficiency [60, 61] (0.57 for an aluminum). The power responsvity of the amplitude and the phase at $T = 250$ mK are $\mathrm{d}A/\mathrm{d}P = -7.6\times10^{12}$ /W and $\mathrm{d}\theta/\mathrm{d}P = 2.8\times10^{13}$ rad/W, respectively, where $\alpha_k = 0.04$, $V = 920\ \mu$m, $\beta_\lambda = 1.6$, and $Q_r = 5.6\times10^4$ same as the calculation of the prototype MKID design. When $P_{\mathrm{read}} = -80$ dBm and $T_N = 5$ K, the NEP of the prototype MKID design in various device temperature are shown in Figure 6.9. As a results, the NEP is also limited by the TLS noise of the prototype MKID in any case.

6.2 Modeling for optically bright condition

Under the optically bright condition, the main origin of the quasiparticles in the MKID is due to the optical loading. Therefore the number of quasiparticles in absorb part increases and the internal quality factor and the resonance frequency decreases comparing for the dark condition. Since the spectrum of the optical source is Planck's law in both of the conventional measurement and the atmospheric observation as mentioned in next section, we consider the optical loading is as thermal radiation in this section. The fluctuation of the photon number from the thermal radiation is added to the PSD model and NEP model of the dark condition.

6.2.1 Number of quasiparticles

For the optically bright condition, we consider the number of quasiparticles generated by the optical loading and the thermal loading. The total quasiparticles, $N_{\mathrm{qp,tot}}$, is the summation of the number of quasiparticles generated by the optical loading and the thermal loading given by

$$N_{\mathrm{qp,tot}} = N_{\mathrm{qp,th}} + N_{\mathrm{qp,abs}}, \tag{6.39}$$

where $N_{\mathrm{qp,th}}$ is the number of quasiparticles due to the thermal loading given by Eq. (6.24) and $N_{\mathrm{qp,abs}}$ is the number of quasiparticles due to the optical loading. Since the quasiparticle lifetime lineally decreases with increasing the number density of quasiparticles, the relation between the quasiparticle lifetime and the number of quasiparticles [79] is given by

$$\tau_{\mathrm{qp,tot}} = \frac{\tau_0 V}{N_{\mathrm{qp,tot}}} \frac{N_0 (k_{\mathrm{B}} T_c)^3}{2\Delta_0^2} = \frac{X}{N_{\mathrm{qp,tot}}} \left(X = \tau_0 V \frac{N_0 (k_{\mathrm{B}} T_c)^3}{2\Delta_0^2} \right). \tag{6.40}$$

To calculate the quasiparticles due to the optical loading, the relation between the number of quasiparticles due to the optical loading [78] is given by

$$N_{\mathrm{qp,abs}} = \frac{\eta_{\mathrm{pb}} \tau_{\mathrm{qp,tot}}}{\Delta_0} P_{\mathrm{abs}}, \tag{6.41}$$

where P_{abs} is the absorbed power in the MKID due to the optical loading. Using Eqs. (6.39), (6.40), and (6.41), the number of quasiparticles due to the optical loading is obtained as

$$N_{\mathrm{qp,abs}} = \frac{-N_{\mathrm{qp,th}} + \sqrt{N_{\mathrm{qp,th}}^2 + 4\eta_{\mathrm{pb}} X P_{\mathrm{abs}} / \Delta_0}}{2}. \tag{6.42}$$

The relation between the absorbed power and the quasiparticle lifetime of the prototype MKID design is shown in Figure 6.10. The quasiparticle lifetime decreases with increasing the absorbed power as expected.

6.2.2 The quality factors and the resonance frequency for the optically bright condition

The inverse of the total quality factor $Q_{i,\mathrm{tot}}$ is the summation of the inverse of internal quality factors due to the optical loading and the thermal loading which is given by

$$\frac{1}{Q_{i,\mathrm{tot}}} = \frac{1}{Q_{i,\mathrm{th}}} + \frac{1}{Q_{i,\mathrm{abs}}}, \tag{6.43}$$

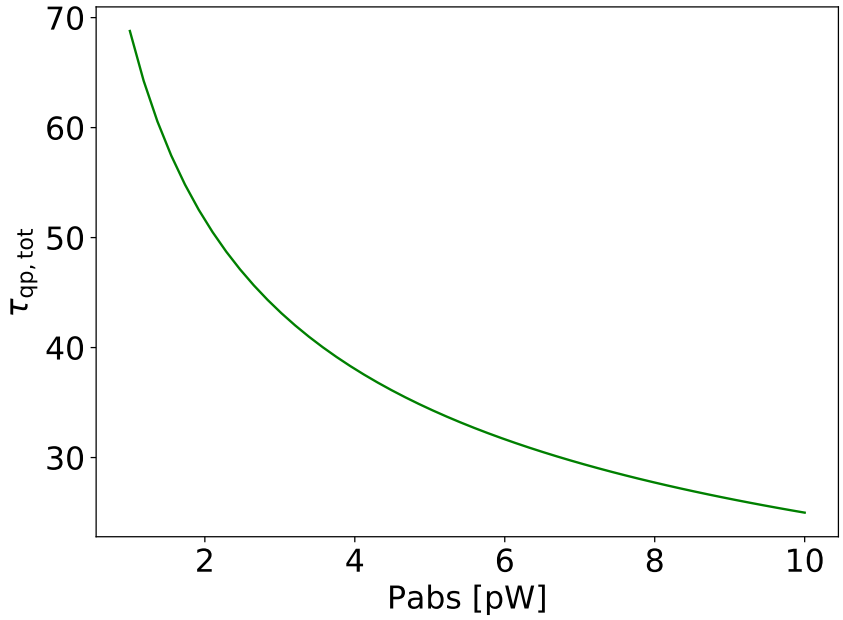

FIGURE 6.10: The quasiparticle lifetime of the prototype MKID design in various absorbed power.

where $Q_{i,\mathrm{th}}$ [85] is the internal quality factor due to the thermal loading given by Eq. (6.15) and $Q_{i,\mathrm{abs}}$ is the internal quality factor due to the optical loading given by

$$\frac{1}{Q_{i,\mathrm{abs}}} = \frac{\delta(1/Q_i)}{\delta N_{\mathrm{qp}}} N_{\mathrm{qp,abs}}, \tag{6.44}$$

where $\frac{\delta(1/Q_i)}{\delta N_{\mathrm{qp}}}$ is the responsivity of the internal quality factor given by

$$\frac{\delta(1/Q_i)}{\delta N_{\mathrm{qp}}} = \frac{\alpha_k \beta_\lambda}{2\sigma_2 V} \frac{\delta\sigma_1}{\delta n_{\mathrm{qp}}}, \tag{6.45}$$

where $\frac{\delta\sigma_1}{\delta n_{\mathrm{qp}}}$ is the responsvity of the complex conductivity given by Eq. 2.7. The internal quality factor of the optically bright condition is lower than that of the dark condition due to the optical loading. The relation between the internal quality factor and the absorbed power is shown in Figure 6.11. The internal quality factor decreases with increasing the optical loading.

Since the coupling quality factor does not depend on the optical loading, the total resonator quality factor $Q_{r,\mathrm{tot}}$ is given by

$$\frac{1}{Q_{r,\mathrm{tot}}} = \frac{1}{Q_{i,\mathrm{tot}}} + \frac{1}{Q_c}. \tag{6.46}$$

The resonance frequency decreases with increasing the optical loading. The responsivity of the resonance frequency is given by

$$\frac{\delta f_r / f_{r0}}{\delta N_{\mathrm{qp}}} = \frac{\alpha_k \beta_\lambda}{4\sigma_2 V} \frac{\delta\sigma_2}{\delta n_{\mathrm{qp}}}. \tag{6.47}$$

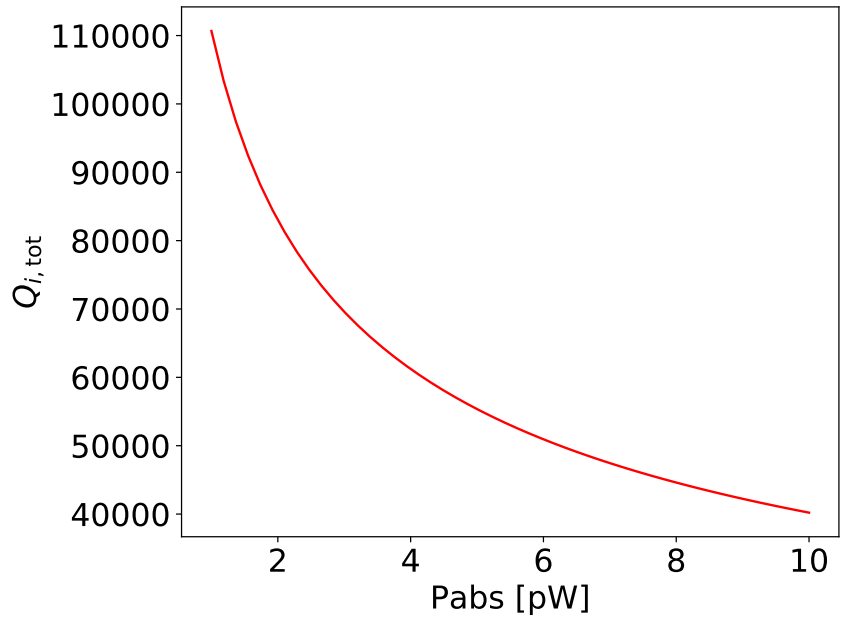

FIGURE 6.11: The internal quality factor of the prototype MKID design in various absorbed power.

Using Eq. (6.14), the resonance frequency for the optically bright condition is given by

$$f_{r,\mathrm{tot}} = \left(1 + \frac{\alpha_k \beta_\lambda}{4\sigma_2 V}\frac{\delta\sigma_2}{\delta n_{\mathrm{qp}}} N_{\mathrm{qp,tmp}} + \frac{\alpha_k \beta_\lambda}{4\sigma_2 V}\frac{\delta\sigma_2}{\delta n_{\mathrm{qp}}} N_{\mathrm{qp,abs}}\right) f_{r0}, \tag{6.48}$$

where the second term of the right hand side is due to the thermal loading and the third term of the right hand side is due to the optical loading.

The complex transmission S_{21} as a function of readout frequency of the prototype MKID design in various absorbed power is shown in Figure 6.12. The resonance frequency decreases with increasing the optical power. The resonance depth decreases with increasing the absorbed power.

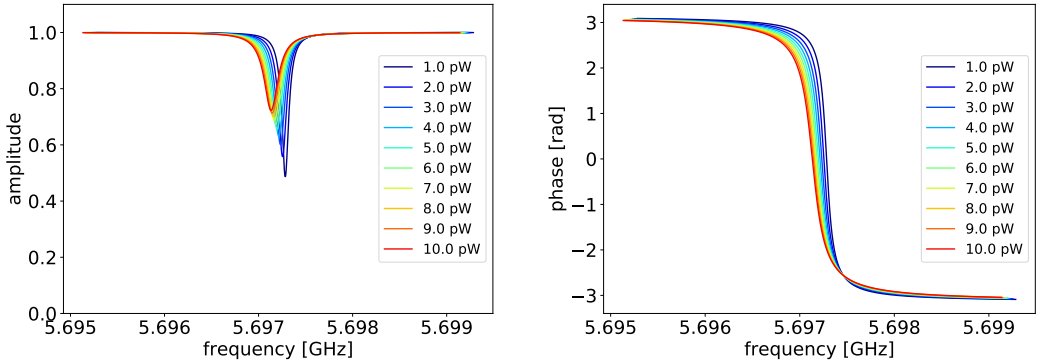

FIGURE 6.12: The amplitude (left figure) and the phase (right figure) of the complex transmission S21 of the prototype MKID design in various absorbed power.

The resonator ring time for the optically bright condition $\tau_{\mathrm{res,tot}}$ is given by

$$\tau_{\mathrm{res,tot}} = \frac{Q_{r,\mathrm{tot}}}{\pi f_{r,\mathrm{tot}}}. \tag{6.49}$$

It becomes shorter than the time of the dark condition due to decreasing the resonator quality factor.

6.2.3 PSD model

The components of the PSD for the optically bright condition are the LNA noise, the TLS noise, the G-R noise, and the photon noise. The summation of the G-R noise and the photon noise is called the BLIP (Background LImited Performance) noise. Therefore, the noise level of the optically bright condition is higher than that of the dark condition. The amplitude PSD for the optically bright condition is summation of the LNA noise and the BLIP noise given by

$$S_A = S_{A,\mathrm{BLIP}} + S_{A,\mathrm{LNA}}, \tag{6.50}$$

and the phase PSD for the optically bright condition is summation of the LNA noise and the TLS noise and the BLIP noise given by

$$S_\theta = S_{\theta,\mathrm{TLS}} + S_{\theta,\mathrm{BLIP}} + S_{\theta,\mathrm{LNA}}. \tag{6.51}$$

For the photon noise observation, the LNA noise and the TLS noise needs to be less than the BLIP noise.

The BLIP noise is the summation of the G-R noise $S_{x,\mathrm{G-R}}$ and the photon noise $S_{x,\mathrm{photon}}$ given by

$$S_{x,\mathrm{BLIP}} = S_{x,\mathrm{G-R}} + S_{x,\mathrm{photon}}. \tag{6.52}$$

The G-R noise due to the optical loading is given by

$$S_{x,\mathrm{G-R}} = \frac{4\Delta_0^2 N_{\mathrm{qp,tot}}/\eta_{\mathrm{pb}}^2 \tau_{\mathrm{qp,tot}}}{[1+(2\pi f\tau_{\mathrm{qp,tot}})^2][1+(2\pi f\tau_{\mathrm{res,tot}})^2]} \left(\frac{\mathrm{d}x}{\mathrm{d}P_{\mathrm{abs}}}\right)^2 \ (x = A, \theta), \tag{6.53}$$

where $\mathrm{d}x/\mathrm{d}P_{\mathrm{abs}}$ is the responsivity for the optically bright condition[78] is given by

$$\frac{\mathrm{d}x}{\mathrm{d}P_{\mathrm{abs}}} = \frac{\eta_{\mathrm{pb}}\tau_{\mathrm{qp,tot}}}{\Delta_0}\frac{\mathrm{d}x}{\mathrm{d}N_{\mathrm{qp}}} \ (x = A, \theta). \tag{6.54}$$

The PSD of the photon noise $S_{x,\mathrm{photon}}$ is given by

$$S_{x,\mathrm{photon}} = \frac{2h\nu P_{\mathrm{abs}}(1+\eta_{\mathrm{opt}}\eta_{\mathrm{em}}\bar{n})}{[1+(2\pi f\tau_{\mathrm{qp,tot}})^2][1+(2\pi f\tau_{\mathrm{res,tot}})^2]} \left(\frac{\mathrm{d}x}{\mathrm{d}P_{\mathrm{abs}}}\right)^2 \ (x = A, \theta), \tag{6.55}$$

where h is the Planck constant, ν is the optical frequency, η_{em} is the emissivity of the thermal radiation, η_{opt} is the optical efficiency which is the ratio of the absorbed power to radiation power P_{rad}, and $\bar{n}$ is the photon occupation number given by

$$\bar{n} = \frac{1}{\exp\left(\frac{h\nu}{k_{\mathrm{B}}T}\right) - 1}. \tag{6.56}$$

Therefore, the PSD of the BLIP noise is given by

$$\begin{aligned} S_{x,\mathrm{BLIP}} &= \frac{2h\nu P_{\mathrm{abs}}(1+\eta_{\mathrm{opt}}\eta_{\mathrm{em}}\bar{n}) + 4\Delta_0^2 N_{\mathrm{qp,tot}}/\eta_{\mathrm{pb}}^2\tau_{\mathrm{qp,tot}}}{[1+(2\pi f\tau_{\mathrm{qp,tot}})^2][1+(2\pi f\tau_{\mathrm{res,tot}})^2]}\left(\frac{\mathrm{d}x}{\mathrm{d}P_{\mathrm{abs}}}\right)^2 \ (x=A,\theta) \\ &= \frac{2h\nu P_{\mathrm{rad}}(1+\eta_{\mathrm{opt}}\eta_{\mathrm{em}}\bar{n}) + 4\Delta_0^2 N_{\mathrm{qp,tot}}/\eta_{\mathrm{pb}}^2\tau_{\mathrm{qp,tot}}}{\eta_{\mathrm{opt}}[1+(2\pi f\tau_{\mathrm{qp,tot}})^2][1+(2\pi f\tau_{\mathrm{res,tot}})^2]}\left(\frac{\mathrm{d}x}{\mathrm{d}P_{\mathrm{rad}}}\right)^2 \ (x=A,\theta), \end{aligned} \tag{6.57}$$

where P_{abs} is the absorbed power given by $P_{\mathrm{abs}} = \eta_{\mathrm{opt}} P_{\mathrm{rad}}$.

The parameters included in the PSD of the TLS noise given by Eq. (6.35), and LNA noise given by Eq. (6.36) are converted from Q_i, Q_r, f_r, τ_{qp}, and τ_{res} to $Q_{i,\mathrm{tot}}$, $Q_{r,\mathrm{tot}}$, $f_{r,\mathrm{tot}}$, $\tau_{\mathrm{qp,tot}}$, and $\tau_{\mathrm{res,tot}}$ in the optically bright condition.

6.2.4 NEP model for optically bright condition

The optical efficiency is ratio of the absorbed power to the radiation power as mentioned in last subsection. When the NEP is dominated by the BLIP noise, we can obtain the optical efficiency by comparing the theoretical NEP and the measured NEP [110, 109], because the difference between these NEP comes from the optical efficiency.

The theoretical NEP NEP_{theory} [57, 113] is given by

$$NEP_{\mathrm{theory}} = \sqrt{\frac{2h\nu P_{\mathrm{rad}}(1+\eta_{\mathrm{opt}}\eta_{\mathrm{em}}\bar{n}) + 4\Delta_0 P_{\mathrm{rad}}/\eta_{\mathrm{pb}}}{\eta_{\mathrm{opt}}}} \tag{6.58}$$

The measured NEP for the optically bright condition is given by

$$NEP = \sqrt{S_x}\left(\frac{\mathrm{d}x}{\mathrm{d}P_{\mathrm{rad}}}\right)^{-1}\sqrt{1+(2\pi f\tau_{\mathrm{qp,tot}})^2}\sqrt{1+(2\pi f\tau_{\mathrm{res,tot}})^2}\ (x=A,\theta), \tag{6.59}$$

where $\mathrm{d}x/\mathrm{d}P_{\mathrm{rad}}$ is the rate of change of the phase and amplitude response for the radiation power.

6.2.5 Summary of Reliability check

The comparison of the model results and the measurement results as mentioned in Chapter 3 is summarized in Table 6.4. The difference of the model and the measurement is less than 70%. We estimate the tiny deference of the measured results and results by the forecaster is came from the production errors. It confirms that our forecaster provides reasonably good evaluation of the MKID performance.

We check our PSD model comparing previous results by S. Verheul in Figure 6.2 left figure in Ref [110]. He modeled aluminum and niobium titanium nitraide hybrid type MKID at $T = 270$ mK. We obtained the same results.

We extended to this model to the optically bright condition. Since unfortunately the performance of the MKID installed in the GroundBIRD telescope is quite low, we could not compare the measurement results and results by the forecaster in the optically bright condition.

6.3 Application of forecaster to evaluate performance of the prototype MKID in optically bright condition

Since the 1/f type noise is higher than the BLIP noise in the previous GroundBIRD measurement [114, 97] and the observation results in the optically bright condition [53], the performance of the prototype MKID mounted on the GroundBIRD telescope does not reached the BLIP noise limit. In this section, we pursue this reason using our forecaster.

We forecast the performance of the prototype MKID in the conventional blackbody measurement and the atmospheric observation by the GroundBIRD.

The following shows the requirements of the MKID performance for these measurement and observation.

- The detector noise is dominated by the BLIP noise in the conventional balckbody measurement.
- The detector noise is dominated by the BLIP noise in the atmospheric observation.
- The 1/f type noise from TLS noise is less than GroundBIRD rotation scan speed (< 0.3 Hz) for the atmospheric observation.

6.3.1 The measurement with blackbody source

Setting blackbody source for which temperature of the source is controllable by manipulating heater in front of the detector is the conventional method for the optical efficiency measurement [109], here after we refer it controllable balckbody. The method is to measure the response of MKID while controlling the temperature of the blackbody source in front of the detector. By comparing the measured NEP given by Eq. (6.59) with the theoretical NEP given by Eq. (6.58), the optical efficiency can be obtained when the detector NEP is dominated by the BLIP noise. Advanced Technology Center, NAOJ has this system [114, 115] and we use this system for our MKID evaluation.

We calculate the MKID response and noise of the prototype MKID design using the controllable blackbody. We define the radiation power is product of the filter transmission and the blackbody radiation given by

$$P_{\rm rad} = \frac{1}{2}\int \left(\frac{c}{\nu}\right)^2 F(\nu)B(\nu,T)\mathrm{d}\nu, \tag{6.60}$$

where c is the speed of light, $F(\nu)$ is the filter transmission, and $B(\nu,T)$ is the source brightness given by

$$B(\nu,T) = \frac{2h\nu^3}{c^2}\frac{1}{\exp\left(\frac{h\nu}{k_{\rm B}T}\right)-1}. \tag{6.61}$$

We forecast the performance of the prototype MKID for the controllable balckbody measurement with the same band pass filter which is used in front of the detector in the GroundBIRD telescope. As mentioned in Chapter 1,the GrondBIRD telescope has two bands whose center frequencies are 145 GHz and 220 GHz, respectively. The filter transmissions as a function of frequency for 145 GHz band and 220 GHz band are shown in Figure 6.13. The filter transmissions for 145 GHz band and 220 GHz band are about 80% and 70%, respectively.

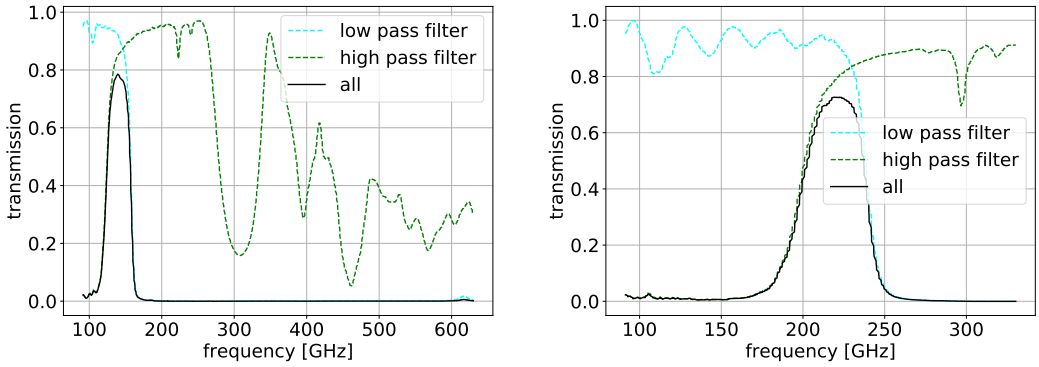

FIGURE 6.13: The filter transmissions for 145 GHz band (left figure) and 220 GHz band (right figure). The filter is used by high pass and low pass filter at 250 mK stage of the GroundBIRD. The cyan dashed line shows the transmission of the low pass filter. The green dashed line shows the transmission of the high pass filter. The black line shows the sum of the transmission of high pass and low pass filters.

Temperature dependence of the amplitude of various noise components at sampling frequency of 1 Hz and 100 Hz are shown in Figure 6.14 for 145 GHz and Figure 6.15 for 220 GHz. As a results, even at 100 Hz, the TLS noise dominates over other noise sources both of 145 GHz and 220 GHz band. This is the main reason why we could not measure optical efficiency by measurement described in Ref. [115, 114].

6.3.2 The forecasting of the atmospheric observation by the GroundBIRD with the prototype MKID

We forecast the performance of the prototype MKID for the observation and conventional onsite calibration. The main optical loading in the observation is atmospheric emission. The atmospheric emission in the GroundBIRD observational site is as mentioned in Chapter 1. The liquid nitrogen (LN2) and room temperature (300 K) blackbody source covering the telescope window is the conventional calblation method of the optical response (hot and cold method) as mentioned in Appendix C.

For calculating the optical loading, we applied the total transmission of the summation of the GroundBIRD optical filter for 145 GHz band and 220 GHz band, and the atmospheric transmission given in Figure 1.6 and in Figure 1.7, respectively. When $\eta_{\mathrm{opt}} = 0.39$ [54, 66, 67] for 145 GHz and $\eta_{\mathrm{opt}} = 0.30$ [54, 68, 67] for 220 GHz, PWV $= 3.8$ mm, $P_{\mathrm{read}} = -80$ dBm, and $T_N = 5$ K, the complex transmission of the prototype MKID as a function of readout frequency for 145 GHz band and 220 GHz band for each observations are shown in Figure 6.16 and Figure 6.17, respectively, and the PSD with the atmospheric observation for 145 GHz (220 GHz) is shown in Figure 6.18 (Figure 6.19). In the calculation, the absorbed power for each situation are summarized in Table 6.5.

Figures 6.16 and 6.17 show that the value of the internal quality factor and that of coupling quality factor are about same for the atmospheric observation.

Our results show that the performance of the prototype MKID is not the BLIP noise limit. In the phase PSD at 1 Hz, the TLS noise is 13 dB higher than the BLIP noise. According to the observational results by the GroundBIRD [53], we could not

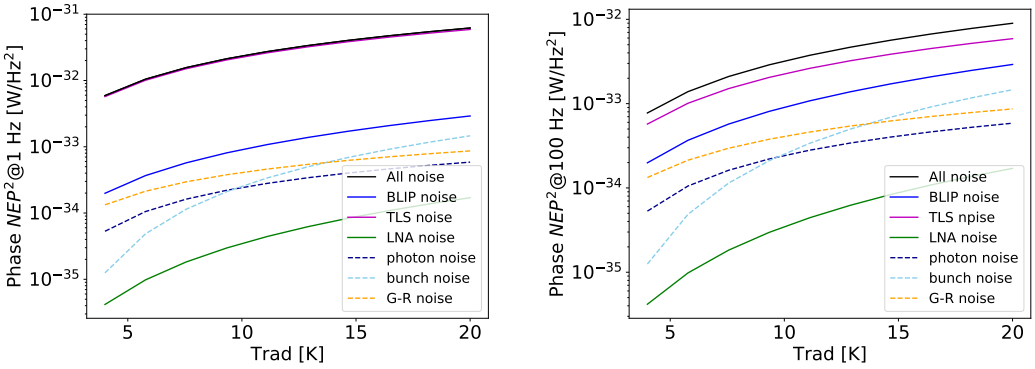

FIGURE 6.14: The each component and summation of the phase NEP at 1 Hz (left figure) and at 100 Hz (right figure) of the prototype MKID design of 145 GHz band in the controllable blackbody measurement. The black line shows the summation of NEP in the phase. The magenta, green, and blue solid lines show the TLS noise, the LNA noise, and the BLIP noise. The dark blue, cyan, and orange dashed lines show the photon, the photon bunch, and the G-R noise.

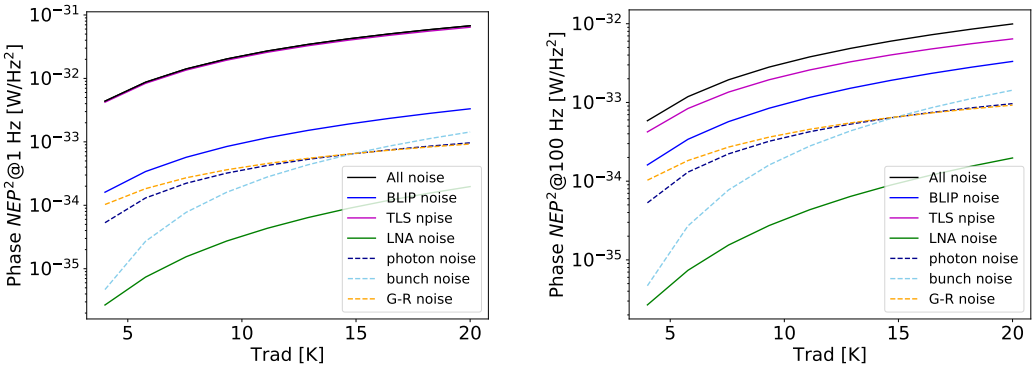

FIGURE 6.15: The each component and summation of the phase NEP at 1 Hz (left figure) and at 100 Hz (right figure) of the prototype MKID design of 220 GHz band in the controllable blackbody measurement. The black line shows the summation of NEP in the phase. The magenta, green, and blue solid lines show the TLS noise, the LNA noise, and the BLIP noise. The dark blue, cyan, and orange dashed lines show the photon, the photon bunch, and the G-R noise.

	145 GHz	220 GHz
atmosphere (PWV = 3.8 mm) [pW]	3	5
LN2 [pW]	8	7
300 K [pW]	30	29

TABLE 6.5: The absorbed power in the calculation.

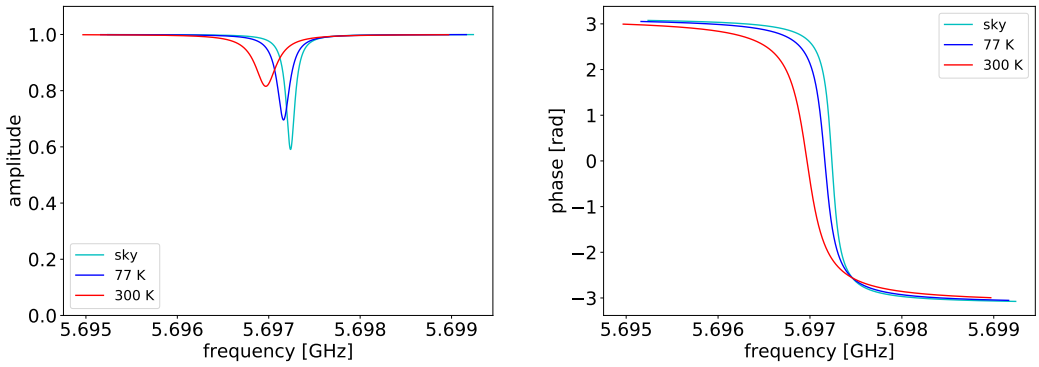

FIGURE 6.16: The amplitude (left figure) and the phase (right figure) of the complex transmission S_{21} as a function of readout frequency of the prototype MKID design of 145 GHz band in atmospheric (PWV = 3.8 mm, cyan solid line), LN2 (blue solid line), and 300 K (red solid line) radiation.

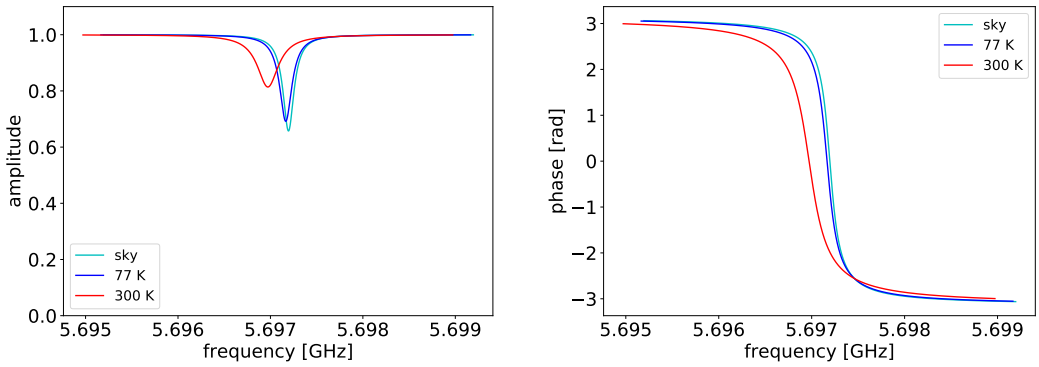

FIGURE 6.17: The amplitude (left figure) and the phase (right figure) of the complex transmission S_{21} as a function of readout frequency of the prototype MKID design of 220 GHz band in atmospheric (PWV = 3.8 mm, cyan solid line), LN2 (blue solid line), and 300 K (red solid line) radiation.

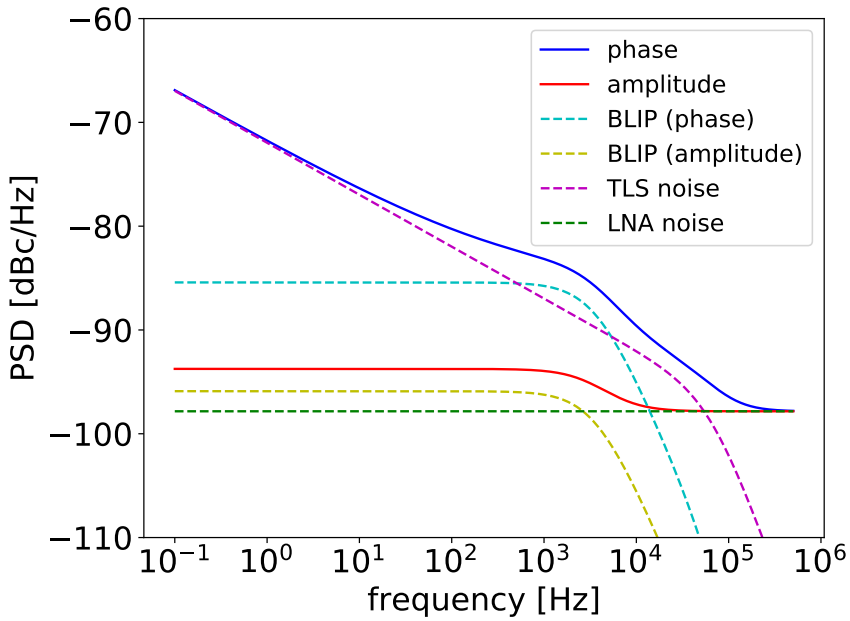

FIGURE 6.18: The each component of PSD (TLS noise, BLIP noise and LNA noise) and sum of the PSD of the prototype MKID design of 145 GHz band in atmospheric (PWV = 3.8 mm) observation. The red and blue lines show the summation of the PSD in the amplitude and the phase. The magenta, green, yellow, and cyan dashed line show the TLS noise, the LNA noise, the amplitude of the BLIP noise, and the phase of that, respectively.

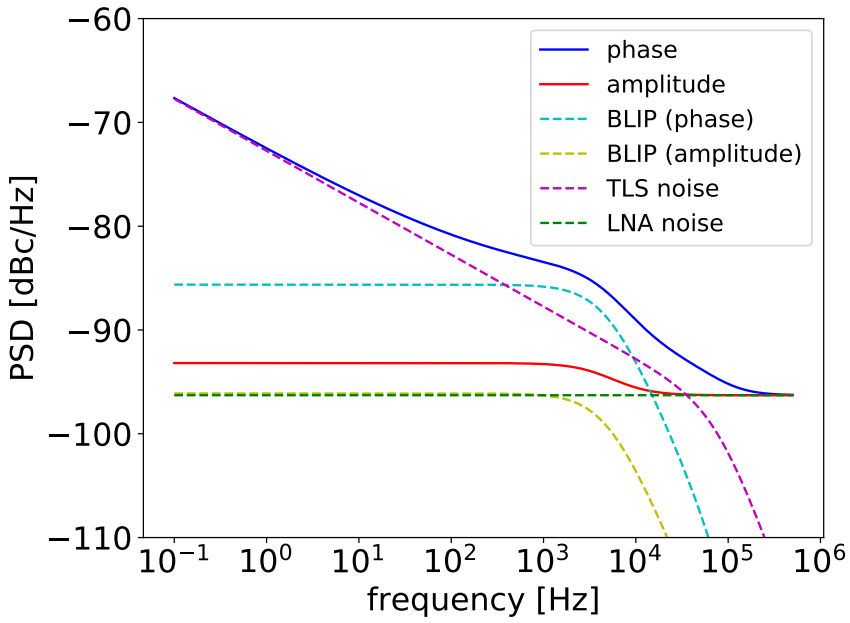

FIGURE 6.19: The each component of PSD (TLS noise, BLIP noise and LNA noise) and sum of the PSD of the prototype MKID design of 220 GHz band in atmospheric (PWV = 3.8 mm) observation. The red and blue lines show the summation of the PSD in the amplitude and the phase. The magenta, green, yellow, and cyan dashed line show the TLS noise, the LNA noise, the amplitude of the BLIP noise, and the phase of that, respectively.

measure the BLIP noise for MKID device (The MKID design is not same as mentioned in this chapter) mounted on the GroundBIRD telescope due to the high 1/f type noise. This can be explained by this model.

6.4 The problems and improvement of the prototype MKID for the GroundBIRD observation.

It is found that the prototype MKID design is not suitable for the GroundBIRD observations. The following is summary of the problems and improvements for the new design.

- The 1/f type noise from the TLS noise is higher than the BLIP noise. The 1/f type noise needs to be less than the BLIP noise at the GroundBIRD rotational speed (0.3 Hz). As mentioned in Chapter 2 and this chapter, the TLS noise is reduced using the large geometry (see Appendix D).
- Since the BLIP noise level depends on the responsivity of the MKID, to get high responsivity is also important. The responsvitity depends on the volume of the absorb part as mentioned in Chapter 3. Using small volume of the absorb part also solves the 1/f type noise problem.

We propose the new MKID design for the GroundBIRD observation to solve the problems in the next Chapter.

6.5 Discussion and Conclusion

We develop the MKID performance forecaster. It is dramatic reduction of the time consumption for the MKID research and development cycle. At first, we model the performance of the hybrid type MKID in the dark condition. We add the temperature dependence in the TLS noise model based on the previous study. We compare the parameters calculated by the forecaster and results as mentioned in Chapter. 3. The difference of these results is less than 70%. It confirms that our forester provides reasonably good evaluation of the MKID performance in the dark condition. We also checked our PSD model comparing previous results by S. Verhuel [110] and we obtain same results. We expand the model for the optically bright condition and forecast MKID performance in the conventional blackbody measurement and GroundBIRD observation.

The results explain why the prototype MKID does not achieve the BLIP noise in our past measurement. The 1/f type noise of the prototype in the atmospheric observation condition is higher than the BLIP noise at 100 Hz. The 1/f type noise needs to be less than the BLIP noise at the GroundBIRD rotational speed (0.3 Hz). In the next chapter, we propose new design to solve the problem using the forecaster.

As mentioned in Chapter 4, Chapter 5, and previous study [71, 72, 73, 74, 57, 75, 65], the excess quasiparticles are also generated by the readout power. We will model and include this effect in our forecaster for the future.

More detail comparison between the results from the forecaster and our measurement results is necessary for future work. Based on the real measurement results, we have a plan to feed back to the model improvement.

The other advantage of the development of the forecaster is to estimate superconducting properties, TLS noise, and optically bright conditions at one time. Commercial electromagnetic simulation software is unable or limited in its ability to simulate

these components. And, the forecaster takes less calculation time than the commercial simulation software.

Chapter 7

New MKID design for the GroundBIRD

We develop MKID performance forecaster introduced in the previous chapter. The performance of the prototype MKID design is not suitable for the GroundBIRD observation. The 1/f type noise due to the TLS noise is much higher than the BLIP noise. We optimize the geometry of the new design MKID using the forecaster in order to suppress the 1/f type noise less down to the BLIP noise at the GroundBIRD rotational speed (0.3 Hz). We forecast the performance of new MKID design in the controllable blackbody measurement and GroundBIRD observation.

7.1 The design optimization for the GroundBIRD observation

In the previous chapter, it is found that the prototype MKID design is not suitable for the GroundBIRD observation. The following is summary of the problems of the prototype MKID and improvements of the new design.

- The 1/f type noise from the TLS noise is higher than the BLIP noise. The 1/f type noise should be less than the noise level of the BLIP noise above the rotation scan frequency of the GroundBIRD (0.3 Hz). As mentioned in Chapter 2 and Chapter 6, the TLS noise is able to be reduced by enlarging size of the resonator (see Appendix D). To suppress the 1/f type noise, we optimize the geometry of the CPW line of the transmission part.
- Since the amplitude of the BLIP noise increases with improving the responsivity of the MKID while keeping the 1/f type noise level, the improving responsivity is the another approach to reduce the relative contribution of the 1/f type noise to the BLIP noise. It is realized by increasing responsivity with decreasing volume of the absorb part and adjusting the length of the transmission part.

In this section, we describe the optimization of the MKID design for the GroundBIRD observation. The material parameters in Table 7.1 are used in the optimization. At first, we optimize the effect of the Low Noise Amplifier noise (LNA noise) in PSD phase noise. As shown in the previous chapter, since the BLIP noise of the phase is higher than that of the amplitude, the phase PSD is less affected by the LNA noise than amplitude PSD. Therefore, we consider only phase PSD in this section. Since the value of the internal quality factor Q_i and that of the coupling quality factor Q_c should optimize to the GroundBIRD atmospheric observation, the optimized LNA

	Aluminum	Niobium	reference
T_c	1.28 K	9.2 K	[65, 85]
ρ_N	1.5 $\mu\Omega \cdot$ cm	5 $\mu\Omega \cdot$ cm	[110, 85]
S_{ref}/f_r^2	-185 dB	-185 dB	[88, 110]

TABLE 7.1: The material parameters for new MKID design. The absorb, and transmission material are Aluminum and Niobium, respectively. T_c is the superconducting transition temperature. ρ_N is the low temperature resistivity. S_{ref}/f_r^2 is the TLS reference parameter described in the previous chapter.

noise $S_{\mathrm{LNA,opt}}$ using Eq. 6.36 is given by

$$S_{\mathrm{LNA,opt}} = \frac{16 k_{\mathrm{B}} T_N}{P_{\mathrm{read}}}, \tag{7.1}$$

where T_N is the thermal noise temperature of the amplifier and P_{read} is the readout power. As shown in Eq. 6.57, the BLIP noise of the PSD is proportional to square of the phase response, $\mathrm{d}\theta/\mathrm{d}P_{\mathrm{abs}}$. As shown in Eq. 6.54, the phase response of the MKID is proportional to the change of the quasiparticle, $\mathrm{d}\theta/\mathrm{d}N_{\mathrm{qp}}$. As shown in Eq. 6.19, $\mathrm{d}\theta/\mathrm{d}N_{\mathrm{qp}}$ is almost proportional to inverse of the volume of the absorb part. Therefore, to increase the sensitivity, the volume of the absorb part should be smaller. Further, this results in increase of the BLIP noise. As a result, the noise contribution due to the LNA becomes less significant. We change the center strip width of the absorb part from 4 μm to 2 μm and the thickness of the absorb part from 0.1 μm to 0.05 μm from the prototype design to the new design. The values are the limits of that our fabrication process can produce stably. We did not change the length of the absorb part because the optical efficiency becomes smaller when the length of the absorb part is shortened [110].

We optimize the length of the transmission part. Since the readout frequency band of the GroundBIRD telescope is $4-8$ GHz limited by the frequency range of the HEMT amplifier at 4 K stage, we need to optimize the resonance frequency within the readout frequency range. Since the resonance frequency depends on the length of the resonator, we calculate the relation between the resonance frequency and the length of the transmission part. We estimate the difference between the designed resonator frequency and real resonator frequency by the fabrication accuracy and the difference between the material properties shown in the Table 7.1 and the real material properties of the fabricated MKID. Based on the Table 6.4, the difference between calculated resonator frequency by the forester and measured that is 400 MHz. Considering the difference, we optimize the length of the transmission part when the resonant frequency included in the range of $4.4-7.6$ GHz. When the lengths of the transmission part are 1230 μm to 4050 μm for 145 GHz band and 1220 μm to 4030 μm for 220 GHz band, the resonance frequencies under the GroundBIRD atmospheric observation are within the readout frequency band. To reduce the LNA noise effect in NEP is to have a large deference between the BLIP noise and the optimized LNA noise in PSD. When $\eta_{\mathrm{opt}} = 0.39$ for 145 GHz band, $\eta_{\mathrm{opt}} = 0.30$ for 220 GHz band, PWV $= 3.8$ mm, $P_{\mathrm{read}} = -80$ dBm, and $T_N = 5$ K, we calculate the difference between the BLIP noise and the optimized LNA noise in various length of the transmission part shown in Figure 7.1. As a result, the deference between the BLIP noise increases with increasing the length of the transmission part. Since $l_{\mathrm{trans}} = 4050$ μm for 145 GHz and $l_{\mathrm{trans}} = 4030$ μm for 220 GHz are the largest

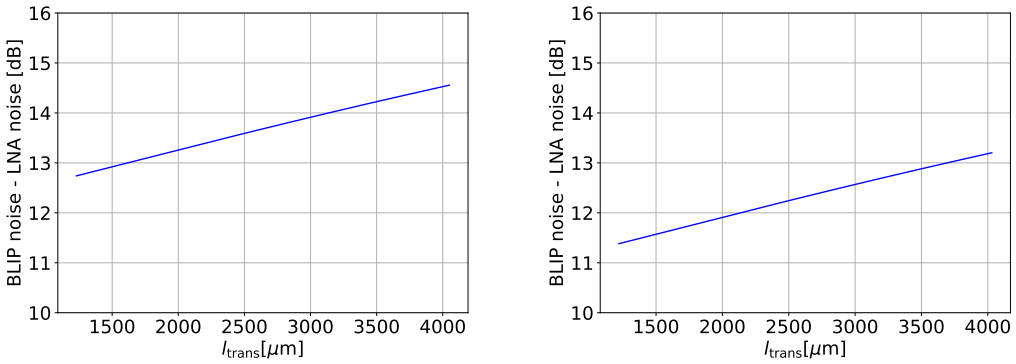

FIGURE 7.1: The difference between the BLIP noise and the LNA noise in various length of the transmission part for 145 GHz (left figure) and 220 GHz (right figure) band, respectively. The difference increase with increasing the length of the transmission part.

deference between the BLIP noise and the optimized LNA noise within the readout frequency band, we adopt this value for the new design.

As mentioned in the previous chapter, the main origin of the 1/f type noise in the phase PSD is the TLS noise of the transmission part and the TLS noise decreases with increasing the total width of the CPW line of the transmission part. However, there are two main trade off caused by the wider CPW line.

One is the magnetic vortex loss effect. It is known that the center strip of CPW line traps magnetic vortex, when high magnetic field is applied during superconducting transition. The vortex works as a excess resistance for complex conductivity [116]. The number of magnetic vortexes depends on the strength of the environmental magnetic field and the center strip width of the CPW line. However, the CPW line can not trap magnetic field under the threshold magnetic field which is perpendicular to the CPW line ($B_{\rm th}$) during the superconducting transition. The threshold magnetic field [117] is given by

$$B_{\rm th} = \frac{\pi \Phi_0}{4s^2}, \tag{7.2}$$

where s is the center strip width, and Φ_0 is the flux quantum given by

$$\Phi_0 = \frac{h}{2e} = 2.07 \times 10^{-15}\ [\mathrm{Tm}^2], \tag{7.3}$$

where e is the elementary charge and h is the Planck constant. We evaluate the effect of the ambient magnetic field around the focal plane of the GroundBIRD telescope. The geomagnetism at the GroundBIRD observational site is $\sim 30\ \mu$T. The GroundBIRD has a magnetic shield which reduce the external magnetic field below 1/100 [118, 97]. If the center strip width of the CPW line exceeds 70 μm, it may trap the vortex.

The other problem is radiation loss [119, 120]. If the phase velocity in the line exceeds the phase velocity in the substrate, the shock wave like a Cherenkov radiation is caused. The shock wave causes the loss in the MKID. The loss parameter α [119, 120] is given by

$$\alpha = \left(\frac{\pi}{2}\right)^5 2 \left(\frac{(1-\cos(\Psi)^2)^2}{\cos(\Psi)} \right) \frac{(s+2w)^2 \epsilon_{\rm sub}^{3/2}}{c^3 K(k') K(k)} f^3, \tag{7.4}$$

where $\epsilon_{\rm sub}$ is the relative permittivity of the substrate, $k = s/(s+w)$ (s: center strip width, w: center strip slot width), $k' = \sqrt{1-k^2}$, K is the complete elliptic integral, f is the readout frequency, c is the speed of light, and Ψ is the angle of the shock wave radiated in substrate given by

$$\cos(\Psi) = \frac{\sqrt{\epsilon'_{\rm eff}}}{\sqrt{\epsilon_{\rm sub}}}, \tag{7.5}$$

where $\epsilon'_{\rm eff}$ is the effective dielectric constant including the superconducting features given by

$$\epsilon'_{\rm eff} = c^2 L_{\rm tot} C_l, \tag{7.6}$$

where $L_{\rm tot}$ is the total inductance which is the summation of the kinetic inductance and the geometrical inductance, and C_l is the transmission capacitance per unit length. The quality factor of the radiation loss is given by

$$Q_{\rm rad} = \frac{\beta}{2\alpha}, \tag{7.7}$$

where β is $2\pi/\lambda$ (λ is the wavelength of the readout microwave signal). Since the loss parameter is proportional to the square of the total width of the CPW line, the quality factor of the radiation loss increases with increasing the total CPW line width. Including the quality factor of the radiation loss, the resonator quality factor Q_r is redefined by

$$\frac{1}{Q_r} = \frac{1}{Q_c} + \frac{1}{Q_i} + \frac{1}{Q_{\rm rad}}. \tag{7.8}$$

The noise level of the BLIP noise is proportional to square of $\mathrm{d}\theta/\mathrm{d}N_{\rm qp}$. The $\mathrm{d}\theta/\mathrm{d}N_{\rm qp}$ is proportional to the resonator quality factor as shown in Eq. 6.19. Therefore, the noise level of the BLIP noise is proportional to square of resonator quality factor. Therefore, the deference between the BLIP noise and the optimized LNA noise decreases with increasing the total CPW width of the transmission part due to the radiation loss.

We consider the trade off of the radiation loss to reduction of the TLS noise in the phase PSD. We include the radiation loss effect in the forecaster. Although these equations are not for the hybrid type MKID, we use these equations to pessimistically estimate the radiation loss by calculating that the same structure and materials are used as in the transmission part. In typical observation using MKID, the BLIP noise is over 10 dB higher than the LNA noise in the phase PSD. Since using common mode nose suppression which subtract readout noise using off resonance fluctuation, the noise level of the LNA noise becomes 3 dB higher than that without this method. Considering the effect, we optimize the total width of the CPW line of the transmission part within over 13 dB deference between the BLIP noise and the optimized LNA noise. When $\eta_{\rm opt} = 0.39$ for 145 GHz band, $\eta_{\rm opt} = 0.30$ for 220 GHz band, PWV $= 3.8$ mm, $P_{\rm read} = -80$ dBm, and $T_N = 5$ K, the relation between the center strip width and the deference between the BLIP noise and the optimized LNA noise is shown in Figure 7.2. In the calculation, the ratio of the center strip width of the transmission part to the slot width of the transmission part is fixed at a constant 3:2. The maximum center strip width (slot width) of the transmission part for 145 GHz and 220 GHz are 39 μm(15 μm) and 26 μm(10 μm), when the deference between the BLIP noise and the optimized LNA noise is over 13 dB. As a results, the

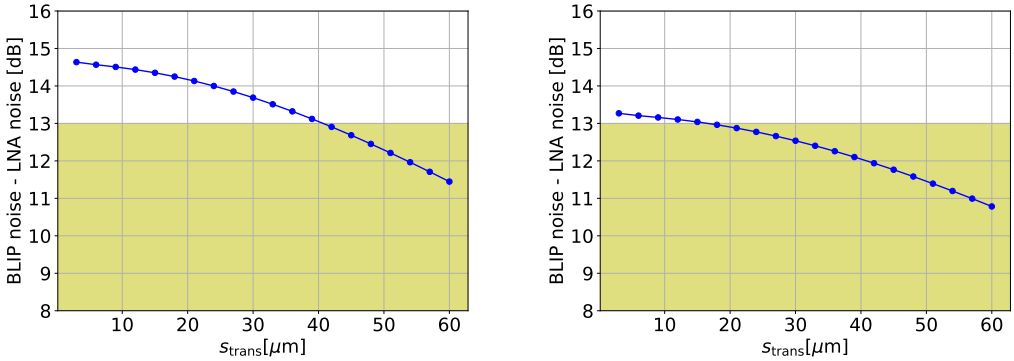

FIGURE 7.2: The difference between the BLIP noise and the optimized LNA noise in various center strip width of the transmission part. The ratio of the center strip width of the transmission part to the slot width of that is fixed at a constant 3:2 in the calculation for 145 GHz (left figure) and 220 GHz (right figure) band, respectively. The difference decreases with increasing the center strip width of the transmission part due to the radiation loss. The yellow region shows deference between the BLIP noise and the optimized LNA noise is less than 13 dB.

	Aluminum	Niobium
l	2300 μm	4050(4030) μm
s	2 μm	39(15) μm
w	2 μm	16(9) μm
d	0.05 μm	0.2 μm
d_g	/	0.2 μm

TABLE 7.2: The geometry of new MKID design. l is the length of the resonator for 145 GHz band (220 GHz band). s is the center strip width for 145 GHz band (220 GHz band). w is the slot width between the center strip and groundplane for 145 GHz band (220 GHz band). d and d_g are the thickness of the center strip and groundplane, respectively.

magnetic vortex effect is negligible for the new design in the GroundBIRD observation. We adopt these values for the geometry of new design MKID. Table 7.2 is the geometry of the new design MKID.

We adjust the coupling geometry to optimize the coupling quality factor. When $\eta_{\rm opt} = 0.39$ for 145 GHz band, $\eta_{\rm opt} = 0.30$ for 220 GHz band, PWV $= 3.8$ mm, the internal quality factors for 145 GHz band and 220 GHz band of the new design for the GroundBIRD atmospheric observation are 1.2×10^4 and 1.1×10^4, respectively. We calculate the geometry of the coupling to be $Q_i = Q_c$ using the public code "cpw_coupling" [111] as mentioned in the previous chapter. As a result, Table 7.3 shows the geometry of the coupling for 145 GHz band and 220 GHz band.

	145 GHz band	220 GHz band
l_c	430 μm	420 μm
s_c	39 μm	15 μm
w_c	26 μm	10 μm
v	3 μm	3 μm
s_t	10 μm	10 μm
w_t	6 μm	6 μm

TABLE 7.3: The geometry of coupling for new design for 145 GHz band and 220 GHz band. l_c is the coupling length. s_c is the coupling line width. w_c is the coupling slot width. v is the deference between the coupling and the feedline. s_t is the feedline strip width. w_t is the feedline slot width.

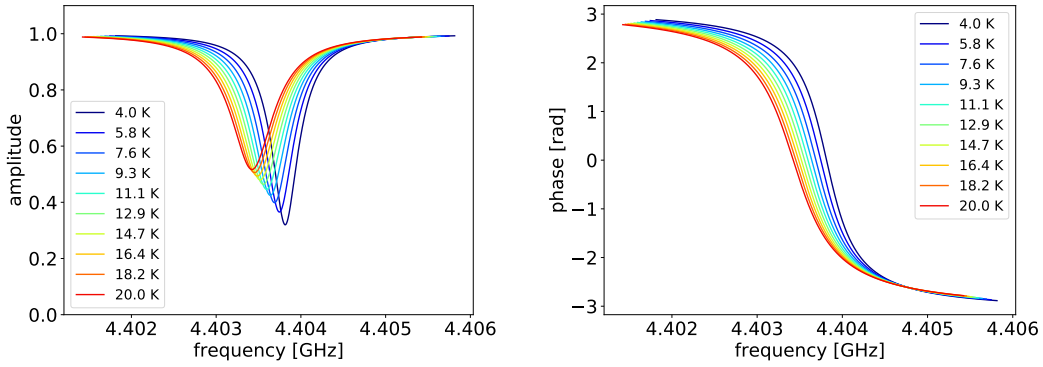

FIGURE 7.3: The amplitude (left figure) and the phase (right figure) of the complex transmission S_{21} for 145 GHz in the controllable blackbody observation for new design. The label shows the radiation temperature of the controllable blackbody. The label shows the blackbody temperature.

7.2 The new design performance forecast in measurement and observation

7.2.1 The measurement with balckbody source

We evaluate the performance of the new design in the controllable blackbody measurement as mentioned in the previous chapter using the forecaster. The amplitude and the phase of the complex transmission S_{21} of 145 GHz band and 220 GHz band in the controllable blackbody measurement are shown in Figure 7.3 and Figure 7.4, respectively, when $\eta_{\mathrm{opt}} = 0.5$. Since the resonance frequencies in any case are within the readout frequency range, the optimization of the length of the transmission part is no problem for the controllable blackbody measurement.

The each component of the phase NEP at 1 Hz and at 100 Hz for both of 145 GHz band and 220 GHz band in the controllable blackbody measurement are shown in Figure 7.5 and Figure 7.6, respectively. The TLS noise and the LNA noise are enough lower than the BLIP noise in the all radiation temperature condition. It is easy to evaluate the optical efficiency for the new design using the blackbody measurement.

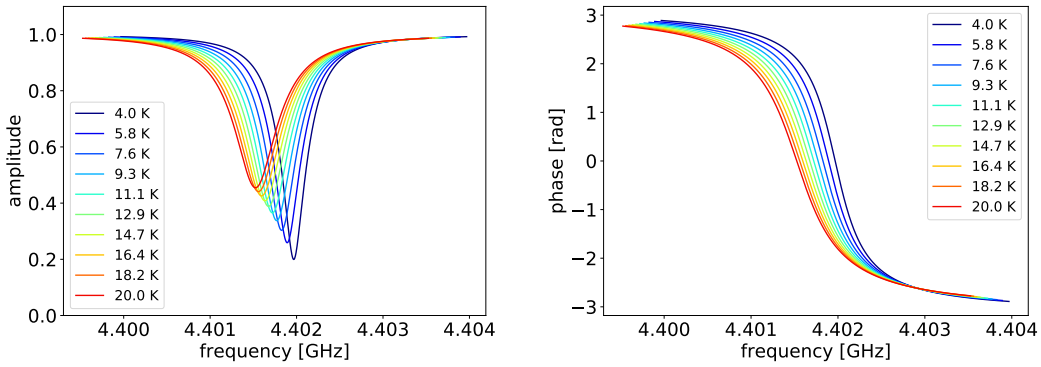

FIGURE 7.4: The amplitude (left figure) and the phase (right figure) of the complex transmission S_{21} for 220 GHz in the controllable blackbody observation for new design. The label shows the radiation temperature of the controllable blackbody. The label shows the blackbody temperature.

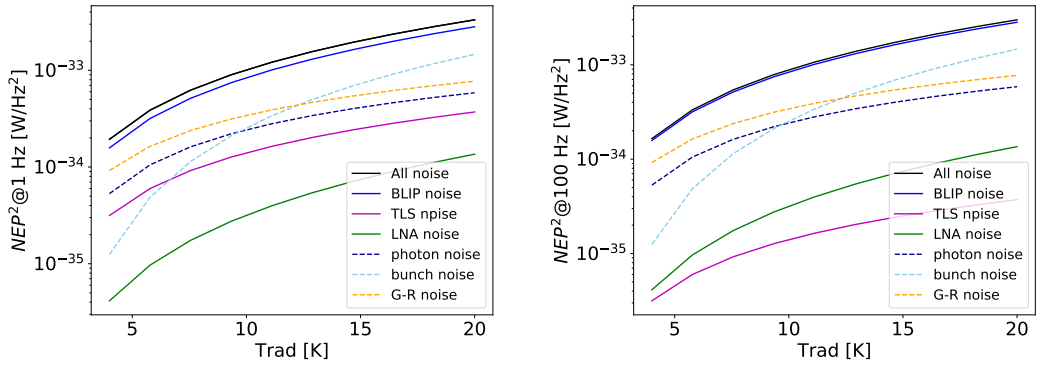

FIGURE 7.5: The each component and summation of the phase NEP at 1 Hz (left figure) and at 100 Hz (right figure) for new design of 145 GHz band in the controllable blackbody measurement. The black line shows the summation of NEP in the phase. The magenta, green, and blue solid lines show the TLS noise, the LNA noise, and the BLIP noise. The dark blue, cyan, and orange dashed lines show the photon, the photon bunch, and the G-R noise.

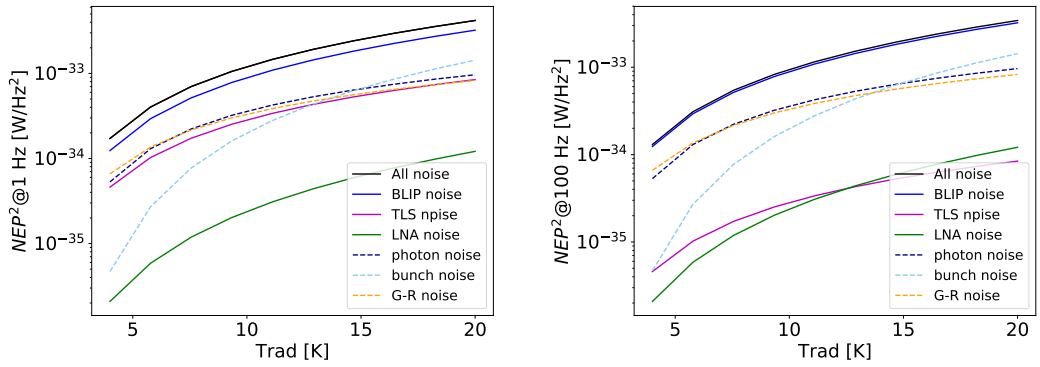

FIGURE 7.6: The each component and summation of the phase NEP at 1 Hz (left figure) and at 100 Hz (right figure) for new design of 220 GHz band in the controllable blackbody measurement. The black line shows the summation of NEP in the phase. The magenta, green, and blue solid lines show the TLS noise, the LNA noise, and the BLIP noise. The dark blue, cyan, and orange dashed lines show the photon, the photon bunch, and the G-R noise.

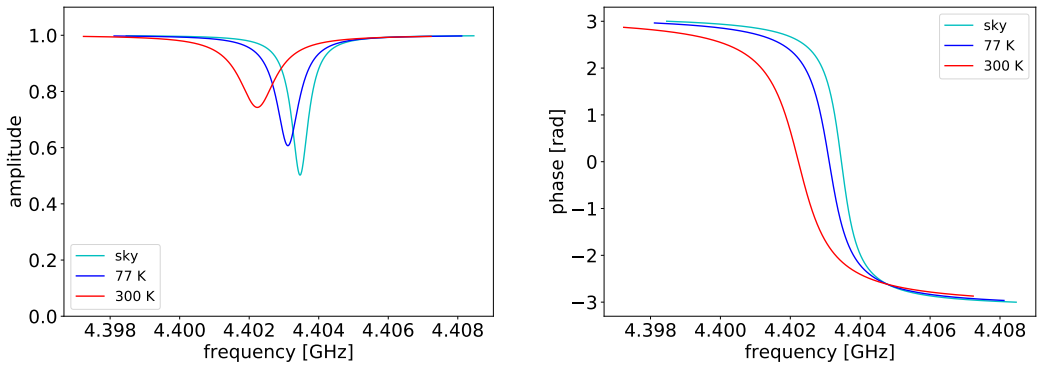

FIGURE 7.7: The amplitude (left figure) and the phase (right figure) of the complex transmission S_{21} as a function of readout frequency for new design of 145 GHz band in atmospheric (PWV = 3.8 mm, cyan solid line), LN2 (blue solid line), and 300 K (red solid line) radiation.

7.2.2 The forecast of the GroundBIRD observation for new design

We evaluate the new design performance for the GroundBIRD observation using the forecaster. When $\eta_{\rm opt} = 0.39$ for 145 GHz band, $\eta_{\rm opt} = 0.30$ for 220 GHz band, PWV = 3.8 mm, $P_{\rm read} = -80$ dBm, and $T_N = 5$ K, the amplitude and the phase of the complex transmission S_{21} for new design of 145 GHz band and 220 GHz band in atmospheric, LN2, and 300 K observation are shown in Figure 7.7 and Figure 7.8, respectively. The PSD in the atmospheric observation for new design 145 GHz band and for 220 GHz band are shown in Figure 7.9 and Figure 7.10, respectively.

The resonance shape is suitable because of $Q_i = Q_c$ in the atmospheric observation. Since the resonance frequencies in any case are within the readout frequency range, the optimization of the length of the transmission part is no problem for the GroundBIRD observation. The LNA noise is lower than the BLIP noise both of the frequency band in the phase PSD. The $1/f$ type noise is less than the BLIP noise at the GroundBIRD rotational speed (0.3 Hz). It concludes that the new design meets the requirements of GroundBIRD observation.

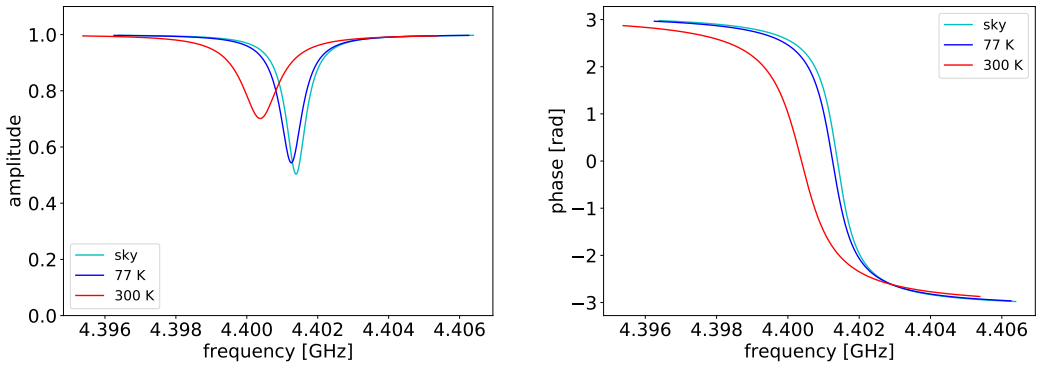

FIGURE 7.8: The amplitude (left figure) and the phase (right figure) of the complex transmission S_{21} as a function of readout frequency for new design of 220 GHz band in atmospheric (PWV = 3.8 mm, cyan solid line), LN2 (blue solid line), and 300 K (red solid line) radiation.

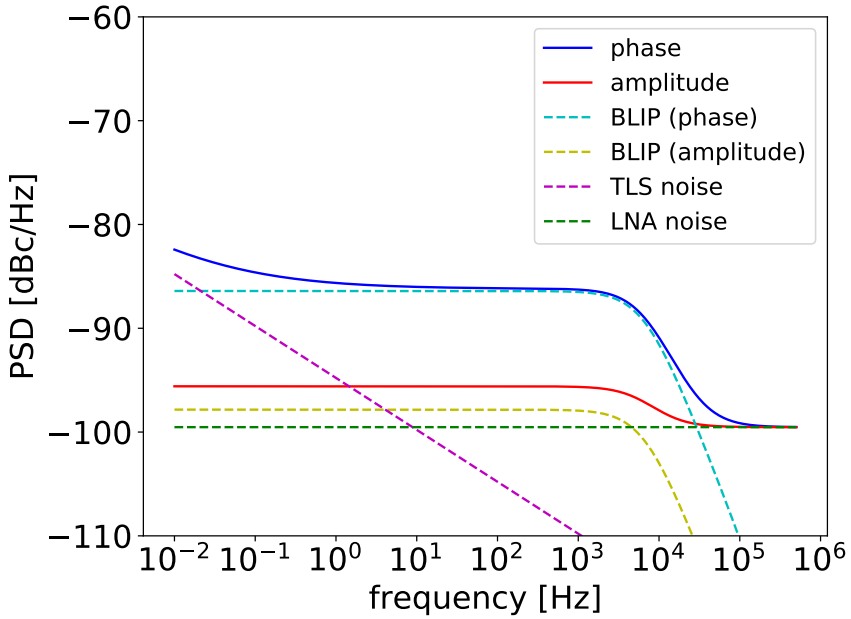

FIGURE 7.9: The each component of PSD (TLS noise, BLIP noise and LNA noise) and sum of the PSD for new design of 145 GHz band in atmospheric (PWV = 3.8 mm) observation. The red and blue lines show the summation of the PSD in the amplitude and the phase. The magenta, green, yellow, and cyan dashed line show the TLS noise, the LNA noise, the amplitude of the BLIP noise, and the phase of that, respectively.

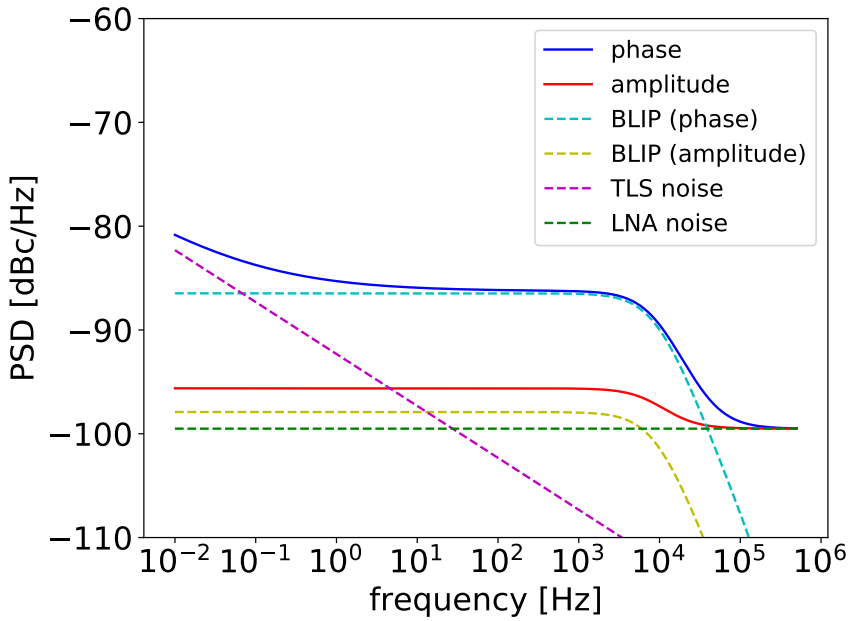

FIGURE 7.10: The each component of PSD (TLS noise, BLIP noise and LNA noise) and sum of the PSD for new design of 220 GHz band in atmospheric (PWV = 3.8 mm) observation. The red and blue lines show the summation of the PSD in the amplitude and the phase. The magenta, green, yellow, and cyan dashed line show the TLS noise, the LNA noise, the amplitude of the BLIP noise, and the phase of that, respectively.

7.3 Discussion and Conclusion

In order to solve problems of prototype design as mentioned in the previous chapter, we propose new MKID geometry for the GroundBIRD observation. The feature of the design is to select suitable Q_c value under the atmospheric observation and to use wider CPW line of the transmission part, small volume of the absorb part, and long length of the transmission part to reduce the $1/f$ type noise less below the BLIP noise at the GroundBIRD rotational speed (0.3 Hz). The trade off problems of using wide CPW line are vortex effect and radiation effect. We include the radiation loss effect in the forecaster and we optimize the geometry to the extent that radiation loss is negligible. And we also check that the magnetic vortex effect is also negligible for the magnetic field environment of the GroudBIRD. We forecast the performance of the new design in the controllable blackbody measurement and GroundBIRD observation. As a results, the performance of new design for the GroundBIRD observation meets the observational requirements of the GroundBIRD.

We include radiation loss effect in the forecaster, however the equations of the radiation loss are not for the hybrid type MKID. For the future plan, we would like to develop the equations of the radiation loss for hybrid type MKID, since we can forecast the more realistic performance of the MKID.

Chapter 8

Impact of our works on the GroundBIRD experiment

We invented the novel method to calibrate the responsivity of MKID [75, 65] based on the creation of the quasiparticles by the readout microwave signal [71, 72, 73, 74, 57] as shown in Chapter 4. Since the GroundBIRD needs cooling cycle everyday, the responsvity of MKID must be calibrated every cooling cycle for the precise observation. The conventional method consumes 2 hours for the calibration. The calibration of the responsivity should be performed when the atmospheric or instrumental conditions are changed. The reduction of the time duration for the responsivity calibration down to 10 minutes contributes to significant maximization of the data acquisition. Further, the conventional method accompanies the systematic uncertainty whether the device temperature is same as the temperature measured by the thermometer. Since our proposed method is free from this kind of systematic uncertainty, our method contributes to improve the accuracy of the obtained data by the GroundBIRD.

We invented the novel measurement method of the superconducting transition temperature (T_c) [65] of the MKID as shown in Chapter 5. Since there was no method to measure T_c for the hybrid type MKID, the cited values of T_c varies largely from $T_c = 1.1$ to 1.5 K for an aluminum. This results in 20% uncertainty of the NEP for the optical bright condition at the GroundBIRD observation site. This method have opened a channel to measure the superconducting transition temperature of the hybrid type MKID at the first time. Since the value of the T_c controls the performance of the MKID, our method dramatically reduces the uncertainty of the performance of the MKID at the time of the design. Therefore, our method contributes to fabricate the MKID optimized to the GroundBIRD experiment and to extract the maximum performance of the GroundBIRD experiment.

In spite of the development of the MKID more than the past five years by the Japanese GroundBIRD team, yet the MKID applicable to the GroundBIRD observation has not been completed. On the other hand, the high performance hybrid type MKIDs applicable to the astronomical observations have been already developed in Netherlands and US. Number of knowledge of the development of the hybrid type MKID have been reported in many papers in the course of these developments. To accelerate the research and development cycle of hybrid type MKID optimized to the GroundBIRD experiment, we have developed the performance forecaster of hybrid type MKID by summarizing the knowledge of the development of the hybrid type MKID obtained by the previous studies as shown in Chapter 6. It allows to forecast the sensitivity of the hybrid type MKID by just inputting the design and observational condition parameters. With this tool, the main cause which degrades the performance of the hybrid type MKID developed by the Japanese team is identified. We are able to propose new design of the hybrid type MKID optimized to

the GroundBIRD observation by improving the defect with the tool. Although the actual performance is not clear until the performance verification of the newly designed hybrid type MKID will be done, it is very confident that the hybrid type MKID fabricated with the proposed design may have enough performance to proceed GroundBIRD experiment since we identified the defect of the former design and improved it. The fabrication of the hybrid type MKID based on the new design is underway as the collaborative work with Netherlands Institute for Space Research (SRON). The fabrication and the performance verification experiment are going to be completed until the end of March 2021. After April 2021, we may able to start the observation with enough sensitivity for the CMB observations at the first time. Therefore, we can say that the development of the forecaster plays a crucial role to proceed the GroundBIRD experiment.

Chapter 9

Conclusion and Future plan

We invented the novel method to calibrate the responsivity of MKID [75, 65] based on the previous studies [71, 72, 73, 74, 57]. For the precision observation, the responsvity of MKID must be calibrated every cooling cycle. Conventionally, the MKID responsivity has been calibrated by changing the device temperature using heater. However, this method is inevitable from following systematic error. It always accompanies uncertainties whether the plate temperature measured by the thermometer coincides with the detector temperature. This method is also time consuming. The invention of the novel calibration method of the MKID responsivity was highly demanded. Since the microwave readout power signal through MKID deposits the energy in the resonator and creates quasiparticles, we can observe the time evolution of the number of quasiparticles by changing microwave power from high power to low power abruptly and can extract the time constant of the resonator. We can evaluate the number of quasiparticles by comparing the measured time constant with the theoretical formula. By using these results, the responsivity is able to be measured. The results obtained by applying our method are compared with the result obtained by the conventional methods [70], [71]. We confirmed that our method reproduces the previously reported results reasonably well. We suppose that a little differences of the results obtained by these two methods are mainly coming from the uncertainty of the device temperature in the conventional method, the uncertainty of the PSD method due to the difficulty of inclusion of the TLS noise precisely, and the uncertainty of the superconducting transition temperature. Since our method is free from the above mentioned systematic accompanying in the conventional method, our method provides much more secure results compared with the conventional method. Further, time duration consumed for the calibration is dramatically shortened, down to 10 minutes, by applying our calibration method. For the GroundBIRD observation, the available time for observational becomes 1.5 times longer when the responsivity calibration method is changed to the proposed method from the conventional method. Since the time constant extracted from the roll off appeared in the frequency dependence of PSD provides the most secure value, it is important to compare the time constant obtained by our method with that extracted from the roll off appeared in PSD for checking the accuracy of our method. Unfortunately the noise level of the prototype MKID is too bad to extract the time constant from the measured PSD. This test should be done in future with better performance MKID. This method also opens a possibility for evaluating degradation of the performance of the MKID due to the excess quasiparticles generated by the readout microwave signal [73].

We invented the novel measurement method of the superconducting transition temperature (T_c) [65] of the MKID. The superconducting transition temperature T_c of the MKID is an important parameter for both fixing design and evaluating performance. However, there is no method which is able to measure the superconducting

transition temperature of the hybrid type MKID directly. By extrapolating the results of the relation between the phase response of the MKID and quasiparticle lifetime when the microwave power is changed rapidly, we can obtain the intrinsic quasiparticle lifetime which is not biased by the excess quasiparticles generated by the readout microwaves input. The intrinsic quasiparticle lifetime is theoretically modeled by T_c, the physical temperature of the device, and other known parameters. We can extract T_c by comparing the measured lifetime with theoretical model [79, 80]. Using an aluminum MKID, we checked the validity of this method. The results are consistent with those obtained by T_c measured by monitoring the transmittance of the readout microwaves while changing the device temperature. This method have opened a channel to measure the superconducting transition temperature of the hybrid type MKID directly. We evaluate the systematic uncertainty of T_c in various observation. For the GroundBIRD observation the uncertainty of T_c causes 20% uncertainty of the NEP. For the CMB satellite mission using MKID, the T_c causes 10% uncertainty of the NEP. For the dark condition, the uncertainty of T_c causes tenfold uncertainty of the NEP. Moreover, since we evaluate some parameters, e.g. optical efficiency, and responsivity using equation included in T_c, the uncertainty of T_c causes the uncertainty of the such parameters.

We show that the performance of the prototype MKID is far from the GroundBIRD observation requirements based on the results of our performance verification experiments. The $1/f$ type TLS noise dominates over the generation and recombination noise below 100 Hz. To mitigate the $1/f$ atmospheric fluctuation by the rapid rotation scan strategy of the GroundBIRD, the TLS noise must be suppressed not to be dominant above 0.3 Hz.

To accelerate the research and development cycle of MKID, we have developed the performance forecaster of MKID. The reliability of the forecaster has been checked by comparing the extracted results with the results of the performance measurement for the prototype GroundBIRD MKID and with the results reported in Ref. [110]. By inputting the design parameters of the prototype GroundBIRD MKID into the forecaster, we confirmed that the TLS noise dominates over the generation and recombination noise below 100 Hz and that the main problem of the prototype MKID is its design. Since the total width of the CPW made from Nb of the prototype MKID is too narrow, the contribution of the TLS noise became prominent. A new design of MKID with widening the total center strip width of the CPW made from Nb is proposed. Enlarging the center strip width of CPW line results in the increase of number of trapped vortex [117] and the increase of the resistance loss due to the trapped vortex. Further, energy loss due to the Cherenkov type radiation emitted from the CPW line [120, 119] is increased. We include the radiation loss effect in the forecaster. We optimize the total center strip width in the range of negligible of the radiation loss. We also checked the magnetic vortex effect is also negligible for the magnetic field environment of the GroundBIRD. The noise behavior of the new design is checked by using the forecaster. We showed that the TLS noise is significantly reduced from that of the prototype MKID and is suppressed below the BLIP noise down to 0.3 Hz.

More detailed comparison between the results from the forecaster and our measurement results is necessary for future work. Based on the real measurement results, we have a plan to feed back to the model improvement. In addition, based on these studies, we fabricate new design MKID for the GroundBRID observations for the future plan. We developed Graphical User Interface tool of the MKID performance forecaster. In the tool, when we input the material parameters, geometry, and measurement condition, the expected MKID performance is outputted. We plan to

develop the tool available on the web for everyone to use for the future.

We mentioned temperature, readout power, and geometry dependence for TLS noise in this thesis. The TLS noise also has a superconducting material dependence [91, 94]. The TLS noise exist at an oxide of the substrate and the metal interface. In order to suppress the effect, the nitride metal, e.g. NbTiN [91] and TiN [94] is advantage. MKID group in SRON and TUDelft develop high quality NbTiN film [91, 92] and use it for MKID. The TLS noise level of NbTiN film is 11 dB lower than that of Nb film studied by J. Gao *et al*.[88]. We start the development of NbTiN-Al hybrid type MKID for the GroundBIRD telescope with them.

The other issue for the ground-based observation using MKID with wide frequency band is the noise from low noise amplifier. When the thermal noise of the low noise amplifier is lower, the range of optimization of the design is wide. In the superconducting quantum computer, the Josephson Parametric Amplifier (JPA) whose noise level achieves quantum noise limit is widely used [121]. The noise level of JPA is $\sim$ 10 dB less than the commercial low nose amplifier which we use. However, the dynamic range of readout power for JPA (< -100 dBm) is lower than the MKID operation readout power (> -100 dBm) and the bandwidth is narrow (< 1 GHz). In recent, the kinetic inductance traveling wave parametric amplifier (KIT) [122] is the cutting-edge superconducting amplifier for superconducting quantum computer and astronomical observation using MKID. It has a wide dynamic range (< -40 dBm) and wide band width (~ 4 GHz). Previous studies shows the noise level reduces almost quantum noise limit. For the future, precise astronomical observation using MKID, the development of these amplifier will be important topic.

Appendix A

Big Bang model

A.1 Homogeneous and isotropic universe

It is known that the universe is the homogeneous and isotropic in the large scale. It is called the cosmological principle. A number of observations, not just the CMB observations, have proved that the cosmological principle is suitable approximation. In 1920s, the metric satisfying with the principle is proposed. It is called Friedmann-Lemaître-Robertson-Walker (FLRW) metric given by

$$ds^2 = -c^2dt^2 + a^2(t)\left[\frac{\mathrm{d}r^2}{1-Kr^2} + r^2(\mathrm{d}\theta^2 + \sin^2\theta \mathrm{d}\phi^2)\right] \tag{A.1}$$

where c is the speed of light, a is the scale factor which represents the cosmological expansion, K is the curvature of space ($K = 0$: the flat universe, $K < 0$: the closed universe, and $K > 0$: the open universe). The relation between the stress-energy tensor and the metric tensor which is called Einstein equation, is given by

$$G^{\mu}_{\nu} = \frac{8\pi G}{c^4} T^{\mu}_{\nu}. \tag{A.2}$$

In a zero-order approximation, the material distribution in the universe is homogeneous. For the perfect fluid, the stress-energy tensor is given by

$$T^{\mu}_{\nu} = \begin{pmatrix} -\rho c^2 & 0 & 0 & 0 \\ 0 & p & 0 & 0 \\ 0 & 0 & 0 & p \end{pmatrix}, \tag{A.3}$$

where ρ and p are the mass density and pressure, respectively. Using Eq. (A.2), two equation which represents evaluation of the homogeneous universe in zero-order approximation which is called Friedman equation is given by

$$\left(\frac{\dot{a}}{a}\right)^2 = \frac{8\pi G}{3}\rho - \frac{c^2 K}{a^2} \tag{A.4}$$

and,

$$\frac{\ddot{a}}{a} = -\frac{4\pi G}{3}\left(\rho + 3\frac{p}{c^2}\right). \tag{A.5}$$

Using the two equation and eliminating $\ddot{a}$, the equation corresponding the energy conservation law of adiabatic change is given by

$$\dot{\rho} + 3\frac{\dot{a}}{a}\left(\rho + \frac{p}{c^2}\right) = 0. \tag{A.6}$$

	state density parameter ω	mass density ρ
non relativistic matter	0	a^{-3}
relativistic matter	1/3	a^{-4}
cosmological constant	-1	const

TABLE A.1: The state density parameter and energy density

We define the relation between the stress and the mass density given by

$$p = \omega \rho c^2, \tag{A.7}$$

where ω is state density parameter summarized in Table A.1. In the Friedman equation, $\omega < -1/3$ means the universe expansion. In general, the material has no negative pressure. Therefore the universe has deceleration expansion. However, Einstein considered the scale of the universe was not changed. In order to cancel the declaration expansion he introduced cosmological constant in the Einstein equation given by

$$G^{\mu}_{\nu} + \Lambda \delta^{\mu}_{\nu} = \frac{8\pi G}{c^4} T^{\mu}_{\nu}. \tag{A.8}$$

where Λ is the cosmological constant. Using the modified Einstein equation, the Friedman equation in the cosmological constant is rewritten by

$$\left(\frac{\dot{a}}{a}\right)^2 = \frac{8\pi G}{3}\rho - \frac{c^2 K}{a^2} + \frac{c^2 \Lambda}{3} = \frac{8\pi G}{3}\left(\rho + \frac{\Lambda c^2}{8\pi G}\right) - \frac{c^2 K}{a^2}, \tag{A.9}$$

and

$$\frac{\ddot{a}}{a} = -\frac{4\pi G}{3}\left(\rho + \frac{3p}{c^2}\right) + \frac{c^2 \Lambda}{3} = -\frac{4\pi G}{3}\left(\rho + 3\frac{p}{c^2}\right) + \frac{4\pi G}{3}\left(\frac{\Lambda c^2}{4\pi G}\right). \tag{A.10}$$

In the Friedman equation, the cosmological constant represents as the expansion of the universe. Using Eq. (A.9) and (A.10), the density and the pressure of the cosmological constant are given by

$$\rho_{\Lambda} = \frac{\Lambda c^2}{8\pi G}, \tag{A.11}$$

and

$$p_{\Lambda} = -\frac{\Lambda c^4}{8\pi G}. \tag{A.12}$$

It is consistent for $\omega = -1$ in the Eq. (A.7).

Edwin Hubble denied the existence of the cosmological constant and the static universe which Einstein proposed observing the redshift of the galaxies. However, observational results of the supernova expansions in the distant universe suggests the accelerated expansion of the universe [123, 124]. In order to describe the expansion universe, the cosmological constant is needed. It is know that the material for expanding the universe is called the dark energy. The state density parameter ω is less than $-1/3$ for the accelerated expansion of the universe. It means the dark energy has $\omega < -1/3$. The results of the Planck satellite also suggested the existence of the dark energy [4]. We consider the origin of the accelerated expansion of the universe as the dark energy.

A.2 Cosmological parameter

When each component's energy conservation laws are independent, using Eq. (A.7), the relation between the density and the scale factor is given by

$$\rho \propto a^{-3(1+\omega)}. \tag{A.13}$$

The current ($t = t_0$) Hubble parameter which is the expansion rate of our universe is given by

$$H_0 = \left(\frac{\dot{a}}{a}\right)_{t=t_0}. \tag{A.14}$$

Using Eq. (A.9), the current Hubble constant is given by

$$H_0^2 = \frac{8\pi G}{3}\rho_0 - c^2 K, \tag{A.15}$$

where ρ_0 is the current density and we used the current scale factor $a_0 = 1$. In the case of the flat universe ($K = 0$), the current density is given by

$$\rho_{\mathrm{cr},0} = \frac{3H_0^2}{8\pi G}. \tag{A.16}$$

where $\rho_{\mathrm{cr},0}$ is called the critical density. When the critical density is same as a total density, the curvature of the universe is flat. The density parameter which represents the component of the density divided by the critical density is given by

$$\Omega_{A0} = \frac{\rho_{A0}}{\rho_{cr,0}} = \frac{8\pi G\rho_{A0}}{3H_0^2} \tag{A.17}$$

where $A = r$ (radiation), m (material), K (curvature), and λ (cosmological constant). Using the relation, Eq. (A.9) is rewritten by

$$\left(\frac{\dot{a}}{a}\right)^2 = H_0^2\left(\frac{\Omega_{r0}}{a^4} + \frac{\Omega_{m0}}{a^3} + \frac{\Omega_{K0}}{a^2} + \Omega_{\Lambda 0}\right), \tag{A.18}$$

where the density parameter of the curvature is given by

$$\Omega_{K0} = -\frac{c^2 K}{H_0^2}. \tag{A.19}$$

In the current universe the material density is more than the radiation one. As the past universe, the material density is the same as the radiation one. The era is called the energy equality. Before the energy equality, the universe is the radiation dominant. In current, the universe is dark energy dominant.

A.3 Inflationary cosmology

The Big Bang theory explained a various astronomical observation results. However, the theory is expected to cause an unnatural initial state in the early universe e.g. the horizon problem and the flatness problem. In 1980s, Alan Guth and Katsuhiko Sato proposed the inflationary cosmology [7, 8]. Assuming the universe had a exponentially expanding period at the very beginning of the universe, they showed that these problems are naturally solved.

A.3.1 Horizon problem

The era of CMB photon emission is 370 k years from the beginning of the universe. The era is called the last scattering surface. At the last scattering surface, the apparent angular size of the particle horizon is $\sim$ 2 deg[1]. However, the fluctuation of CMB temperature with larger than a few degree are found (COBE/DIRBE, WMAP, Planck reference). Why the coherent structures are imprinted in the CMB temperature fluctuation exceeding the particle horizon is the horizon problem.

A.3.2 Flatness problem

It is observationally confirmed that the curvature of the current universe is close to zero, in other word the geometry of the current universe is close to flat[5, 6]. The most updated Planck result is $\Omega_{K0} = 0.0007 \pm 0.0019$ [4]. Using the Friedman equation (A.18), $\Omega_K \propto a^{-2}H^{-2}$ in early universe, where a is the scale factor and H is the Hubble constant at the time. The relation between the curvature of current universe and that of the past universe is given by

$$\Omega_K = \frac{H_0^2}{H^2}\frac{\Omega_{K0}}{a^2} = \left(\frac{\dot{a}_0}{\dot{a}}\Omega_{K0}\right)^2. \tag{A.20}$$

Since $\dot{a}$ is increasing as going back the time in the standard Big Bang theory, the right hand of Eq. (A.20) is decreasing as going back the time. In the era of the radiation dominant ($a \propto t^{1/2}$), the relation between scale factor and time is given by

$$\left(\frac{\dot{a}_0}{\dot{a}}\right) = \left(\frac{t}{t_0}\right)^2 = \left(\frac{a}{a_0}\right)^2. \tag{A.21}$$

Since the adiabatic condition that the production of the CMB temperature and the scale factor is constant is applicable with good accuracy from the begging of the universe to the current universe, the density parameter of the curvature at the Planck time ($t_{pl} \sim 5.39 \times 10^{-44}$ sec) is given by

$$\Omega_K(t_{pl}) \sim \left(\frac{k_B T_0}{m_p c^2}\right)\Omega_{K0} \sim 10^{-62}\Omega_{K0}, \tag{A.22}$$

where $m_{pl}c^2 = \sqrt{\hbar c/G} = 1.2 \times 10^{19}$ GeV is the Planck mass. Since $\Omega_{K0} \sim 0$, the curvature of the universe at the begging of the universe must be tuned to a value close to zero with an accuracy of more than 62 orders. This fine tuning problem is called the flatness problem.

A.3.3 Cosmic inflation

The flatness and horizon problems are solved if the universe has the acceleration expansion period in the early epoch. The inflation theory predicts that the universe has a nearly exponentially expanding period at the very early epoch. This period is called inflationary period. During the inflationary period, $\dot{a}$ is decreasing function with going back time. Therefore, the fine tuning problem of the initial density parameter of the universe is relaxed and the flatness problem is able to be solved. During the inflationary period, the radius of the current observable universe shrinks exponentially as going back time. Therefore, the even particle horizon of the current universe was contracted to very small scale and less than the particle horizon at

the time. This provides the solution to the horizon problem since all the structures within the current particle horizon was once contained in the causally contactable scale.

The model proposed that the nearly exponential expansion during the inflationary period is realized by the vacuum energy of the scalar field ϕ called "Inflaton". When the effective potential of the Inflaton field is $V(\phi)$, the action of the inflaton field is given by

$$I = \int \sqrt{-g}\mathrm{d}^4x \left[-\frac{1}{2} g^{\mu\nu} \partial_\mu \phi \partial_\nu \phi - V(\phi) \right], \tag{A.23}$$

where g is the determinant of the metric tensor given by $g = \det(g_{\mu\nu})$ and the adopted the metric in the local inertial frame is $\eta_{\mu\nu} = (-1, 1, 1, 1)$. In zeroth order, the action is reduced to

$$I = \int \mathrm{d}^4x a^3 \left[\frac{\dot{\phi}^2}{2c^2} - V(\phi) \right], \tag{A.24}$$

where homogeneous, isotropic and spatially flat are assumed to the zeroth order universe. Using Euler–Lagrange equation, the equation of the motion of scalar field is given by

$$\ddot{\phi} + 3H\dot{\phi} + c^2 V'(\phi) = 0, \tag{A.25}$$

where $\dot{\phi} = \mathrm{d}\phi/\mathrm{d}t$ and $V' = \mathrm{d}V/\mathrm{d}\phi$. The energy density of the Inflaton field is given by

$$\rho_\phi c^2 = \frac{\dot{\phi}}{2c^2} + V(\phi). \tag{A.26}$$

Using Noether's theorem, the pressure of the Inflaton field is given by

$$p_\phi = \frac{\dot{\phi}^2}{2c^2} - V(\phi). \tag{A.27}$$

When $\dot{\phi}^2/c^2 \ll V(\phi)$, the equation of state is reduced to $p_\phi = -\rho_\phi c^2$ that is equivalent to the cosmological constant. Using $\rho_\phi = V/c^2$ and solving the Friedman equation as the Inflaton dominant, the expansion law scale is given by

$$a = C\exp(Ht), \tag{A.28}$$

where the Hubble constant is given by

$$H = \sqrt{\frac{8\pi G V(\phi)}{3c^2}}. \tag{A.29}$$

The era of inflationary period is that the universe is exponential expanding by the vacuum energy from the Inflaton field. It is known that the scale of universe is expanded $\sim 10^{30}$ times in $\sim 10^{-34}$ s.

A.3.4 The slow-roll inflation

The slow-roll inflationary model is one of the standard inflationary model. In the model, the scalar field ϕ moves to the minimum value of the inflationary potential in the Inflaton potential V while keeping $|\dot{\phi}|^2 \ll c^2 V$ as shown in Figure A.1. As a result, nearly exponential expansion is realized. When the scalar field fall down to the minimum value of the inflaton potential, the era of inflation is finished and the difference between the potential energy is released as latent heat of the vacuum and all species of the particles such as photon, dark matter particles, baryons and

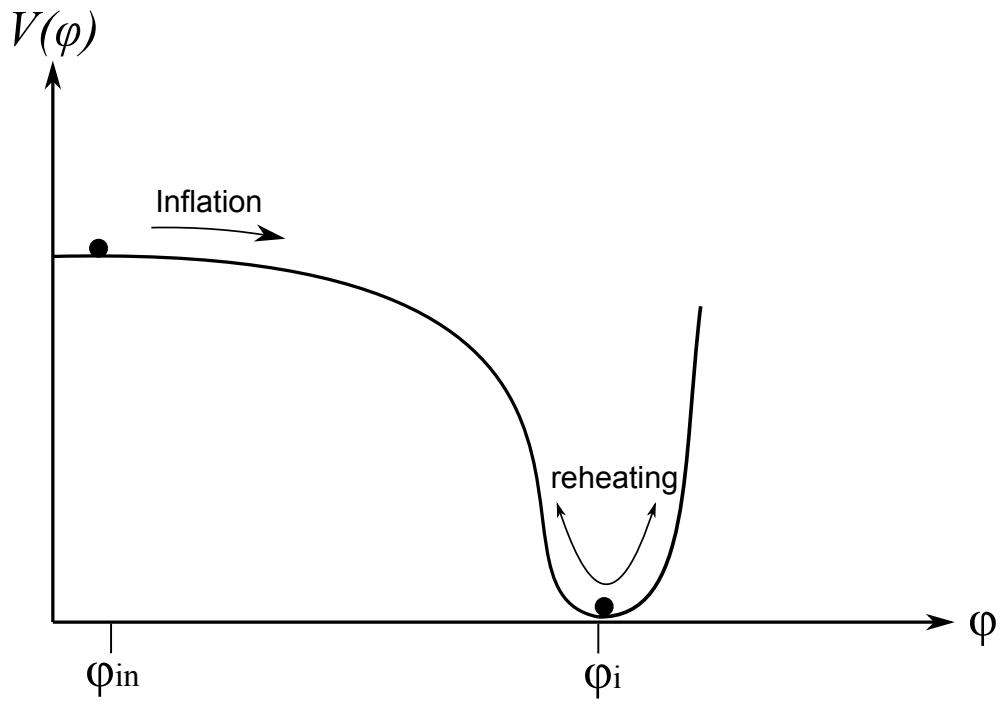

FIGURE A.1: The potential of the scalar field. The exponential expansion occurs at $\phi_{\rm in}$. After the expansion, reheating occurs.

leptons etc. The era is called reheating period. In order to maintain $\dot{\phi}^2 \ll c^2 V$, the acceleration of the scalar field must be also sufficiently small. The first term of the left hand side of equation (A.25) is compared with other two terms. The equation is reduced to

$$\dot{\phi} \sim -\frac{c^2}{3H} V'(\phi). \tag{A.30}$$

Also, in the case of $\dot{\phi}^2 \ll c^2 V$, the Hubble constant is also approximated as

$$H \sim \sqrt{\frac{8\pi G V(\phi)}{3c^2}}. \tag{A.31}$$

We introduce two parameters as slow roll parameters defined as

$$\epsilon \equiv \frac{c^4}{16\pi G}\left(\frac{V'}{V}\right)^2, \tag{A.32}$$

and

$$\eta \equiv \frac{c^4}{8\pi G}\frac{V''}{V}. \tag{A.33}$$

The ratio of kinetic energy of the scalar field to its potential is described by the slaw roll parameter as

$$\frac{\frac{1}{2c^2}\dot{\phi}^2}{V} \sim \frac{1}{2}\frac{1}{V}\frac{V'^2}{9H^2} \sim \frac{1}{3}\frac{c^4}{16\pi G}\left(\frac{V'}{V}\right)^2 = \frac{1}{3}\epsilon. \tag{A.34}$$

Time derivative of square of the Hubble constant is given as

$$2H\dot{H} \sim \frac{8\pi G}{3c^2} V'\dot{\phi}. \tag{A.35}$$

Dividing this equation by H^3 and using Eq. (A.30), we get

$$\frac{\dot{H}}{H^2} = -\frac{4\pi G}{3c^2}\frac{c^2 V'^2}{3H^4} \sim -\epsilon. \tag{A.36}$$

From the time derivative of Eq. (A.30), we get

$$3H\ddot{\phi} + 3\dot{H}\dot{\phi} = -V''\dot{\phi}c^2. \tag{A.37}$$

The ratio between the first term and the second term of Eq. (A.25) is given by

$$\frac{\ddot{\phi}}{3H\dot{\phi}} \sim -\frac{c^2 V''}{9H^2} - \frac{\dot{H}}{3H^2} \sim -\frac{1}{3}\frac{c^4 V''}{8\pi G V} + \frac{1}{3}\epsilon = \frac{1}{3}(-\eta + \epsilon). \tag{A.38}$$

Therefore in order to realize the slow roll inflation, $\epsilon \ll 1$ and $|\eta| \ll 1$ are required.

A.3.5 Physical essence of the realization of scalar and tensor perturbation due to quantum fluctuation during the inflation period

Any inhomogeneity existing before the inflation are erased due to the exponential expanding during the inflation. Pair creation and annihilation of particle and antiparticle always happen in the nature due to quantum fluctuation of the vacuum. The life time of the pair created particles of energy of E till annihilation, Δt, is estimated from the uncertainty principle as

$$\Delta t \sim \frac{\hbar}{E}. \tag{A.39}$$

In the time scale of the normal life in the present universe, these effect does not have any observable effect. In the standard inflation model, it is assumed that the inflaton field is described by real scalar field. Therefore, antiparticle of inflaton is inlfaton itself. Since the tensor mode of the metric perturbation is also real field, antiparticle of graviton is also graviton itself. Since the event horizon of c/H exists during the inflation period, the separation of the pair created particles which have life time of longer than the Hubble time, exceeds the event horizon that is

$$c\Delta t > \frac{c}{H}. \tag{A.40}$$

This pair created particles misses the chance to encounter and to annihilate. These remain in the universe. Since the quantum fluctuation of the vacuum is random process, distribution of the realized particles is inhomogeneous. This is the origin of the scalar and tensor perturbation. These considerations lead that the typical energy scale of the fluctuation of the inflaton field and graviton is both $E \sim \hbar H$.

A.3.6 The scalar perturbation of the metric

For simplicity, reheating happens suddenly when the vacuum expectation value of the inflaton field reaches the valley of the inflaton potential shown in Figure A.1. Let's consider the region accompanying the inflaton field fluctuation of $\delta\phi$. Assume the amplitude is positive. The reheating of the region happens prior to the average region where accompanies no fluctuation. The difference of the reheating time of the

region prior to the average universe is given by

$$\delta t_{\rm reh} = -\frac{\delta\phi}{\dot{\phi}}, \tag{A.41}$$

where $\delta t_{\rm reh} < 0$. Under abrupt reheating assumption, dominant component of the energy density of the universe switch to inflaton potential to energy of the relativistic particles. Before reheating the expansion law of the region is nearly exponential expansion. After reheating the expansion law of the region abruptly changes to $t^{1/2}$. Therefore, the change of the radius of the universe of the already reheated region during $-\delta t_{\rm reh}$ which gives the time duration till the reheating of the average region is happened after the reheating the region is happened, is negligible compare with the change of the radius of the universe of the average universe, that is $\Delta a = \dot{a}(-\delta_{\rm reh})$. In other word, the radius of the universe of the already reheated region is smaller than the average region amount of $-\Delta a$. This results in the perturbation of the scalar curvature of the region as

$$\varphi \sim \frac{-\Delta a}{a} = \frac{\dot{a}\delta t_{\rm reh}}{a} = -\frac{H\delta\phi}{\dot{\phi}}. \tag{A.42}$$

Therefore, the power spectrum of the scalar curvature perturbation is given by the power spectrum of the inflaton perturbation as

$$P_s(k) = \left(\frac{H}{\dot{\phi}}\right)^2 P_\phi(k) = \left(\frac{H}{\dot{\phi}}\right)^2 \left(\frac{H}{2\pi}\right)^2_{k=aH}, \tag{A.43}$$

where we use $P_\phi = (H/2\pi)^2/2k^3$, k is comoving wave number of the perturbation and subscript $k = aH/c$ defines the Hubble constant when the perturbation with wavelength of a/k exits the event horizon $1/H$. Note that the natural unit is adopted in this discussion. The following definition of the power spectrum of variable X is applied;

$$< X_{\vec{k}} X_{\vec{k}'} > \equiv (2\pi^2)\delta^3(\vec{k} - \vec{k}')\frac{P_X(k)}{k^3}. \tag{A.44}$$

Using

$$\left(\frac{H}{\dot{\phi}}\right)^2 \sim \frac{9H^4}{c^4 V'^2} = 4\pi G \frac{16\pi G V^2}{c^4 V'^2} = 4\pi G \frac{1}{\epsilon}, \tag{A.45}$$

the power spectrum of scalar curvature is given by

$$P_s(k) = \frac{4\pi G}{\epsilon}\left(\frac{H}{2\pi}\right)^2_{k=aH}. \tag{A.46}$$

It predicts that the scalar curvature perturbation is almost scale invariant.

Equation (A.46) says that amplitude of power spectrum of scalar perturbation for some wave number is given by the Hubble constant at the time of horizon exit of the perturbation. In the slow roll inflation model, the value of the Hubble constant during the inflation that is the value of the inflaton potential, is monotonically decreasing with time as shown in Figure A.1. Further, the larger the wave number of the perturbation exits the event horizon later. Therefore the power spectrum of scalar curvature decreases with increasing wave number. Suppose the horizon exit time of the perturbation with wave number of $k + \delta k$ delays δt from the horizon exit time of the perturbation with k. Using $k = aH$, the wave number deference is

rewritten as

$$\mathrm{d}k \sim (\dot{a}H + a\dot{H})dt \sim \dot{a}dtH = -aH^2\frac{d\phi}{\dot{\phi}} = -kH\frac{d\phi}{\dot{\phi}}. \tag{A.47}$$

Therefore,

$$\frac{\mathrm{d}}{\mathrm{d}\ln k} = \frac{k\mathrm{d}}{\mathrm{d}k} \sim -\frac{\dot{\phi}}{H}\frac{\mathrm{d}}{\mathrm{d}\phi} \sim -\frac{c^4}{8\pi G}\frac{V'}{V}\frac{\mathrm{d}}{\mathrm{d}\phi}. \tag{A.48}$$

and

$$\frac{\mathrm{d}\epsilon}{\mathrm{d}\ln k} = -\frac{1}{2}\frac{1}{(8\pi G)^2}\frac{V'}{V}\left(\frac{2V'V''}{V^2} = \frac{2V'^2}{V^2}\right) = -2\eta\epsilon + 4\epsilon^2, \tag{A.49}$$

is obtained. The power index of the power spectrum of the scalar curvature perturbation is deduced as

$$\frac{\mathrm{d}\ln P_s(k)}{\mathrm{d}\ln k} = 2\eta - 6\epsilon. \tag{A.50}$$

The power spectrum of the density fluctuation is defined as

$$< \delta\rho_k^2 > \propto k^{n_s}. \tag{A.51}$$

Poisson equation $\nabla^2\Phi \propto \delta\rho_k$ provides $\Phi \propto k^{-2}\delta\rho_k$. Therefore,

$$\int \mathrm{d}\ln k P_s(k) \propto \int k^2\mathrm{d}k|\Phi_k|^2 \propto \int \mathrm{d}k k^{-2}|\delta\rho_k|^2 \propto \int \mathrm{d}\ln k k^{n_s-1}. \tag{A.52}$$

Therefore, the power spectral index of the scalar curvature is given by $n_s - 1$ and

$$n_s - 1 = 2\eta - 6\epsilon. \tag{A.53}$$

When $\epsilon = 0$ and $\eta = 0$, the scale invariant so-called Harison-Zel'dovich spectrum of $n_s = 1$ is recovered. The most updated Planck results [4] shows that the spectral index of the scalar perturbation is

$$n_s = 0.9649 \pm 0.0042. \tag{A.54}$$

A.3.7 The tensor perturbation

The power spectrum of the tensor perturbation is given by

$$P_t(t) = 64\pi G\left(\frac{H}{2\pi}\right)^2_{k=aH}. \tag{A.55}$$

The spectral index is given by

$$n_t = \frac{\mathrm{d}\ln(P_t)}{\mathrm{d}\ln k} \sim -2\epsilon. \tag{A.56}$$

A.3.8 The tensor-to-scalar ratio

The ratio of the power spectrum of the scalar perturbation and the power spectrum of the tensor perturbation is called tensor-to-scalar ratio r. The tensor-to-scalar ratio is defined as

$$r = \frac{P_t(k)}{P_s(k)} = 16\epsilon. \tag{A.57}$$

The relation between the potential V and tensor-to-scalar ratio is given by

$$V^{1/4} = 1.06 \times 10^{16} \times \left(\frac{r}{0.01}\right)^{1/4} \text{ GeV}. \tag{A.58}$$

When we know the tensor-to-scalar ratio by the observations, we can estimate the energy scale at the inflation era. It is known that the energy scale is close to that of the grand unified theory (GUT) scale. The current lower limit of the tensor-to-scalar ratio is $r < 0.07$ (95%, C.L.)[12]. From eq.(A.57), the lower limit on r provides the lower limit of ϵ as $\epsilon < 0.04375$. By combining with Planck results Eq.(A.54) and eq.(A.53), we get $\eta < -0.00465$. The inflaton potential model with negative η is favored more than one sigma significance.

A.4 Cosmic Microwave Background

If there is the cosmic inflation at the beginning of our universe, the primordial gravitational waves are generated. This should make specific polarization pattern in the CMB polarization map. It is called B-mode polarization. The detection of CMB B-mode polarization is supposed to be smoking gun evidence to confirm inflation.

In order to measure the tensor-to-scalar ratio r, the CMB polarization observation is the most promising approach today [9]. The primordial gravitation waves originated from the quantum fluctuation of the space time metric during inflation imprints the odd parity polarization pattern to the CMB called "B-mode" polarization.

A.4.1 The brief history of CMB observations

Arno Penzias and Robert Wilson observed the CMB for the first time using 20 feet horn antenna at the Crawford Hill location of Bell Telephone Laboratories in 1964 [125].

In 1989, the COBE (Cosmic Background Explorer) satellite measured the CMB monopole power spectrum using the spectroscope named FIRAS (Far Infrared Absolute Spectroscopy). The CMB monopole spectrum meets 2.725 K blackbody spectrum shown in Figure A.2 [126, 127, 128]. The DMR (Differential Microwave Radiometer) on COBE probed that there is 10^{-5} temperature fluctuation with respect to the CMB temperature. It is known that the fluctuation is the origin of the large scale structure of the universe.

A.4.2 CMB polarization

Before the clear up of the universe, the proton and electron moved separately. The photon is scattered by the electron which is called Thomson scattering. Since the electron captured by proton in the last scattering state, the photon was not scattered by the electron.

In the redshift $z \sim 20$, the photon was re-scattered by the electron created by the UV radiation from the first stars. The era is called reionization. The expected power spectrum of the B-mode polarization has the bump affected by the reionization at angular scale $l < 10$.

In the observational results (COBE/DMR, WMAP, Plnack), the CMB has a temperature fluctuation. Therefore the CMB has a polarization. The photon scattered by the electron create perpendicular polarization at the line of site. When the universe

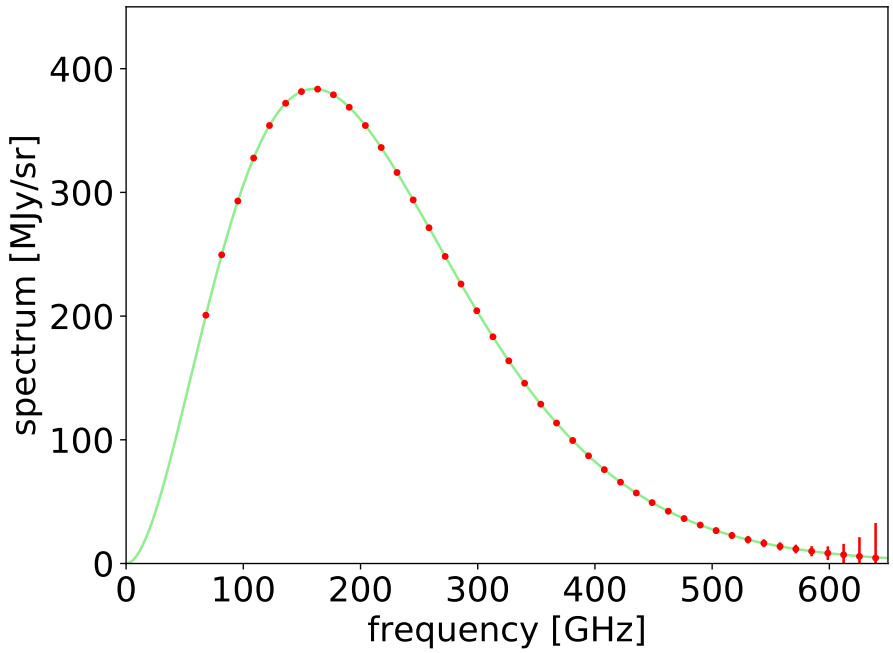

FIGURE A.2: The CMB spectrum with 100σ error bars as a function of frequency measured by the COBE/FIRAS. The green line shows 2.725 K blackbody spectrum. The data is available from [129]

is isotropic, the polarization is canceled out by the various direction polarization whose intensity is same. Otherwise, when the universe has a quadrupole distribution, the polarization is not canceled out, and it remains the polarization along the line of hot region shown in Figure A.3. Because the polarization from hot region (low energy density region) is higher than that from cold region (high energy density region). When the polarization are overlapped, the angle of polarization from hot region remains.

A.4.3 Stokes parameter

We define electrical fields E_x and E_y ($E_x \perp E_y$). The phase difference of the fields is defined δ. The Stokes parameters is given by

$$I = E_x^2 + E_y^2, \tag{A.59}$$

$$Q = E_x^2 - E_y^2, \tag{A.60}$$

$$U = E_x E_y \cos\delta, \tag{A.61}$$

and

$$V = E_x E_y \sin\delta, \tag{A.62}$$

where I is the intensity, Q is the intensity deference of x and y direction, U is the intensity difference of x and y direction inclined by 45 degrees, and V is the intensity deference of right and left circular polarization. It is known that the circular polarization of CMB polarization is too weak. The stokes parameter V is negligible for CMB polarization observation. The CMB intensity is proportional to the fourth

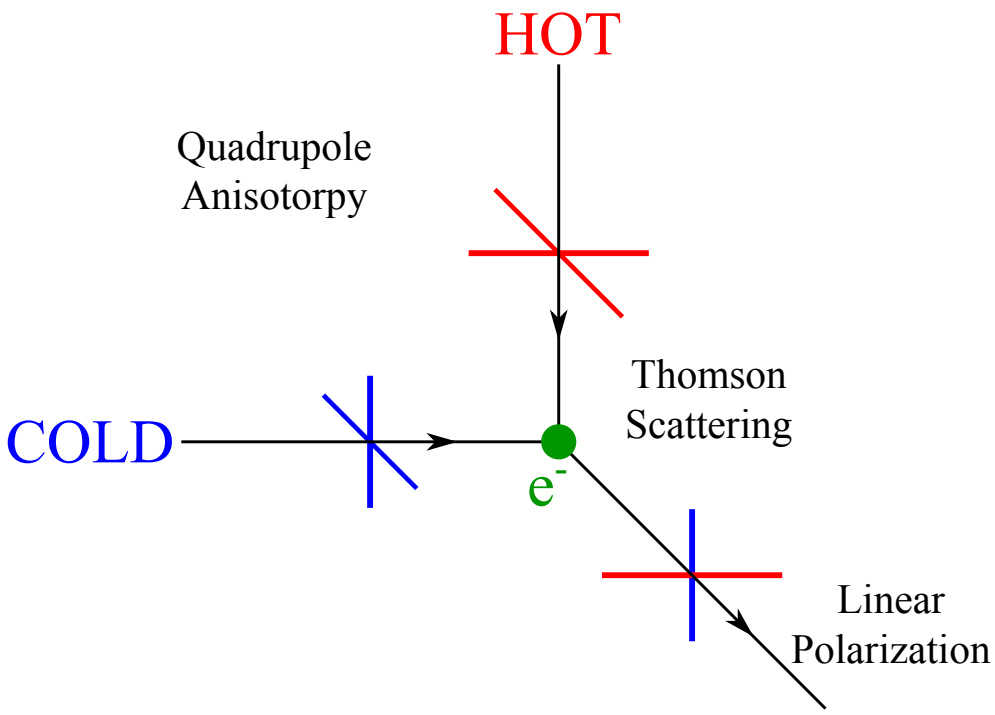

FIGURE A.3: The CMB polarization from the quadrupole anisotorpy. The photon scattered by the electron. When the quadrupole anisotoropy, the polarization is created aligned to the hot region.

power of CMB temperature ($\delta T/T = \delta I/4I$). Similarly, we define the dimensionless stokes parameters Q' and U' as the stokes parameters Q and U divided by $4I$ given by

$$Q' = \frac{Q}{4I}, \tag{A.63}$$

and

$$U' = \frac{U}{4I}. \tag{A.64}$$

A.4.4 *E*-mode and *B*-mode polarization

The dimensionless stokes parameters Q' and U' is defined by the coordinate of the observer. Using wave number vector, the parameters is changed to an observer independent parameters. We define $\bar{Q}(\vec{l})$ and $\bar{U}(\vec{l})$ as making Q' and U' Fourier transform, respectively. Using two dimensional wave number vector ($\vec{l}$), we change the coordinate given by

$$\begin{pmatrix} E(\vec{l}) \\ B(\vec{l}) \end{pmatrix} = \begin{pmatrix} \cos 2\phi_l & \sin 2\phi_l \\ -\sin 2\phi_l & \cos 2\phi_l \end{pmatrix} \begin{pmatrix} \bar{Q}(\vec{l}) \\ \bar{U}(\vec{l}) \end{pmatrix}, \tag{A.65}$$

where ϕ is the angle between two dimensional wave number vector and $\bar{Q}$, $\bar{U}$. $E(\vec{l})$ and $B(\vec{l})$ are called *E*-mode polarization and *B*-mode polarization respectively. *E*-mode polarization is parallel or perpendicular to the wave number vector in the real space. *B*-mode is 45 deg or 135 deg tilted to the wave number vector in the real space. The power spectrum of the *E*-mode and *B*-mode polarization are given by

$$< E^*(\vec{l})E(\vec{l'}) >= (2\pi)^2\delta^2(\vec{l}-\vec{l'})C_l^{EE}, \tag{A.66}$$

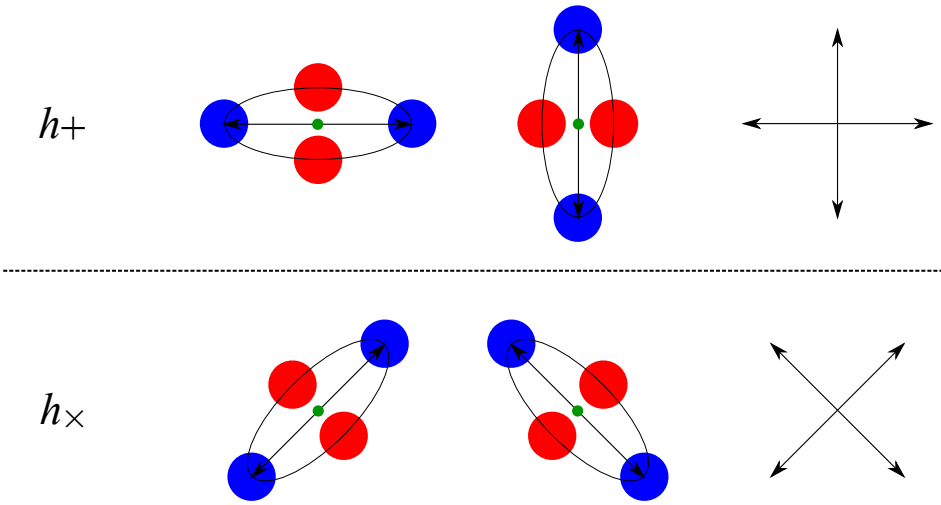

FIGURE A.4: The polarization from the primordial gravitational waves. The primordial gravitational wave stretched the space and create CMB polarization by the Thomson scattering. The blue and red region are cold and hot region, respectively. The h_+ polarization creates E-mode polarization. The $h_\times$ mode creates B-mode polarization.

and

$$< B^*(\vec{l})B(\vec{l'}) >= (2\pi)^2\delta^2(\vec{l}-\vec{l'})C_l^{BB}, \tag{A.67}$$

respectively.

To observe B-mode polarization is the direct proof of the inflationary cosmology. The cosmology predicts the existence of the primordial gravitational waves. The wave causes the fluctuation to the space component of the metric tensor (g_{ij}). The metric tensor is given by

$$g_{ij}(\vec{x},t) = \bar{g}_{ij}(\vec{x},t) + \delta g_{ij}(\vec{x},t), \tag{A.68}$$

where $\delta g_{ij}(\vec{x},t)$ is given by

$$\delta g_{ij}(\vec{x},t) = \begin{pmatrix} \Phi & 0 & 0 \\ 0 & \Phi & 0 \\ 0 & 0 & \Phi \end{pmatrix} + a^2 \begin{pmatrix} 0 & 0 & h_1 \\ 0 & 0 & h_2 \\ h_1 & h_2 & 0 \end{pmatrix} + a^2 \begin{pmatrix} h_+ & h\times & 0 \\ h_\times & -h_+ & 0 \\ 0 & 0 & 0 \end{pmatrix}, \tag{A.69}$$

where the first term of the right hand is scalar perturbation, the second term of that is vector perturbation, and third term of that is tensor perturbation. Φ is the gravitational potential and h_+, $h_\times$ shown in Figure A.4 is the metric tensor caused by the primordial gravitational waves. When the gravitational waves penetrate the last scattering surface, the space is stretched. It causes quadruple distribution and CMB polarization. h_+-mode causes E-mode polarization, however it is not identified that the polarization is caused by the temperature perturbation or primordial gravitational waves. $h_\times$-mode causes B-mode polarization. The polarization is not created by the temperature perturbation. Therefore, to observe B-mode polarization is direct proof of the inflationary cosmology shown in Figure A.5).

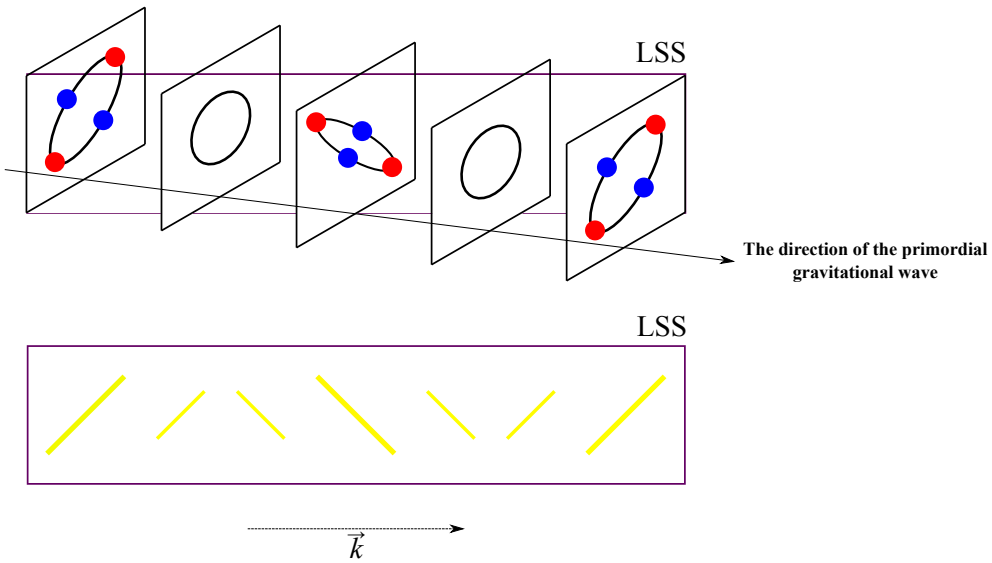

FIGURE A.5: The gravitational wave propagate the last scattering surface (top figure). The CMB polarization at the last scattering surface (bottom figure). The $\vec{k}$ is the vector of the wave number.

Appendix B

Superconducting photon detectors

B.1 Transition Edge Sensor

A transition edge sensor (TES) [23] shown in Figure B.1 is a superconducting detector. The detector is widely used for millimeter, submillimeter astronomical observation. And the detector is also used dark matter search experiment and have a plan to be used for the X-ray satellite observation. The combination of the detector and SQUID (superconducting quantum interference device) amplifier can be multiplexed. This makes a large focal plane detector. The superconducting absorber of TES is maintained the slightly below transition temperature. An incoming photon is changed the resistance of the TES dramatically. When the TES is connected to the bias voltage source, we can measure the incoming light power by the current change.

B.2 Superconducting Tunnel Junction

A superconducting tunnel junction (STJ) [130, 131] shown in Figure B.2 is a superconducting detector. The detector used Josephson effect as a detection mechanism. It consists of a superconducting-normal-superconducting junction. The radiation breaks Cooper pairs and generates quasiparticles. The radiation power is estimated by the Josephson current which is quasiparticles tunneled very thin insulator film. The detectors are being developed for submillimeter and optical/UV and X r-ray observation. Same mechanism is used in the superconducting mixer for millimeter and submillimeter astronomical observations.

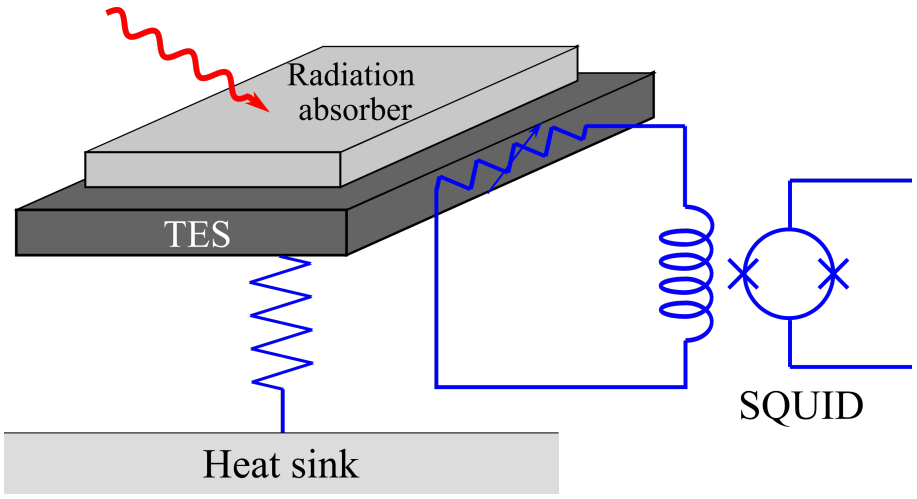

FIGURE B.1: The illustration of Transition Edge Sensor (TES).

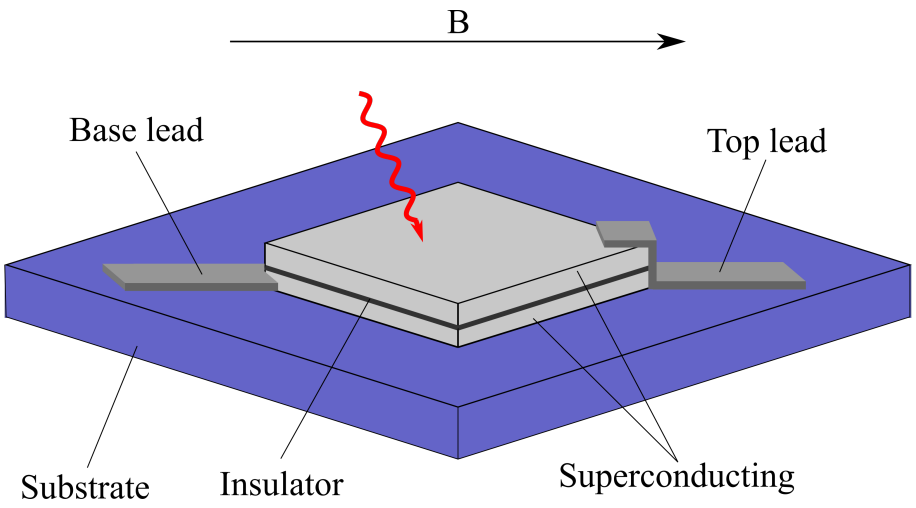

FIGURE B.2: The illustration of Superconducting Tunnel Junction (STJ).

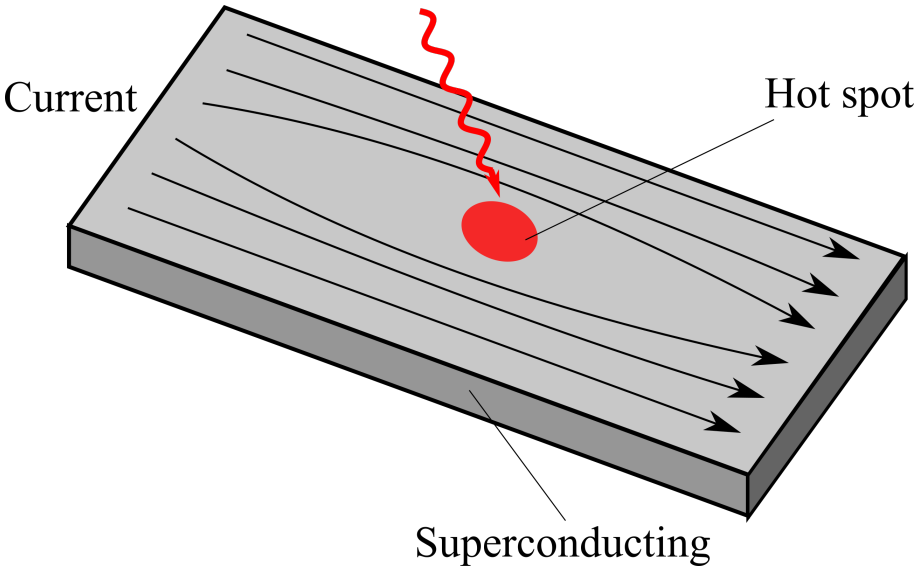

FIGURE B.3: The illustration of Superconducting Nanowire Single-Photon Detector (SNSPD).

B.3 Superconducting Nanowire Single-Photon Detector

A superconducting nanowire single-photon detector (SNSPD) [132, 133] shown in Figure B.3 is a type of near-infrared and optical single-photon detector. It based on current-biased superconducting nanowire. It was developed at Moscow State Pedagogical University and the University of Rochester in 2001. In 2018, the SNSPD is the fastest single-photon detector for photon counting measurement. The SNSPD consists of a thin and narrow superconducting nanowire whose length is typically hundreds micrometers. The detector is maintained below superconducting transition temperature and biased DC current which is slightly below critical current. The incoming photon breakers Cooper-pairs and reduces the local critical current and creates non-superconducting region. The incoming photon energy is measured by the voltage change.

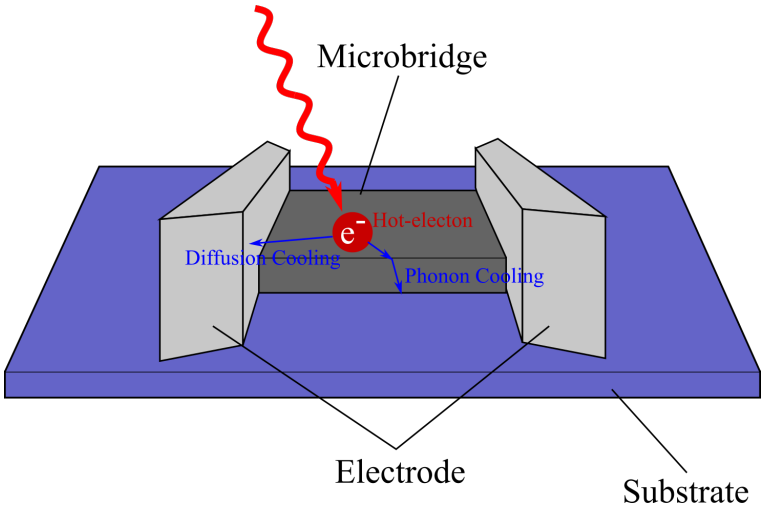

FIGURE B.4: The illustration of Hot Electron Bolometer (HEB).

B.4 Hot Electron Bolometer

A hot electron bolometer [134] shown in Figure B.4 is a type of semiconductor or superconducting direct detector. The electrons in the metal is coupled with phonon included in substrate in low temperature. When the detector is absorbed radiation, the electrons is decoupled phonon. The decoupled electron in the metal is called "hot electron". When the resistance is depend on the temperature of the electrons, we can use this mechanism as a bolometer.

B.5 Metallic Magnetic Calorimeter

A metallic magnetic calorimeter (MMC) [135] shown in B.5 is based on the measurement for the change of magnetization of superconducting metal. The change is proportional to the temperature change caused by the absorption of the radiation. We measure this change by SQUID.

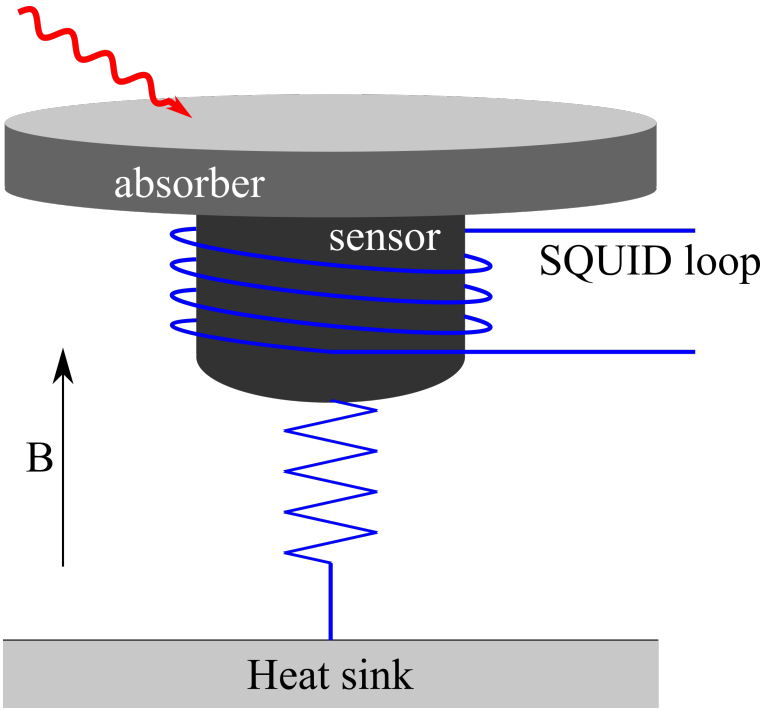

FIGURE B.5: The illustration of Metallic Magnetic Calorimeter (MMC).

Appendix C

Calibration for GroundBIRD telescope

C.1 The elevation scan

The elevation scan is to calibrate detector responsivity, because the radiation power from the sky is changed by the thickness of atmosphere. The minimum elevation angle of the GroundBIRD telescope is 60 deg. The radiation temperature of the elevation scan is given by

$$T_{\mathrm{sky,elevation}} = \frac{T_{\mathrm{sky}}}{\cos(90 - \theta_{\mathrm{elevation}})} \tag{C.1}$$

where $\theta_{\mathrm{elevation}}$ is the telescope elevation and T_{sky} is the radiation temperature from the sky at $\theta_{\mathrm{elevation}} = 90$ deg. The sky temperature as a function of elevation angle for 145 and 220 GHz is in Figure C.1.

C.2 The moon observation

The moon is the good calibration source for the millimeter telescope [136]. To observe the moon is useful to calibrate the responsivity of the detector, the polarization of the detector and the beam of the telescope. The moon polarization is distributed radially from the center. We can use this polarization for the polarization calibration. The radiation temperature of the moon is $\sim$ 200 K. The moon centered map simulation for the GroundBIRD 20 RPM observation for 145 and 220 GHz is in Figure C.2 and C.3. The parameter of the simulation is in tab. C.1. The center temperature for the moon observation is 67 K for 145 GHz and 110 K for 220 GHz. The maximum and minimum polarization temperature difference is $\pm$0.4 K for 145 GHz and $\pm$1.3 K for 220 GHz.

Radiation temperature	200 K
Reflection index	1.8
The moon radius	0.25 deg
Angular resolution	0.60 deg(0.42 deg)

TABLE C.1: The parameter of the moon observation simulation for 145 GHz(220 GHz) [136, 54]

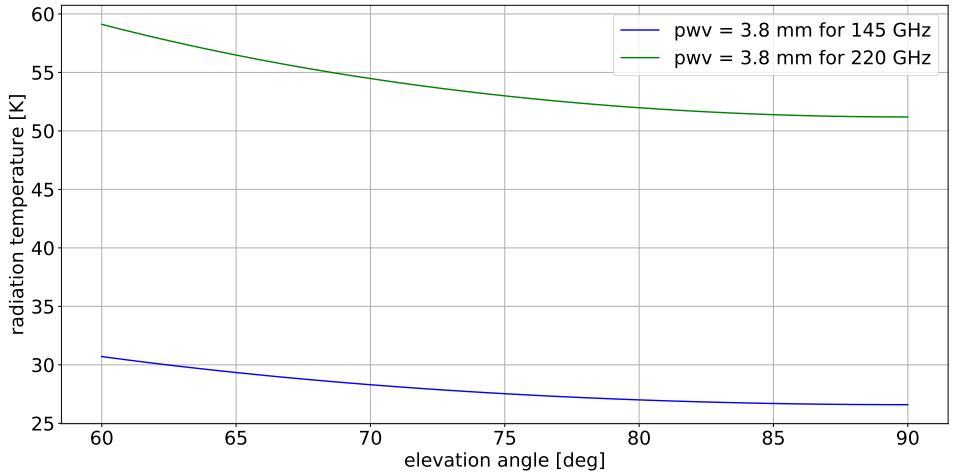

FIGURE C.1: The sky radiation temperature as a function of elevation angle with PWV = 3.8 mm

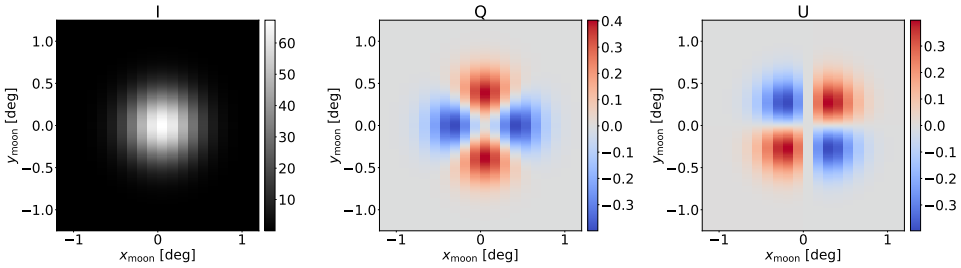

FIGURE C.2: The moon observation simulation for 145 GHz with 20 RPM. The left, center, and right shows the Stokes parameter I, Q, and U of the moon signal.

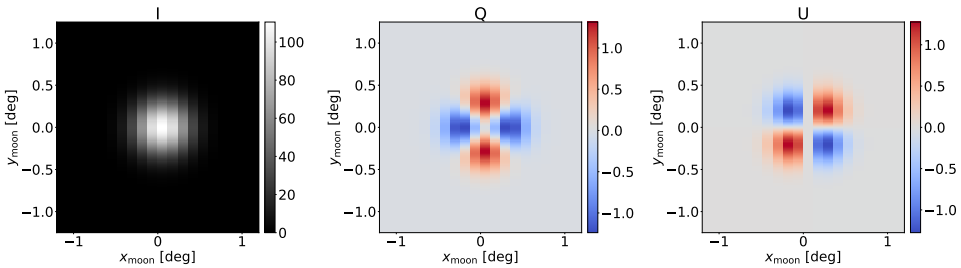

FIGURE C.3: The moon observation simulation for 220 GHz with 20 RPM. The left, center, and right shows the Stokes parameter I, Q, and U of the moon signal.

C.3 The blackbody radiation measurement

The method that the telescope window is covered by the blackbody radiation source is one of the most common calibration method for radio astronomical observation. We usually use commercial blackbody source called "AN-72". It is ideal blackbody source. When the ambient temperature is 300 K, the absorbed power from the blackbody source is given by

$$P_{\mathrm{abs-hot,145\ GHz}} = 80\eta_{\mathrm{opt}}\ \mathrm{pW}\ (\text{for } 145\ \mathrm{GHz}), \tag{C.2}$$

and

$$P_{\mathrm{abs-hot,220\ GHz}} = 101\eta_{\mathrm{opt}}\ \mathrm{pW}\ (\text{for } 220\ \mathrm{GHz}). \tag{C.3}$$

In the case of the telescope window covering by the liquid nitrogen blackbody source ($T_{\mathrm{rad}} = 77$ K) the absorbed power from the blackbody source is given by

$$P_{\mathrm{abs-cold,145\ GHz}} = 20\eta_{\mathrm{opt}}\ \mathrm{pW}\ (\text{for } 145\ \mathrm{GHz}), \tag{C.4}$$

and

$$P_{\mathrm{abs-cold,220\ GHz}} = 26\eta_{\mathrm{opt}}\ \mathrm{pW}\ (\text{for } 220\ \mathrm{GHz}). \tag{C.5}$$

Appendix D

The model of the geometrical dependence of Two Level System noise in the PSD

In Chapter 6, we include the simple geometrical scaling of the TLS noise level shown in Eq. 6.30 in the MKID forecaster. In this Appendix, we evaluate more realistic geometrical dependence of TLS noise based on semiemprical model proposed by J. Gao *et al*. [89].

D.1 The geometrical dependence of the TLS noise model

J. Gao *et al*. [89] proposed semiempirical noise model for TLS noise in frequency PSD, S_{f_r}/f_r^2, given by

$$\frac{S_{f_r}}{f_r^2} = \kappa(f,\omega,T)\frac{\int_{V_h}|\vec{E}|^3 \mathrm{d}\vec{r}}{(C_l V_0^2 l)^2}, \tag{D.1}$$

where the latter term shows the geometrical dependence of the TLS noise, $\kappa(f,\omega,T)$ is the sampling frequency, readout frequency, and temperature dependence, V_0 is the voltage at open end, l is the resonator length, E is the electric field, V_h is the TLS host material volume, and C_l is the capacitance of the coplanar waveguide (CPW) line given by

$$C_l = 4\epsilon_0\epsilon_{\mathrm{eff}}\frac{K(k)}{K(k')}, \tag{D.2}$$

where ϵ_0 is the permittivity of vacuum and ϵ_{eff} is the effective dielectric constant of the CPW line, K is the complete elliptic integral, $k = s/(s+2w)$ (s and w are the center strip and gap width of the CPW line, respectively.), and $k' = \sqrt{1-k^2}$. The relation between the voltage at open end and geometry is given by [84]

$$V_0 \propto 2K(k'). \tag{D.3}$$

The TLS noise mainly exists at metal substrate interface, metal air interface, substrate air interface and the edge of the metal [92, 137] shown in Figure D.1. The TLS noise is proportional to the third power of the electric field $|E|^3$. Based on the knowledge, we calculate the relative geometric dependence of the TLS noise effect by considering the third power of the electric field distribution at the metal and the substrate surface using Schwarz-Christoffel mapping which is a type of the conformal mapping useful in microwave engineering. The relation between the geometry and the summation of the third power of the electrical field at surface of the metal

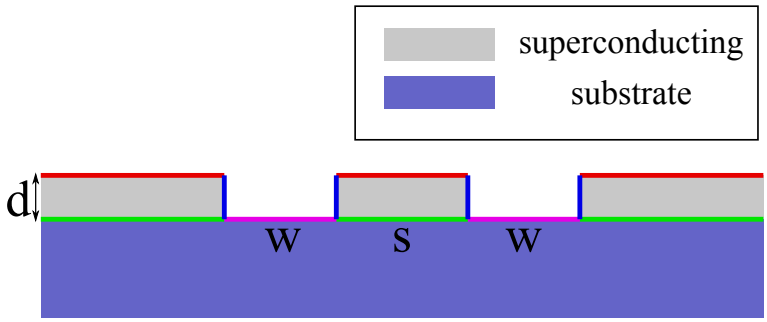

FIGURE D.1: The TLS noise distribution. The figure shows the cross section of the CPW line. The TLS noise is mainly distributed at metal substrate interface (red region), at metal edge (blue region), at metal substrate interface (green region), and at substrate air interface (magenta region).

and substrate influencing the TLS noise is given by [89, 84]

$$\int_{V_h} |\vec{E}|^3 \mathrm{d}\vec{r} \propto \frac{4}{a^2}\left(\int_0^{1/k_0} G'(u)\mathrm{d}u + \int_{1/k_0}^{1} G'(u)\mathrm{d}u + \int_{1/k_1}^{\infty} G'(u)\mathrm{d}u + \int_{1/k}^{1/k_1} G'(u)\mathrm{d}u + \int_{1}^{1/k} G'(u)\mathrm{d}u\right) = \frac{4}{a^2} I', \tag{D.4}$$

where first, second, third, forth, and fifth terms represent the relation between the geometry and the third power of the electric field influencing the TLS noise at the center strip interface, at the metal edge of the center strip, at the interface of the groundplane, at the metal edge of the groundplane, and at the substrate air interface, respectively, $a = s/2$, $k_0 = 1 + \frac{2t}{\pi a}$ (t is the half thickness of the resonator), $k_1 = \frac{a}{b}\left(1 - \frac{2t}{\pi b}\right)$ ($b = s/2 + w$) [84], and $G'(u)$ represents the third power of the electric field distribution using Schwarz-Christoffel mapping given by

$$G'(u) = \frac{1}{\left|(1-k_0^2u^2)(1-k_1^2u^2)\sqrt{(1-u^2)(1-k^2u^2)}\right|}. \tag{D.5}$$

Therefore the relative geometrical dependence of the TLS noise is given by

$$\frac{\int_{V_h} |\vec{E}|^3 \mathrm{d}\vec{r}}{(C_l V_0^2 l)^2} \propto \frac{I'}{64a^2\epsilon_0^2\epsilon_{\mathrm{eff}}^2 K(k)^2 K(k')^2 l^2}. \tag{D.6}$$

Using Eq. D.6, we can evaluate the relative geometrical dependence of TLS noise in the PSD.

D.2 The geometrical dependence of the TLS noise for PEC

In the case of perfect electric conductor (PEC), the effective dielectric constant ϵ_{eff} is given by

$$\epsilon_{\mathrm{eff}} = \frac{1 + \epsilon_{\mathrm{sub}}}{2}, \tag{D.7}$$

where ϵ_{sub} is the relative permittivity of substrate. We calculate relative geometrical dependence of the TLS noise by Eq. (D.6) as a function of total CPW width for PEC using the python package (scipy.integrate.quad). To avoid the singularities in

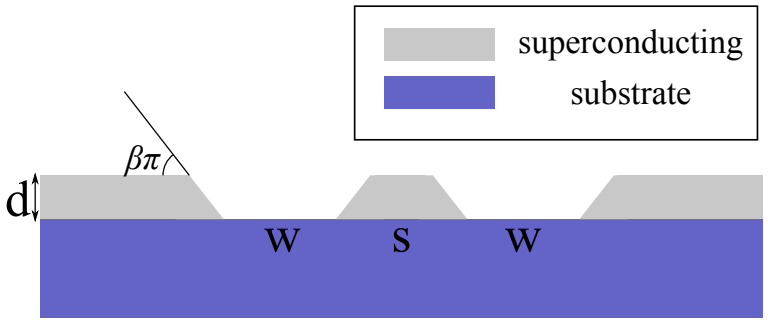

FIGURE D.2: To avoid the singularities in Eq. D.6. The angle of the metal edge is set $\beta\pi(< \pi/2)$.

Eq. D.6, we must consider the angle of the metal edge to be less than $\pi/2$ [89]. When the edge angle is $\beta\pi$ shown in Figure D.2, the third power of the electric field distribution using Schwarz-Christoffel mapping $G'(u)$ is rewritten by

$$G'(u) = \frac{1}{a^2}\left|\frac{[(1-u^2)(1-ku^2)]^{2\beta}}{[(1-u^2)(1-ku^2)]^{3/2}[(1-k_0^2u^2)(1-k_1u^2)]^{2\beta}}\right|. \tag{D.8}$$

When $\beta = \frac{89.5}{180}$, the relative geometrical dependence of TLS noise as a function of total CPW line width are shown in Figure D.3. We normalize the results by the result at $s = 3$ μm and $w = 2$ μm. All results are calculated for CPW thicknesses of $d = 200$ nm. As a results, even if the total CPW width is same, the amplitude of the TLS noise effect in the the PSD at the ratio fixed $s : w = 3 : 2$ is lower than that fixed $s = 3$ μm and $w = 2$ μm. The results are almost same results proposed by R. Barends *et al*. [92].

D.3 The geometrical dependence of the TLS noise including the superconducting features

The effective dielectric constant including the superconducting features [120] is given by

$$\epsilon'_{\text{eff}} = c^2 L_{\text{tot}} C_l = c^2 \frac{L_g}{1-\alpha_k} C_l, \tag{D.9}$$

where L_{tot} is the total inductance of the CPW line which is summation of the kinetic inductance L_k and geometrical inductance L_g, and α_k is the kinetic inductance fraction which is the kinetic inductance per total inductance. The geometric inductance is given by

$$L_g = \frac{\mu_0}{4}\frac{K(k')}{K(k)}, \tag{D.10}$$

where mu_0 is the vacuum permeability. Therefore, the effective dielectric constant including in the superconducting features is given by

$$\epsilon'_{\text{eff}} = \frac{\epsilon_{\text{eff}}}{1-\alpha_k}. \tag{D.11}$$

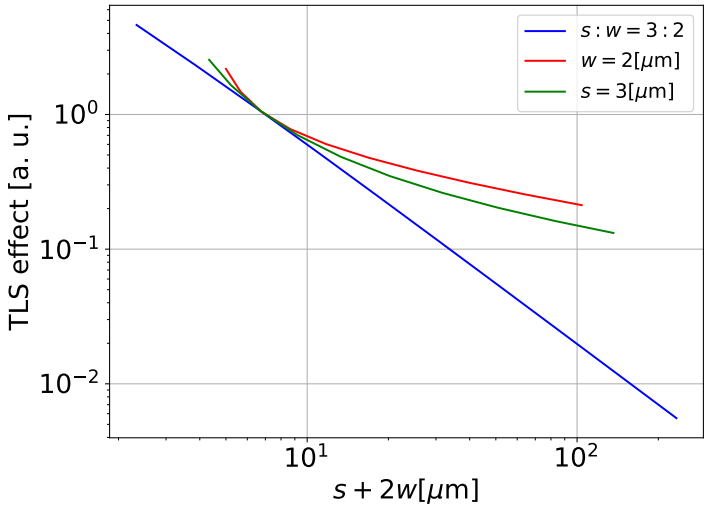

FIGURE D.3: The relative geometrical dependence of the TLS noise as a function of total center strip width. We normalize the results using the result at $s = 3$ μm and $w = 2$ μm. All results are calculated with the thickness of CPW of $d = 200$ nm. The blue line shows the relative geometrical dependence of the TLS noise fixed the ratio $s : w = 3 : 2$. The red line shows the relative geometrical dependence of the TLS noise fixed $w = 2$ μm. The green line shows the relative geometrical dependence of the TLS noise fixed $s = 3$ μm.

Using this effective dielectric constant, the geometrical dependence of the TLS noise is redefine by

$$\frac{\int_{V_h} |\vec{E}|^3 \mathrm{d}\vec{r}}{(C_l V_0^2 l)^2} \propto \frac{(1-\alpha_k^2) I'}{64 a^2 \epsilon_0^2 \epsilon_{\mathrm{eff}}^2 K(k)^2 K(k')^2 l^2}. \tag{D.12}$$

The result shows that the TLS noise effect decrease with increasing the kinetic inductance fraction. The kinetic inductance of the NbTiN is higher than the kinetic inductance of Nb with same geometry, because the penetration depth of NbTiN is larger than that of Nb. R. Barends *et al*. [92] propose the TLS noise effect of NbTiN film is 11 dB lower than that of Nb film studied by J. Gao *et al*. [88]. We estimate the results can be explained by Eq. (D.12).

Bibliography

[1] Steven Weinberg et al. *Cosmology*. Oxford university press, 2008.

[2] E Dwek et al. "Morphology, near-infrared luminosity, and mass of the Galactic bulge from COBE DIRBE observations". In: *The Astrophysical Journal* 445 (1995), pp. 716–730.

[3] Charles L Bennett et al. "Nine-year Wilkinson Microwave Anisotropy Probe (WMAP) observations: final maps and results". In: *The Astrophysical Journal Supplement Series* 208.2 (2013), p. 20.

[4] Planck Collaboration et al. "Planck 2018 results. VI. Cosmological parameters". In: (2020).

[5] Pea de Bernardis et al. "A flat Universe from high-resolution maps of the cosmic microwave background radiation". In: *Nature* 404.6781 (2000), pp. 955–959.

[6] Shaul Hanany et al. "MAXIMA-1: a measurement of the cosmic microwave background anisotropy on angular scales of 10'-5". In: *The Astrophysical Journal Letters* 545.1 (2000), p. L5.

[7] Alan H Guth. "Inflationary universe: A possible solution to the horizon and flatness problems". In: *Physical Review D* 23.2 (1981), p. 347.

[8] Katsuhiko Sato. "First-order phase transition of a vacuum and the expansion of the Universe". In: *Monthly Notices of the Royal Astronomical Society* 195.3 (1981), pp. 467–479.

[9] Uros Seljak and Matias Zaldarriaga. "Signature of gravity waves in the polarization of the microwave background". In: *Physical Review Letters* 78.11 (1997), p. 2054.

[10] Lloyd Knox and Yong-Seon Song. "Limit on the Detectability of the Energy Scale of Inflation". In: *Physical Review Letters* 89.1 (2002), p. 011303.

[11] Antony Lewis, Anthony Challinor, and Anthony Lasenby. "Efficient computation of cosmic microwave background anisotropies in closed Friedmann-Robertson-Walker models". In: *The Astrophysical Journal* 538.2 (2000), p. 473.

[12] PAR Ade et al. "Constraints on Primordial Gravitational Waves Using Planck, WMAP, and New BICEP2/Keck Observations through the 2015 Season". In: *Physical review letters* 121.22 (2018), p. 221301.

[13] R Keisler et al. "Measurements of sub-degree B-mode polarization in the cosmic microwave background from 100 square degrees of SPTpol data". In: *The Astrophysical Journal* 807.2 (2015), p. 151.

[14] JT Sayre et al. "Measurements of B-mode polarization of the cosmic microwave background from 500 square degrees of SPTpol data". In: *Physical Review D* 101.12 (2020), p. 122003.

[15] S Adachi et al. "A Measurement of the Degree-scale CMB B-mode Angular Power Spectrum with POLARBEAR". In: *The Astrophysical Journal* 897.1 (2020), p. 55.

[16] Y Fukuda et al. "Evidence for oscillation of atmospheric neutrinos". In: *Physical Review Letters* 81.8 (1998), p. 1562.

[17] Erminia Calabrese, David Alonso, and Jo Dunkley. "Complementing the ground-based CMB-S4 experiment on large scales with the PIXIE satellite". In: *Physical Review D* 95.6 (2017), p. 063504.

[18] Wayne S Holland et al. "SCUBA: a common-user submillimetre camera operating on the James Clerk Maxwell Telescope". In: *Monthly Notices of the Royal Astronomical Society* 303.4 (1999), pp. 659–672.

[19] Jason Glenn et al. "Bolocam: a millimeter-wave bolometric camera". In: *Advanced Technology MMW, Radio, and Terahertz Telescopes*. Vol. 3357. 1998, pp. 326–334.

[20] Brian G Keating et al. "BICEP: a large angular-scale CMB polarimeter". In: *Polarimetry in Astronomy*. Vol. 4843. 2003, pp. 284–295.

[21] D Barkats et al. "Cosmic microwave background polarimetry using correlation receivers with the PIQUE and CAPMAP experiments". In: *The Astrophysical Journal Supplement Series* 159.1 (2005), p. 1.

[22] QUIET Collaboration et al. "The QUIET instrument". In: *ArXiv e-prints* 1207 (2012).

[23] KD Irwin. "An application of electrothermal feedback for high resolution cryogenic particle detection". In: *Applied Physics Letters* 66.15 (1995), pp. 1998–2000.

[24] M Dobbs et al. "APEX-SZ first light and instrument status". In: *New Astronomy Reviews* 50.11-12 (2006), pp. 960–968.

[25] Hien Trong Nguyen et al. "BICEP2/SPUD: searching for inflation with degree scale polarimetry from the South Pole". In: *Millimeter and Submillimeter Detectors and Instrumentation for Astronomy IV*. Vol. 7020. 2008, 70201F.

[26] Arthur Kosowsky. "The atacama cosmology telescope". In: *New Astronomy Reviews* 47.11-12 (2003), pp. 939–943.

[27] JE Carlstrom et al. "The 10 meter south pole telescope". In: *Publications of the Astronomical Society of the Pacific* 123.903 (2011), p. 568.

[28] Zigmund D Kermish et al. "The POLARBEAR experiment". In: *Millimeter, Submillimeter, and Far-Infrared Detectors and Instrumentation for Astronomy VI*. Vol. 8452. 2012, p. 84521C.

[29] Peter Ade et al. "The Simons Observatory: science goals and forecasts". In: *Journal of Cosmology and Astroparticle Physics* 2019.02 (2019), p. 056.

[30] T Matsumura et al. "Mission design of LiteBIRD". In: *Journal of Low Temperature Physics* 176.5-6 (2014), pp. 733–740.

[31] B Dober et al. "Microwave SQUID multiplexer demonstration for cosmic microwave background imagers". In: *Applied Physics Letters* 111.24 (2017), p. 243510.

[32] J Schlaerth et al. "A millimeter and submillimeter kinetic inductance detector camera". In: *Journal of Low Temperature Physics* 151.3-4 (2008), pp. 684–689.

[33] NG Czakon et al. "Microwave kinetic inductance detector (MKID) camera testing for submillimeter astronomy". In: *AIP Conference Proceedings*. Vol. 1185. 1. 2009, pp. 172–175.

[34] Alessandro Monfardini et al. "NIKA: A millimeter-wave kinetic inductance camera". In: *Astronomy & Astrophysics* 521 (2010), A29.

[35] M Calvo et al. "The NIKA2 instrument, a dual-band kilopixel KID array for millimetric astronomy". In: *Journal of Low Temperature Physics* 184.3-4 (2016), pp. 816–823.

[36] Akira Endo et al. "First light demonstration of the integrated superconducting spectrometer". In: *Nature Astronomy* 3.11 (2019), pp. 989–996.

[37] Nicholas Galitzki et al. "The next generation BLAST experiment". In: *Journal of Astronomical Instrumentation* 3.02 (2014), p. 1440001.

[38] Jason E Austermann et al. "Millimeter-wave polarimeters using kinetic inductance detectors for TolTEC and beyond". In: *Journal of Low Temperature Physics* 193.3 (2018), pp. 120–127.

[39] Jochem JA Baselmans et al. "A kilo-pixel imaging system for future space based far-infrared observatories using microwave kinetic inductance detectors". In: *Astronomy & Astrophysics* 601 (2017), A89.

[40] BA Mazin et al. "ARCONS: A 2024 pixel optical through near-IR cryogenic imaging spectrophotometer". In: *Publications of the Astronomical Society of the Pacific* 125.933 (2013), p. 1348.

[41] Seth R Meeker et al. "DARKNESS: a microwave kinetic inductance detector integral field spectrograph for high-contrast astronomy". In: *Publications of the Astronomical Society of the Pacific* 130.988 (2018), p. 065001.

[42] SJC Yates et al. "Photon noise limited radiation detection with lens-antenna coupled microwave kinetic inductance detectors". In: *Applied Physics Letters* 99.7 (2011), p. 073505.

[43] J. Gao. PhD thesis. California Institute of Technology, Pasadena, California, 2008.

[44] WA Phillips. "Two-level states in glasses". In: *Reports on Progress in Physics* 50.12 (1987), p. 1657.

[45] P W Anderson, BI Halperin, and C M Varma. "Anomalous low-temperature thermal properties of glasses and spin glasses". In: *Philosophical Magazine* 25.1 (1972), pp. 1–9.

[46] Omid Noroozian et al. "Two-level system noise reduction for microwave kinetic inductance detectors". In: *AIP Conference Proceedings*. Vol. 1185. 1. 2009, pp. 148–151.

[47] Osamu Tajima et al. "GroundBIRD: an experiment for CMB polarization measurements at a large angular scale from the ground". In: *Millimeter, Submillimeter, and Far-Infrared Detectors and Instrumentation for Astronomy VI*. Vol. 8452. 2012, p. 84521M.

[48] S Oguri et al. "GroundBIRD experiment: Detecting CMB polarization power in a large angular scale from the ground". In: *Journal of Low Temperature Physics* 176.5-6 (2014), pp. 691–697.

[49] S Oguri et al. "Groundbird: observing cosmic microwave polarization at large angular scale with kinetic inductance detectors and high-speed rotating telescope". In: *Journal of Low Temperature Physics* 184.3-4 (2016), pp. 786–792.

[50] Shugo Oguri et al. "GroundBIRD: observations of CMB polarization with fast scan modulation and MKIDs". In: *Ground-based and Airborne Telescopes VI*. Vol. 9906. 2016, p. 99063L.

[51] J Choi et al. "Status of the GroundBIRD Telescope". In: *EPJ Web of Conferences*. Vol. 168. 2018, p. 01014.

[52] Taketo Nagasaki et al. "GroundBIRD: Observation of CMB Polarization with a Rapid Scanning and MKIDs". In: *Journal of Low Temperature Physics* 193.5-6 (2018), pp. 1066–1074.

[53] K Lee et al. "GroundBIRD: A CMB Polarization Experiment with MKID Arrays". In: *Journal of Low Temperature Physics* 200.5 (2020), pp. 384–391.

[54] Jihoon Choi. PhD thesis. Korea University, Korea, 2015.

[55] Y Mizugutch, M Akagawa, and H Yokoi. "Offset dual reflector antenna". In: *isap*. 1976, pp. 2–5.

[56] Peter K Day et al. "A broadband superconducting detector suitable for use in large arrays". In: *Nature* 425.6960 (2003), pp. 817–821.

[57] Jonas Zmuidzinas. "Superconducting microresonators: Physics and applications". In: *Annu. Rev. Condens. Matter Phys.* 3.1 (2012), pp. 169–214.

[58] Daniel Flanigan et al. "Photon noise from chaotic and coherent millimeter-wave sources measured with horn-coupled, aluminum lumped-element kinetic inductance detectors". In: *Applied Physics Letters* 108.8 (2016), p. 083504.

[59] John Bardeen, Leon N Cooper, and John Robert Schrieffer. "Theory of superconductivity". In: *Physical review* 108.5 (1957), p. 1175.

[60] AG Kozorezov et al. "Quasiparticle-phonon downconversion in nonequilibrium superconductors". In: *Physical Review B* 61.17 (2000), p. 11807.

[61] M Kurakado. "Possibility of high resolution detectors using superconducting tunnel junctions". In: *Nuclear Instruments and Methods in Physics Research* 196.1 (1982), pp. 275–277.

[62] Junta Komine. MA thesis. Kyoto University, Japan, 2019.

[63] Juan R Pardo, José Cernicharo, and Eugene Serabyn. "Atmospheric transmission at microwaves (ATM): an improved model for millimeter/submillimeter applications". In: *IEEE Transactions on antennas and propagation* 49.12 (2001), pp. 1683–1694.

[64] B Garcıa-Lorenzo et al. "Infrared astronomical characteristics of the Roque de los Muchachos Observatory: precipitable water vapour statistics". In: *Monthly Notices of the Royal Astronomical Society* 405.4 (2010), pp. 2683–2696.

[65] Hiroki Kutsuma et al. "A method to measure superconducting transition temperature of microwave kinetic inductance detector by changing power of readout microwaves". In: *Aip Advances* 10.9 (2020), p. 095320.

[66] Taketo Nagasaki. internal document. 2019.

[67] Hiroki Kutsuma. internal document. 2020.

[68] Masato Naruse. PhD thesis. The University of Tokyo, 2011.

[69] Kyungmin Lee. internal document. 2020.

[70] J Gao et al. "Equivalence of the effects on the complex conductivity of superconductor due to temperature change and external pair breaking". In: *Journal of Low Temperature Physics* 151.1-2 (2008), pp. 557–563.

[71] P. J. de Visser. PhD thesis. Delft University of Technology, Netherlands, 2014.

[72] SE Thompson et al. "Dynamical behaviour of superconducting microresonators with readout-power heating". In: *Superconductor Science and Technology* 26.9 (2013), p. 095009.

[73] PJ De Visser et al. "Microwave-induced excess quasiparticles in superconducting resonators measured through correlated conductivity fluctuations". In: *Applied Physics Letters* 100.16 (2012), p. 162601.

[74] PJ De Visser et al. "Evidence of a nonequilibrium distribution of quasiparticles in the microwave response of a superconducting aluminum resonator". In: *Physical review letters* 112.4 (2014), p. 047004.

[75] Hiroki Kutsuma et al. "A measurement method for responsivity of microwave kinetic inductance detector by changing power of readout microwaves". In: *Applied Physics Letters* 115.3 (2019), p. 032603.

[76] WL McMillan. "Transition temperature of strong-coupled superconductors". In: *Physical Review* 167.2 (1968), p. 331.

[77] G. Vardulakis. PhD thesis. University of Cambridge, Cambridge, 2007.

[78] B. A. Mazin. PhD thesis. California Institute of Technology, Pasadena, California, 2004.

[79] SB Kaplan et al. "Quasiparticle and phonon lifetimes in superconductors". In: *Physical Review B* 14.11 (1976), p. 4854.

[80] PJ De Visser et al. "Number fluctuations of sparse quasiparticles in a superconductor". In: *Physical review letters* 106.16 (2011), p. 167004.

[81] DC Mattis and John Bardeen. "Theory of the anomalous skin effect in normal and superconducting metals". In: *Physical Review* 111.2 (1958), p. 412.

[82] W Henkels and C Kircher. "Penetration depth measurements on type II superconducting films". In: *IEEE Transactions on magnetics* 13.1 (1977), pp. 63–66.

[83] Richard L Kautz. "Picosecond pulses on superconducting striplines". In: *Journal of Applied Physics* 49.1 (1978), pp. 308–314.

[84] R. E. Collins. *Foundations for microwave engineering*. McGraw-Hill, New York, 2001.

[85] R. Barends. PhD thesis. Delft University of Technology, Netherlands, 2009.

[86] David M Pozar. *Microwave engineering*. John wiley & sons, 2011.

[87] CM Wilson, L Frunzio, and DE Prober. "Time-resolved measurements of thermodynamic fluctuations of the particle number in a nondegenerate Fermi gas". In: *Physical review letters* 87.6 (2001), p. 067004.

[88] Jiansong Gao et al. "Noise properties of superconducting coplanar waveguide microwave resonators". In: *Applied Physics Letters* 90.10 (2007), p. 102507.

[89] Jiansong Gao et al. "A semiempirical model for two-level system noise in superconducting microresonators". In: *Applied Physics Letters* 92.21 (2008), p. 212504.

[90] Shwetank Kumar et al. "Temperature dependence of the frequency and noise of superconducting coplanar waveguide resonators". In: *Applied Physics Letters* 92.12 (2008), p. 123503.

[91] R Barends et al. "Noise in NbTiN, Al, and Ta superconducting resonators on silicon and sapphire substrates". In: *IEEE transactions on applied superconductivity* 19.3 (2009), pp. 936–939.

[92] R Barends et al. "Reduced frequency noise in superconducting resonators". In: *Applied Physics Letters* 97.3 (2010), p. 033507.

[93] C Neill et al. "Fluctuations from edge defects in superconducting resonators". In: *Applied Physics Letters* 103.7 (2013), p. 072601.

[94] Michael R Vissers et al. "Low loss superconducting titanium nitride coplanar waveguide resonators". In: *Applied Physics Letters* 97.23 (2010), p. 232509.

[95] AV Sergeev, VV Mitin, and BS Karasik. "Ultrasensitive hot-electron kinetic-inductance detectors operating well below the superconducting transition". In: *Applied physics letters* 80.5 (2002), pp. 817–819.

[96] Ryo Koyano. MA thesis. Saitama University, Japan, 2016.

[97] Hiroki Kutsuma. MA thesis. Tohoku University, Japan, 2018.

[98] Hikaru Ishitsuka. MA thesis. the Graduate University for Advanced Studies, Japan, 2015.

[99] H Ishitsuka et al. "Front–end electronics for the array readout of a microwave kinetic inductance detector towards observation of cosmic microwave background polarization". In: *Journal of Low Temperature Physics* 184.1-2 (2016), pp. 424–430.

[100] J Suzuki et al. "Development of a data acquisition system for kinetic inductance detectors: wide dynamic range and high sampling rate for astronomical observation". In: *Journal of Low Temperature Physics* 193.3-4 (2018), pp. 562–569.

[101] Joris van Rantwijk et al. "Multiplexed readout for 1000-pixel arrays of microwave kinetic inductance detectors". In: *IEEE Transactions on Microwave Theory and Techniques* 64.6 (2016), pp. 1876–1883.

[102] Anthony Megrant et al. "Planar superconducting resonators with internal quality factors above one million". In: *Applied Physics Letters* 100.11 (2012), p. 113510.

[103] MS Khalil et al. "An analysis method for asymmetric resonator transmission applied to superconducting devices". In: *Journal of Applied Physics* 111.5 (2012), p. 054510.

[104] Junya Suzuki. internal document. 2018.

[105] BL Blackford. "A tunneling investigation of energy-gap anisotropy in superconducting bulk aluminum crystals". In: *Journal of Low Temperature Physics* 23.1-2 (1976), pp. 43–52.

[106] A Fyhrie et al. "Decay Times of Optical Pulses for Aluminum CPW KIDs". In: *Journal of Low Temperature Physics* (2020), pp. 1–8.

[107] MR Vissers et al. "Ultrastable millimeter-wave kinetic inductance detectors". In: *Applied Physics Letters* 116.3 (2020), p. 032601.

[108] Agnes Dominjon et al. "Study of superconducting bilayer for microwave kinetic inductance detectors for astrophysics". In: *IEEE Transactions on Applied Superconductivity* 26.3 (2016), pp. 1–6.

[109] RMJ Janssen et al. "High optical efficiency and photon noise limited sensitivity of microwave kinetic inductance detectors using phase readout". In: *Applied Physics Letters* 103.20 (2013), p. 203503.

[110] Stefan Vehrheul. MA thesis. Delft University of Technology, Netherlands, 2019.

[111] Ilya Besedin and Alexey P Menushenkov. "Quality factor of a transmission line coupled coplanar waveguide resonator". In: *EPJ Quantum Technology* 5.1 (2018), pp. 1–16.

[112] RMJ Janssen et al. "Power handling and responsivity of submicron wide superconducting coplanar waveguide resonators". In: *Journal of Low Temperature Physics* 167.3-4 (2012), pp. 354–359.

[113] G Jones et al. "High quality factor manganese-doped aluminum lumped-element kinetic inductance detectors sensitive to frequencies below 100 GHz". In: *Applied Physics Letters* 110.22 (2017), p. 222601.

[114] Hidesato Ishida. MA thesis. Tohoku University, Japan, 2020.

[115] Hiroki Kutsuma. internal document. 2019.

[116] Chunhua Song et al. "Microwave response of vortices in superconducting thin films of Re and Al". In: *Physical Review B* 79.17 (2009), p. 174512.

[117] Gheorghe Stan, Stuart B Field, and John M Martinis. "Critical field for complete vortex expulsion from narrow superconducting strips". In: *Physical review letters* 92.9 (2004), p. 097003.

[118] Hiroki Kutsuma et al. "Optimization of Geomagnetic Shielding for MKIDs Mounted on a Rotating Cryostat". In: *Journal of Low Temperature Physics* 193.3-4 (2018), pp. 203–208.

[119] Michael Y Frankel et al. "Terahertz attenuation and dispersion characteristics of coplanar transmission lines". In: *IEEE Transactions on microwave theory and techniques* 39.6 (1991), pp. 910–916.

[120] S Hähnle et al. "Suppression of radiation loss in high kinetic inductance superconducting co-planar waveguides". In: *Applied Physics Letters* 116.18 (2020), p. 182601.

[121] Josh Y Mutus et al. "Strong environmental coupling in a Josephson parametric amplifier". In: *Applied Physics Letters* 104.26 (2014), p. 263513.

[122] C Bockstiegel et al. "Development of a broadband NbTiN traveling wave parametric amplifier for MKID readout". In: *Journal of Low Temperature Physics* 176.3-4 (2014), pp. 476–482.

[123] Saul Perlmutter et al. "Measurements of Ω and Λ from 42 high-redshift supernovae". In: *The Astrophysical Journal* 517.2 (1999), p. 565.

[124] Adam G Riess et al. "Observational evidence from supernovae for an accelerating universe and a cosmological constant". In: *The Astronomical Journal* 116.3 (1998), p. 1009.

[125] Arno A Penzias and Robert Woodrow Wilson. "A measurement of excess antenna temperature at 4080 Mc/s." In: *The Astrophysical Journal* 142 (1965), pp. 419–421.

[126] DJ Fixsen and JC Mather. "The spectral results of the far-infrared absolute spectrophotometer instrument on COBE". In: *The Astrophysical Journal* 581.2 (2002), p. 817.

[127] JC Mather et al. "Calibrator Design for the COBE Far-Infrared Absolute Spectrophotometer (FIRAS)". In: *The Astrophysical Journal* 512 (1999), p. 511.

[128] DJ Fixsen et al. "The Cosmic Microwave Background Spectrum from the Full COBE FIRAS Data". In: *The Astrophysical Journal* 473 (1996), p. 576.

[129] *COsmic Background Explorer / FIRAS. FIRAS PROJECT DATA SETS.*

[130] Damian Twerenbold. "Giaever-type superconducting tunnelling junctions as high-resolution X-ray detectors". In: *EPL (Europhysics Letters)* 1.5 (1986), p. 209.

[131] H Kraus et al. "Quasiparticle trapping in a superconductive detector system exhibiting high energy and position resolution". In: *Physics Letters B* 231.1-2 (1989), pp. 195–202.

[132] Alex D Semenov, Gregory N Gol'tsman, and Alexander A Korneev. "Quantum detection by current carrying superconducting film". In: *Physica C: Superconductivity* 351.4 (2001), pp. 349–356.

[133] GN Gol'Tsman et al. "Picosecond superconducting single-photon optical detector". In: *Applied physics letters* 79.6 (2001), pp. 705–707.

[134] Alexei D Semenov et al. "Terahertz performance of integrated lens antennas with a hot-electron bolometer". In: *IEEE transactions on microwave theory and techniques* 55.2 (2007), pp. 239–247.

[135] Andreas Fleischmann, Ch Enss, and GM Seidel. "Metallic magnetic calorimeters". In: *Cryogenic particle detection*. 2005, pp. 151–216.

[136] Colin Bischoff. PhD thesis. The university of Chicago, 2010.

[137] J Wenner et al. "Surface loss simulations of superconducting coplanar waveguide resonators". In: *Applied Physics Letters* 99.11 (2011), p. 113513.